UNIVERSITY OF SOUTHAMPTON

Faculty of Engineering and Physical Sciences
Zepler Institute for Photonics and Nanoelectronics

Slow light superstructure gratings for optical storage and enhancing second harmonic generation

by

Thomas Edward Maybour
ORCiD: 0000-0002-5259-9604

A thesis for the degree of
Doctor of Philosophy

January 2022

Abstract

Slow light is the phenomenon whereby a large reduction in group velocity is observed close to a resonance. Devices which exhibit this behaviour are of great general interest and have numerous applications. The primary focus for such devices is in the creation of optical storage and quantum memories. They also have additional applications in optical switching and enhancing optical nonlinearities. The field of slow light generated a great deal of interest when it was demonstrated that exceptionally low group velocities down to the speed of a cyclist were achieved using electromagnetically induced transparency. Since that time there has been significant activity in developing new slow light devices. Along with electromagnetically induced transparency, devices have been developed using fibres and photonic crystals. However, all such devices are limited by the delay-bandwidth product. The greater the reduction in the group velocity, the more delay the device can generate. Unfortunately, this is also accompanied by a decrease in the available bandwidth which limits the device storage capacity.

In this work a slow device based on a dynamic moiré grating is explored. A moiré grating produces a double resonant structure with a slow light transmission band. The amount that the group velocity is reduced in a moiré grating is dependent on the size of the transmission band. A smaller transmission band leads to lower group velocities and so the device is bounded by the delay-bandwidth product. Here I show that by dynamically varying the coupling strength of a moiré grating, the limits imposed by the delay-bandwidth product can be potentially broken by many orders of magnitude. This result relies on symmetric switching of the coupling strength. I also show that asymmetric switching can generate bandwidth modulation. A potential realisation of such a device is presented using an electro-optic grating in a periodically poled medium. Applying an external quasi-static field allows for the dynamic control of the grating coupling strength.

Another feature of moiré gratings is that the generated slow light is accompanied by pulse compression and field enhancement. I explore in this work as means of enhancing second-harmonic generation. I then show that the slow light transmission band creates forward and backward second-harmonic modes with greater efficiency than a standard device. By including a second grating at the front of the device, the backward second-harmonic mode can be suppressed producing unidirectional output. The additional grating creates a resonance within the device which further enhances the second-harmonic generation. I show that by tuning the device parameters it is possible to achieve near complete conversion efficiency in regimes where conversion efficiency would ordinarily be negligible.

Declaration of Authorship

I declare that this thesis and the work presented in it is my own and has been generated by me as the result of my own original research.

I confirm that:

1. This work was done wholly or mainly while in candidature for a research degree at this University;
2. Where any part of this thesis has previously been submitted for a degree or any other qualification at this University or any other institution, this has been clearly stated;
3. Where I have consulted the published work of others, this is always clearly attributed;
4. Where I have quoted from the work of others, the source is always given. With the exception of such quotations, this thesis is entirely my own work;
5. I have acknowledged all main sources of help;
6. Where the thesis is based on work done by myself jointly with others, I have made clear exactly what was done by others and what I have contributed myself;
7. Parts of this work have been published as listed in Appendix A

Signed: Thomas Edward Maybour Date: 27/09/2021

Acknowledgements

First and foremost I would like to acknowledge and thank my supervisor Peter Horak for his help and guidance over the course of my PhD. I thank you for your endless patience and kindness. I feel very privileged to have been supervised by someone with such a breadth and depth of knowledge. It wouldn't have been possible to complete this thesis without your support. I would like to also thank my co-supervisor Devin Smith for sharing his knowledge and expertise.

I would like to extend my thanks to John for nudging me toward Python at the start of my PhD and who was always happy to help with any coding issues. Thanks to Sam and Dom for coffee and lunch time conversations and distractions.

A special thanks goes to my parents Ann and Tim and my parents-in-law Jean and Chris for their continued support and help. Without them it would not have been possible to undertake this PhD.

Finally, my thanks goes to my long suffering wife Hannah and my son Jack. Without you helping me through this I would not have crossed the finish line.

Contents

List of Figures

List of Abbreviations

GVD	Group velocity dispersion
EIT	Electromagnetically induced transparency
CPO	Coherent population oscillations
SHG	Second-harmonic-generation
QPM	Quasi-phase-matching
SPM	Self phase modulation
XPM	Cross phase modulation
FWHM	Full width at half maximum

List of Symbols

$\vec{B}$	Vacuum/macroscopic magnetic field
c	Speed of light
D	Group delay dispersion
$\vec{D}$	Auxiliary electric field
$\vec{E}$	Vacuum/macroscopic electric field
f	Frequency
$\vec{H}$	Auxiliary magnetic field
I	Field intensity
k	Wavenumber
K_B	Bragg grating wavenumber
K_S	Superstructure wavenumber
$\vec{P}$	Polarisation
$\vec{M}$	Magnetisation
n	Refractive index
$\bar{n}$	Effective refractive index
n_e	Electric index
n_g	Group index
n_m	Magnetic index
n_2	Nonlinear refractive index
v_E	Energy velocity
v_g	Group velocity
v_p	Phase velocity
α_a	Apodisation strength
α_B	Bragg absorption coefficient
β	Propagation constant
δn	Grating strength
Δ	Detuning
Δn	Refractive index change
ϵ_0	Vacuum permittivity
κ	Coupling constant
λ	Wavelength

λ_B	Bragg wavelength
Λ	Poling period
Λ_B	Bragg period
Λ_S	Superstructure period
μ	Time windowing strength of a dynamic grating
μ_0	Vacuum permeability
τ_g	Group delay
$\chi^{(e)}$	Electric susceptibility
$\chi^{(m)}$	Magnetic susceptibility
$\chi^{(2)}$	Quadratic electric susceptibility
$\chi^{(3)}$	Cubic electric susceptibility
ω	Angular frequency

Chapter 1

Introduction

The purpose of the research is to explore the application of slow light in creating an optical storage device and enhancing nonlinear processes. Optical and photonic storage devices are key components in developing future quantum technologies such as quantum repeaters [1, 2] and photonic quantum computers [3]. They are capable of storing an optical pulse or single photon which can subsequently be retrieved at a later time. Slow light is the phenomenon whereby the group velocity of a pulse envelope is slowed by a resonance. It has long been a goal to use a slow light resonance to trap and release pulses thereby making an optical storage device. However, the performance of slow light devices is constrained by a trade-off between the available bandwidth and the amount of the delay the device can produce. This constraint is therefore known as the delay-bandwidth product and is a limiting factor in producing slow light storage devices. Another consequence of slow light is that the reduced group velocity of a pulse results in an enhancement of its intensity. It has therefore been proposed as a means of enhancing nonlinear intensity dependent processes.

Before discussing these features of slow light in more detail, it is first useful to introduce the definitions which characterise the different velocities associated with wave phenomena. A monochromatic wave is one which is composed of a single angular frequency ω and associated wavenumber k. The connection between ω and k is commonly referred to as the dispersion relationship and is given by

$$\omega = ck. \tag{1.1}$$

The conversion factor c between the two quantities is known as the phase velocity. It is the speed at which the wavefronts of a wave propagate. For an electromatic wave in vacuum, the phase velocity is equal to the speed of light which is 299 792 458 m/s. The passage of light within a medium is impeded such that its phase velocity is reduced. The amount that a medium can impede the passage of light can often be characterised

by a single number n which is known as the refractive index. Each medium has a different refractive index which modifies the dispersion relationship such that

$$\omega = v_p \beta, \tag{1.2}$$

where the phase velocity is given by $v_p = c/n$ and $\beta = nk$ is the propagation constant. The factor of n in v_p and β cancel so that the two expressions (1.1) and (1.2) are equivalent. Equation (1.2) is known as a linear dispersion relationship and is a simplified model which approximately holds over small bandwidths. In general, a medium will respond differently to different applied frequencies and the phase velocity and propagation constant will be functions of the frequency

$$\omega = v_p(\omega)\beta(\omega), \tag{1.3}$$

A common way to express the frequency dependent propagation constant is using a Taylor expansion around a carrier frequency ω_0

$$\beta(\omega) = \beta_0 + \beta_1(\omega - \omega_0) + \frac{1}{2}\beta_2(\omega - \omega_0)^2 + \ldots, \tag{1.4}$$

where the coefficients are given by

$$\beta_n = \frac{\partial^n \beta(\omega)}{\partial^n \omega}. \tag{1.5}$$

When the coefficients for the index $n \geq 1$ are zero, the dispersion relationship is linear by (1.2); it is also common to refer this situation as dispersionless. When the higher order dispersion terms are non-zero, different frequencies will travel with different phase velocities which has implications for pulse propagation.

A pulse is constructed from a super position of different frequency waves which can in general be written as

$$p(t, z) = \int_{\infty}^{\infty} d\omega \; f(\omega) e^{i(\beta z - \omega t)}. \tag{1.6}$$

The function $f(\omega)$ is the Fourier transform of the pulse which is peaked around a carrier frequency ω_0. The pulse is then characterised by a carrier signal modulated by an envelope function which moves at a group velocity v_g. The definition of the group velocity is given by the inverse of the first order coefficient β_1 evaluated at the carrier frequency

$$v_g = \left.\frac{\partial \omega}{\partial \beta}\right|_{\omega=\omega_0} \tag{1.7}$$

The group velocity is only well defined when the pulse envelope is well defined. For a dispersionless medium the group velocity is simply equal to the phase velocity of the carrier frequency. In general, the frequency dependent phase velocity will will mean that the pulse will broaden due to the underlying superposition of waves (1.6) travelling at different speeds. This behaviour is characterised by the group velocity dispersion (GVD) which is given by the second coefficient β_2

$$GVD = \frac{\partial^2 \beta(\omega)}{\partial^2 \omega}. \tag{1.8}$$

An alternative definition of the group velocity dispersion is to define it by the derivative of inverse group velocity with respect to wavelength

$$D_\lambda = \frac{\partial}{\partial \lambda}\frac{1}{v_g}, \tag{1.9}$$

which is more commonly used in optical fibre communications. There are two different types of dispersion which are termed normal and anomalous. Normal dispersion occurs when the group velocity decreases with frequency, and conversely anomalous dispersion when it increases with frequency. Within a medium there are certain wavelengths where dispersion is zero, creating what is known as a zero dispersion wavelength. It is typically beneficial to centre the carrier frequency of a pulse at a zero dispersion wavelength in order to minimise broadening effects.

The higher order dispersion effects have so far been considered in the context of material dispersion. However, if a narrow enough pulse bandwidth is considered and the carrier frequency is far from any material resonance, then the linear dispersion relationship (1.2) provides a good approximation. Dispersion effects can also be induced structurally. By carefully engineering the material properties it is possible to tailor the dispersion relationship to fit a particular need.

With this brief overview of the basic properties of wave propagation, we can now return to topic of slow light. Quite simply, slow light refers to a dramatic decrease in the group velocity relative to the phase velocity. This is achieved when there is a flattening of the dispersion curve between the frequency and propagation constant. There are principally two ways of achieving this. The first is to use a material resonance and the second is to employ a structural resonance. In either case, a dramatic decrease in the group velocity can be observed close to a resonance. There are a number of review article which provide a thorough background into the field of slow light [4, 5, 6, 7, 8, 9, 10] as well as book devoted to the subject [11].

The principal metric for comparing the performance of different slow light devices is the delay-bandwidth product [12, 13, 14]. For any given slow light device, the product of the available slow light bandwidth and the induced delay is approximately constant. This means if the parameters of a particular device are altered such that the delay produced is increased, this will come at the expense of a decrease in the available bandwidth. The trade off between the two is such that their product remains unchanged. An ideal slow light device would produce very low group velocity with a large available bandwidth. Therefore the delay-bandwidth product is a useful metric for comparing devices, where devices with a larger product have better performance.

Calculating the product first requires the group delay. If a slow device has a group velocity v_g and length L, then the group delay τ_g that a pulse experiences in propagating from one end of the device to the other is given by

$$\tau_g = \frac{L}{v_g} \tag{1.10}$$

A common alternative way to express the group delay is using the group index which is defined as

$$n_g = \frac{c}{v_g}, \tag{1.11}$$

which is also known as the slow down factor [13]. It is defined in a similar way to the refractive index, being the ratio of the vacuum speed of light to the group velocity rather than the phase velocity. The group index is also another common figure of merit for slow light devices. The group delay can therefore also then be written as

$$\tau_g = \frac{n_g L}{c}. \tag{1.12}$$

Then if a slow light device has a resonance bandwidth of Δf, then its delay-bandwidth product is given by

$$DBP = \frac{n_g L}{c} \Delta f \tag{1.13}$$

The factor of L means that increasing the length of the device increases the size of the delay-bandwidth product.

While research into slow light has been going on for some time [15, 16, 17] albeit not necessary under the name slow light, it was not until the work of Hau et al [18] that the field garnered significant attention. In their ground breaking paper they showed that light could be slowed to 17 m/s using electromagnetically induced transparency (EIT)

in a gas of sodium atoms cooled close to absolute zero. EIT is an example of generating slow light by a material resonance. It works by using two driving fields to make an opaque medium transparent over a frequency band through which a probe field can propagate. Applying a driving force to a medium will cause electrons to oscillate at the frequency of the applied field. Transparency is achieved by the two driving fields having equal magnitude but opposite sign so that the driving force of one field acting on the electrons is cancelled by the other. With the driving fields suppressing electron oscillations the probe field is able to propagate through the medium [19].

After the work of Hau et al, it was later experimentally demonstrated that light could be stopped completely using EIT [20, 21]. This was achieved by switching off the driving fields whilst the probe pulse was still inside the medium. This closed the transmission window trapping the pulse inside the vapour cloud. Subsequently turning the driving field back on reopened the transmission window and allowed the pulse to escape.

EIT has demonstrated impressive results but it requires an atomic medium supercooled to temperatures close to absolute absolute. Circumventing this requirement led researchers to develop a new approach to producing slow light using spectral holes due to coherent population oscillations (CPO) [22, 23]. This approach was first demonstrated in a room temperature ruby crystal where a group velocity of 57.5 m/s was observed [24]. Although it has been demonstrated that both EIT and CPO could achieve extraordinarily low group velocities, the size of their slow light resonances are in the range of 10s of Hertz. Therefore the available pulse bandwidth is similarly restricted.

The second approach to generating slow light is to use a structured or engineered resonance. Typically this involves manipulating the material properties of a photonic crystal to create an artificial resonance that can be exploited for slow light. One such approach is to use coupled resonators [25, 26, 27] which offer similar properties to EIT [28]. Another approach has been to use Brillouin scattering which induces a slow light resonance using acoustic phonons [29, 30]. In this work we are principally interested in slow light generated by Bragg grating structures. A Bragg grating is a periodic modulation of the refractive index. It has the property that for a grating period Λ_B there is a resonance centred on the wavelength λ_B over which incoming light is reflected by the grating. The linewidth of the resonance is known as the band gap or rejection band. At the edges of the band gap the incoming light is rapidly coupled into forward and backward propagating modes which can lead to a substantial decrease in the group velocity of a propagating pulse generating slow light.

One of the mostly widely used mediums for fabricating Bragg gratings is in optical fibres. They were first developed in 1978 [31] when it was observed that UV light launched into an optical fibre was after a few minutes back-reflected. This process is

caused by an effect called photosensitivity. Using two interfering UV beams, photosensitivity allows for a periodic index modulation to be written into the core of an optical fibre [32].

The first significant demonstration of slow light in fibres was using optical solitons propagating through the grating band gap [33]. A group index of $n_g \approx 5$ was measured with a group delay of $\tau_g \approx 1.7\,\text{ns}$. Recent research exploiting the edges of the band gap have produced group indices as high as 1010 [34]. This corresponds to a group velocity of approximately $300\,\text{km/s}$. The authors reported that the available linewidth was 50 fm centred at 1549.72 nm which equates approximately to a bandwidth of 6 MHz.

One of the main issues with grating induced slow light is that the lower and upper band edges produce normal and anomalous dispersion respectively. The amount of second order dispersion at the band edges increases with the reduction in the group velocity. Therefore, slower group velocities result in stronger pulse broadening. One way to resolve this issue is to use a dual resonance grating known as a moiré grating [28, 35, 36]. A moiré grating consists of two super imposed grating periods which creates a dual band gap structure. Provided the linewidth between the grating periods is sufficiently small, a slow light transmission band opens between the the two band gaps. The normal and anomalous dispersion generated from the lower and upper edges of the two band gaps cancel creating a zero dispersion wavelength at the centre of the transmission band. Pulse broadening can then be minimised by setting the carrier wavelength to the centre of the transmission band. However, third order dispersion effects are still present.

The background theory for Bragg gratings is presented in Chapter 2. The standard approach to describing a Bragg grating is to develop a set of coupled mode equations by applying approximations to Maxwell's equations. A set of solutions is then found from which the group velocity and group delay dispersion can be calculated. It is shown that a significant reduction in group velocity occurs at the band gap edges produce by the grating along with strong second order dispersion. The theory describing Moiré gratings is then introduced and it is demonstrated how they cancel second order dispersion within a slow light transmission band.

In Chapter 3 an alternative approach to developing coupled mode equations is introduced using the Lagrangian formalism. The formalism is extended to nonlinear materials and it is shown how each coupled mode equation corresponds to varying the action with respect to each mode.

The fundamental limit on all slow light gratings is the delay-bandwidth product. Chapter 4 explores how this limit can be overcome by introducing a dynamic moiré grating. This is done by dynamically varying the grating strength of the underlying Bragg

grating. This has the effect of altering the size of the transmission band. The delay-bandwidth product can then be enhanced by the change in group velocity induced by dynamically varying the slow light resonance.

In Chapter 6 an approach to creating delay lines using Bragg gratings and cross phase modulation is examined. It is shown that to create gratings with lengths that can be fabricated with current technology, it is necessary to use the slow light band edge of the grating. The grating lengths can be decreased further by using switchable bandwidth using the transmission band of a moiré grating.

Next, the potential for enhancing non linear processes using a π-phase shifted grating is explored in Chapter 6. A π-phase shifted grating is closely related to a moiré grating. It is shown that when combined with a Bragg grating, significant enhancement to second-harmonic generation can be achieved in a quasi-phased matched medium.

Finally Chapter 7 provides conclusions and potential future research that could follow from the work contained in this thesis.

Chapter 2

Background

2.1 Electromagnetism

Electromagnetism is one of the four known fundamental forces of nature along with gravity, the strong nuclear force and weak nuclear force. Although electric and magnetic phenomena where documented by ancient civilisations, electromagnetism only really began to develop over the course of the 19th century. One of the most significant contributions to its development was by experimentalist Michael Faraday who introduced the concept of a field. Faraday became convinced after extensive experimentation of the existence of electric and magnetic fields that extended and filled all of space. This was a key insight but Faraday lacked the necessary mathematical training to quantitatively express his ideas. The problem was taken up by the mathematical physicist James Clerk Maxwell who in his 1865 work 'A dynamical theory of the electromagnetic field' [37] introduced a set of equations describing Faraday's electric and magnetic fields. His equations were revolutionary. They predicted the existence of electromagnetic waves which propagated at a speed approximately equal to what was the known speed of light at the time, thus establishing that light was an electromagnetic wave and unifying electromagnetism and optics. Today his equations are known in his honour as Maxwell's equations.

2.1.1 Maxwell's equations

In this thesis the version of Maxwell's equations that are of principle interest are the sourceless matter equations which are given by

$$\vec{\nabla} \cdot \vec{B} = 0 \tag{2.1}$$

$$\vec{\nabla} \times \vec{E} = -\frac{\partial \vec{B}}{\partial t} \tag{2.2}$$

$$\vec{\nabla} \cdot \vec{D} = 0 \tag{2.3}$$

$$\vec{\nabla} \times \vec{H} = \frac{\partial \vec{D}}{\partial t} \tag{2.4}$$

The $\vec{E}$ and $\vec{B}$ fields are the macroscopic electric and magnetic fields respectively and $\vec{D}$ and $\vec{H}$ fields are the auxiliary electric and magnetic fields respectively. The auxiliary fields often go by a number of different names. The $\vec{D}$ field is commonly referred to as the electric displacement or electric induction and the $\vec{H}$ field is commonly known as the magnetic field strength or magnetic intensity. We follow here the convention of calling them simply auxiliary fields.

Equations (2.1-2.4) are written in the vector calculus formalism where $\vec{\nabla}$ is known as the vector derivative which in Cartesian coordinates is given by

$$\vec{\nabla} = \hat{e}_x \frac{\partial}{\partial x} + \hat{e}_y \frac{\partial}{\partial y} + \hat{e}_z \frac{\partial}{\partial z}. \tag{2.5}$$

The four equations are known as Gauss's law for magnetism (2.3), the Maxwell-Faraday equation (2.2), Gauss's law (2.3) and Ampère's law (2.4). In the absence of any sources, Gauss's laws say that the macroscopic magnetic and auxiliary electric fields are divergenceless. The Maxwell-Faraday equation and Ampère's law describe how rotating electric and magnetic fields produce time varying magnetic and electric fields respectively.

The macroscopic and the auxiliary fields are related to each other through two further fields, the polarisation $\vec{P}$ and the magnetisation $\vec{M}$ by

$$\vec{D} = \epsilon_0 \vec{E} + \vec{P} \tag{2.6}$$

$$\vec{H} = \frac{1}{\mu_0} \vec{B} - \vec{M} \tag{2.7}$$

where ϵ_0 and μ_0 are the vacuum permittivity and permeability respectively. The polarisation and magnetisation contain all the information pertaining to a particular medium and characterise how that medium affects the fields and subsequent dynamics. In vacuum the polarisation and magnetisation are zero and Maxwell's equations reduce to the vacuum Maxwell equations

$$\vec{\nabla} \cdot \vec{B} = 0 \tag{2.8}$$

$$\vec{\nabla} \times \vec{E} = -\frac{\partial \vec{B}}{\partial t} \tag{2.9}$$

$$\vec{\nabla} \cdot \vec{E} = 0 \tag{2.10}$$

$$\vec{\nabla} \times \vec{B} = \frac{1}{c^2} \frac{\partial \vec{E}}{\partial t} \tag{2.11}$$

where $c = 1/\sqrt{\epsilon_0 \mu_0}$ is the speed of light in vacuum. Notice that Gauss's law for magnetism and the Maxwell-Faraday equation are the same in both the matter and vacuum equations and can be thought of as forming one set of Maxwell's equations; with Gauss's law and Ampère's law forming a second set.

There is an important subtly between the matter and vacuum equations. While the $\vec{E}$ and $\vec{B}$ fields in matter equations are the macroscopic fields, in the vacuum equations they are the vacuum fields. The macroscopic fields are averages of the vacuum fields over the atomic structure of a medium and therefore the sets of fields are only equivalent in the case where the polarisation and magnetisation are zero. In general the macroscopic fields do not satisfy the second set of the vacuum equations despite sharing the same notation. It should therefore always be clear from context whether the $\vec{E}$ and $\vec{B}$ refer to the macroscopic or vacuum fields.

Perhaps the most striking feature of Maxwell's equations is that they give rise to electromagnetic wave equations. By setting the magnetisation equal to zero, $\vec{M} = 0$, then the Faraday (2.2) and Ampere (2.4) laws can be combined to give the wave equation

$$\vec{\nabla}^2 \vec{E} = \mu_0 \frac{\partial^2 \vec{D}}{\partial t^2}. \tag{2.12}$$

It is more common to express this relationship using the polarisation given by (2.6) so that

$$\vec{\nabla}^2 \vec{E} - \frac{1}{c^2} \frac{\partial^2 \vec{E}}{\partial t^2} = \mu_0 \frac{\partial^2 \vec{P}}{\partial t^2} \tag{2.13}$$

In the vacuum case where $\vec{P} = 0$, the Faraday (2.2) and Ampere (2.4) laws give rise the vacuum wave equations for the electric and magnetic fields

$$\vec{\nabla}^2\vec{E} - \frac{1}{c^2}\frac{\partial^2\vec{E}}{\partial t^2} = 0, \tag{2.14}$$

$$\vec{\nabla}^2\vec{B} - \frac{1}{c^2}\frac{\partial^2\vec{B}}{\partial t^2} = 0. \tag{2.15}$$

2.1.2 Index notation

The previous section expressed Maxwell's equations in terms of three vector notation. Another useful notation is index notation which facilitates expressing Maxwell's equation in terms of tensors. Converting a general vector $\vec{A}$ into index notation is straight forward, it is simply given by $A_i \equiv \hat{e}_i \cdot \vec{A}$ where the dot product picks out the i^{th} component of the vector. The dot and cross products can be written in index notation by $A_iB_i \equiv \vec{A}\cdot\vec{B}$ and $\epsilon_{ijk}A_jB_k \equiv \vec{A}\times\vec{B}$ where $\vec{B}$ is another general vector. A common convention with index notation is to sum over repeated indices without including an explicit summation symbol. This convention is known as Einstein summation. The cross product in index notation uses the epsilon tensor ϵ_{ijk} also known as the totally anti-symmetric tensor. It is defined such that $\epsilon_{123} = 1$, then any odd permutation of the indices picks up a minus sign. For example $\epsilon_{132} = -1$, $\epsilon_{312} = 1$ and so on. Any repeated indices give zero such as $\epsilon_{122} = 0$. Maxwell's equations (2.1-2.4) can then be expressed in index notation as

$$\partial_i D_i = 0 \tag{2.16}$$

$$\epsilon_{ijk}\partial_j E_k = -\partial_t B_i \tag{2.17}$$

$$\partial_i B_i = 0 \tag{2.18}$$

$$\epsilon_{ijk}\partial_j H_k = \partial_t D_i \tag{2.19}$$

where

$$\partial_i \equiv \frac{\partial}{\partial x^i} \tag{2.20}$$

$$\partial_t \equiv \frac{\partial}{\partial t}. \tag{2.21}$$

2.1.3 Potentials and gauge invariance

Instead of expressing electromagnetism in terms of the electric and magnetic fields, an alternative approach is to use the vector potential A_i and the scalar potential ϕ. The potentials are related to the electric and magnetic fields through the relations

$$E_i = -\partial_t A_i - \partial_i \phi \tag{2.22}$$

$$B_i = \epsilon_{ijk} \partial_j A_k. \tag{2.23}$$

The fields and potentials give physically equivalent descriptions, however, there are certain circumstances where it necessary to use the potentials, such as with the Lagrangian formalism which is described in chapter 3. The potentials also allow electromagnetism to be expressed in a manifestly Lorentz invariant way by combining the potentials into a four potential by

$$A_\mu = (\phi, A_i). \tag{2.24}$$

The index μ runs from 0 to 3, where the 0 index of A_μ corresponds to the scalar potential. Another feature of electromagnetism that becomes evident when using the potentials is gauge invariance. This property allows the potentials to be transformed by an arbitrary gauge field f through the transformations

$$A_i \to A_i + \partial_i f \tag{2.25}$$

$$\phi \to \phi - \partial_t f. \tag{2.26}$$

Substituting the transformed potentials into the field definitions (2.22) and (2.23) leads to cancellation between all terms containing the gauge field. Therefore, making any arbitrary gauge transformation using (2.25) and (2.26) gives rise to the same electric and magnetic fields. This means that each gauge is physically equivalent. However, when analysing a given system, one gauge may provide greater simplification over another.

2.1.4 Incorporating matter

In a linear medium the polarisation and magnetisation are related to the $\vec{E}$ and $\vec{B}$ fields through matter susceptibilities. The susceptibilities are in general tensors and so it is convenient to express the relationships using index notation

$$P_i = \epsilon_0 \chi_{ij}^{(e)} E_j \tag{2.27}$$

$$M_i = \frac{1}{\mu_0} \chi_{ij}^{(m)} B_j. \tag{2.28}$$

The tensors $\chi_{ij}^{(e)}$ and $\chi_{ij}^{(m)}$ are the dimensionless electric and magnetic susceptibilities. They characterise the interaction of each of component of the macroscopic fields with the medium. It is often possible to approximate a medium as homogeneous and isotropic. In such a case the susceptibilities tensors can be expressed using the scalar susceptibilities $\chi^{(e)}$ and $\chi^{(m)}$ by the expressions

$$\chi_{ij}^{(e)} = \chi^{(e)} \delta_{ij} \tag{2.29}$$

$$\chi_{ij}^{(m)} = \frac{\chi^{(m)}}{1 + \chi^{(m)}} \delta_{ij}. \tag{2.30}$$

The auxiliary fields are then related to the macroscopic fields through the scalar susceptibilities by

$$D_i = \epsilon_0 (1 + \chi^{(e)}) E_i \tag{2.31}$$

$$B_i = \mu_0 (1 + \chi^{(m)}) H_i. \tag{2.32}$$

It is common practice to define the electric and magnetic indices n_e and n_m which are related to scalar susceptibilities through

$$n_e = \sqrt{1 + \chi^{(e)}} \tag{2.33}$$

$$n_m = \sqrt{1 + \chi^{(m)}}. \tag{2.34}$$

One further abstraction is to introduce the refractive index which is defined by

$$n = n_e n_m. \tag{2.35}$$

Most mediums of interest in optics are non-magnetic so that $n_m \approx 1$, in which case the refractive index is determined solely by the electric index. In this case the auxiliary fields reduce to

$$D_i = \epsilon_0 n^2 E_i \tag{2.36}$$

$$B_i = \mu_0 H_i, \tag{2.37}$$

and the wave equation (2.12) becomes

$$\vec{\nabla}^2 \vec{E} - \frac{n^2}{c^2} \frac{\partial^2 \vec{E}}{\partial t^2} = 0. \tag{2.38}$$

2.2 Gratings

In this work the principle interest in gratings is their ability to generate slow light. In section both the properties of Bragg gratings and moiré gratings are introduced.

2.2.1 Bragg gratings

2.2.1.1 Coupled mode equations from Maxwell's equations

To understand how a Bragg grating produces slow light, it is first necessary to find solutions for wave propagation through them using Maxwell's equations. One of the key approaches to extracting analytical solution is to use coupled mode theory [38]. A detailed derivation of Bragg grating solutions in $3+1$ dimensions can be found in [39] and [40]. Here we only require a single mode treatment in $1+1$ dimensions. It is useful to provide a brief derivation of the coupled mode equations as it illustrates where many of the important quantities come from and what underlying assumptions and approximations have been made. To start we have the refractive index profile for a Bragg grating which is given by

$$n(z) = \bar{n} + \delta n \cos\left(\frac{2\pi z}{\Lambda_B}\right), \tag{2.39}$$

where $\bar{n}$ is the effective refractive index, δn is the grating strength and Λ_B is the Bragg period. It is common to refer to $\bar{n}$ and δn as the DC an AC components respectively. To develop the coupled mode equations, the following electric field ansatz is proposed

$$E(t,z) = U(z)e^{i(\beta z - \omega t)} + V(z)e^{-i(\beta z + \omega t)}. \tag{2.40}$$

The ansatz is monochromatic with angular frequency ω and propagation constant $\beta = \bar{n}k$ where the wavenumber k is related to the angular frequency through the dispersion relation (1.1). The field is composed into forward and backward modes where $U(z)$ and $V(z)$ are the forward and backward mode envelopes respectively. The envelopes are position dependent only so that they correspond to steady state solutions. Substituting the ansatz (2.40) into the wave equation (2.38) and evaluating the time derivatives only, reduces the wave equation to the Helmholtz equation

$$\left(\frac{\partial^2}{\partial z^2} + n^2k^2\right)E(z) = 0, \tag{2.41}$$

and the ansatz becomes

$$E(z) = U(z)e^{i\beta z} + V(z)e^{-i\beta z}. \tag{2.42}$$

There are a number of approximation that go into deriving the coupled mode equations. The first is a slowly varying envelope approximation. This approximation assumes that the pulse envelope varies slowly compared to the underlying wavelength. As a consequence the magnitude of the second derivatives become small so that for the ansatz (2.42)

$$\left|k\frac{\partial U(z)}{\partial z}\right| \gg \left|\frac{\partial^2 U(z)}{\partial z^z}\right| \tag{2.43}$$

$$\left|k\frac{\partial V(z)}{\partial z}\right| \gg \left|\frac{\partial^2 V(z)}{\partial z^z}\right|. \tag{2.44}$$

Only the first derivatives of the envelope function are then required to capture the behaviour of the system. Then substituting the ansatz (2.42) into the Helmholtz equation (2.41) and making a slowly varying envelope approximation gives the following expression

$$e^{i\beta z}\left(2i\beta\frac{\partial}{\partial z} - \beta^2 + n^2k^2\right)U(z) - e^{-i\beta z}\left(2i\beta\frac{\partial}{\partial z} + \beta^2 - n^2k^2\right)V(z) = 0. \tag{2.45}$$

The next step is to multiply equation (2.45) by $e^{-i\beta z}$ and rearrange to give

$$\frac{\partial U(z)}{\partial z} = i\frac{k}{2\bar{n}}\left(n^2 - \bar{n}^2\right)\left(U(z) + e^{-2i\beta z}V(z)\right) + e^{-2i\beta z}\frac{\partial V(z)}{\partial z}, \tag{2.46}$$

and then do same again but this time multiply (2.45) by $e^{-i\beta z}$ to give

$$\frac{\partial V(z)}{\partial z} = -i\frac{k}{2\bar{n}}\left(n^2 - \bar{n}^2\right)\left(e^{2i\beta z}U(z) + V(z)\right) + e^{2i\beta z}\frac{\partial U(z)}{\partial z}. \tag{2.47}$$

Equations (2.46) and (2.46) provide the basis for the coupled mode equations. The equations contain the square of the refractive index, which by the Bragg grating index profile (2.39) is given by

$$n^2 = \bar{n}^2 + \bar{n}\delta n\left(e^{iK_B z} + e^{-iK_B z}\right) + \frac{\delta n^2}{4}\left(e^{iK_B z} + e^{-iK_B z}\right)^2, \tag{2.48}$$

where the Bragg grating wavenumber is given by

$$K_B = \frac{2\pi z}{\Lambda_B}. \tag{2.49}$$

As the grating strength is small, a neglecting small terms approximation can be made giving

$$n^2 \approx \bar{n}^2 + \bar{n}\delta n\left(e^{iK_B z} + e^{-iK_B z}\right). \tag{2.50}$$

Then substituting (2.50) into equations (2.46) and (2.47) yields

$$\frac{\partial U(z)}{\partial z} = i\kappa\left(e^{iK_B z} - e^{-iK_B z}\right)U(z) + i\kappa\left(e^{-2i\Delta z} - e^{-i(K_B+2\beta)z}\right)V(z) + e^{-2i\beta z}\frac{\partial V(z)}{\partial z} \tag{2.51}$$

$$\frac{\partial V(z)}{\partial z} = -i\kappa\left(e^{i(K_B+2\beta)z} - e^{2i\Delta z}\right)U(z) - i\kappa\left(e^{iK_B z} - e^{-iK_B z}\right)V(z) + e^{2i\beta z}\frac{\partial U(z)}{\partial z}, \tag{2.52}$$

where the detuning Δ and the coupling constant κ are defined by

$$\Delta = \frac{2\beta - K_B}{2} = \beta - \frac{\pi}{\Lambda_B} \tag{2.53}$$

$$\kappa = \frac{k\delta n}{2}. \tag{2.54}$$

To reduce equations (2.51) and (2.52) down to their final forms, a rotating wave approximation needs to made [41]. This approximation works on the basis that as the rate of oscillation of a wave increases, its mean value tends to zero. Therefore, when a wave is fast oscillating relative to another, it is contribution can be neglected. Looking again at equations (2.51) and (2.52), as the detuning becomes small so that $e^{-2i\Delta z} \approx e^{2i\Delta z} \approx 1$, all the other wave terms become fast oscillating and rotating wave approximations can be made, giving the final form of the coupled mode equations

$$\frac{dU(z)}{dz} = i\kappa V(z)e^{-2i\Delta z} \tag{2.55}$$

$$\frac{dV(z)}{dz} = -i\kappa U(z)e^{2i\Delta z}. \tag{2.56}$$

When the detuning is zero, the Bragg period is related to the Bragg wavelength by

$$\lambda_B = 2\bar{n}\Lambda_B. \tag{2.57}$$

2.2.1.2 Solutions for semi-infinite Bragg gratings

The coupled mode equations (2.55) and (2.56) can be solved using standard methods and have general solutions given by

$$U(z) = c_1 e^{-i(\Delta-\alpha_B)z} + c_2 e^{-i(\Delta+\alpha_B)z} \tag{2.58}$$

$$V(z) = c_1\left(\frac{\alpha_B - \Delta}{\kappa}\right)e^{i(\Delta+\alpha_B)z} - c_2\left(\frac{\alpha_B + \Delta}{\kappa}\right)e^{i(\Delta-\alpha_B)z}, \tag{2.59}$$

and where

$$\alpha_B = \sqrt{\Delta^2 - \kappa^2}. \tag{2.60}$$

and c_1 and c_2 are arbitrary constants. Without applying boundary conditions and fixing the values for c_1 and c_2, the solutions (2.55) and (2.56) correspond to a semi-infinite grating extending from 0 to $\pm\infty$. It is useful to split the electric field ansatz into two terms so that $E(z) = E_1(z) + E_2(z)$, where

$$E_1(z) = c_1\left[e^{i\beta_+ z} + \left(\frac{\alpha_B - \Delta}{\kappa}\right)e^{-i\beta_- z}\right] \tag{2.61}$$

$$E_2(z) = c_2\left[e^{i\beta_- z} + \left(\frac{\alpha_B + \Delta}{\kappa}\right)e^{-i\beta_+ z}\right] \tag{2.62}$$

As the goal here is to understand how Bragg gratings generate slow light, writing the electric field in this form shows how the propagation constant has been modified by the inclusion of the grating. The grating has produced two modified versions of the propagation constant which are given by

$$\beta_\pm = \frac{\pi}{\Lambda_B} \pm \alpha_B. \tag{2.63}$$

Both of the propagation constants become complex when

$$\kappa^2 > \Delta^2 \tag{2.64}$$

due to the quantity α_B becoming imaginary. Consequently this leads to exponentially decreasing solutions which creates a band gap for wavelengths satisfying equation (2.64). The edges of the band gap can be found by solving the equation $\alpha_B = 0$, which results in the quadratic equation

$$\frac{\lambda^2}{4\Lambda_B^2} - \frac{\bar{n}\lambda}{\Lambda_B} + \bar{n}^2 + \left(\frac{\delta n}{2}\right)^2 = 0, \tag{2.65}$$

and which has solutions

$$\lambda_\pm = \Lambda_B(2\bar{n} \pm \delta n). \tag{2.66}$$

The wavelengths λ_+ and λ_- correspond to the top and bottom of the band gap respectively. The centre of the band gap is then given by

$$\lambda_B = \frac{\lambda_+ + \lambda_-}{2} = 2\Lambda\bar{n} \tag{2.67}$$

which corresponds to the Bragg wavelength. The rejection bandwidth is given by

$$\frac{\lambda_+ - \lambda_-}{2} = 2\Lambda_B\delta n, \tag{2.68}$$

showing that the size of the band gap is proportional to the AC modulation of the refractive index. The definition of the group velocity is given by equation (1.7) and is the inverse derivative of the propagation constant with respect to the angular frequency. Using the modified propagation constants (2.63), the group velocity evaluates to

$$v_{g\pm} = \pm\left(\frac{\partial \alpha_B}{\partial \omega}\right)^{-1} = \pm v_p\left(\frac{2\bar{n}\alpha_B}{2\bar{n}\Delta - \delta n\kappa}\right) \tag{2.69}$$

Similarly the group delay dispersion (1.9) can be calculated from the second derivative of the modified propagation constants with respect to the angular frequency, giving

$$D_\pm = \pm\frac{\pi^3 \delta n^2}{2c\Lambda_B^2 \lambda^2 \alpha_B^3}. \tag{2.70}$$

The group velocity given by equation (2.69) tends as expected to the phase velocity v_p as the coupling κ tends to zero, which is effectively switching the grating off. The reduction in group velocity which leads to slow light comes from the factor α_B tending to zero. As we saw before $\alpha_B = 0$ corresponds to the band edges and so the group velocity tends to zero as the wavelength approach one of the band edges. The expression for the group velocity also has a singularity which occurs when $2\bar{n}\Delta - \delta n\kappa \to 0$. This corresponds to the wavelength

$$\lambda_\infty = \frac{\lambda_+\lambda_-}{\lambda_B} = \lambda_B\left(1 - \frac{\delta n^2}{4\bar{n}^2}\right). \tag{2.71}$$

If we consider a forward propagating pulse with a positive group velocity, then when $\lambda < \lambda_\infty$, the propagation constants β_+ and $-\beta_-$ provide physically meaningful solutions. Similarly, when $\lambda > \lambda_\infty$, the propagation constants $-\beta_+$ and β_- provide physically meaningful solution. This corresponds to a semi-invite grating starting at zero and extending out to infinity. The group velocity can then be defined by

$$v_g = \begin{cases} v_{g+} & \lambda < \lambda_\infty \\ v_{g-} & \lambda > \lambda_\infty, \end{cases} \tag{2.72}$$

and the group delay dispersion by

$$D = \begin{cases} D_+ & \lambda < \lambda_\infty \\ D_- & \lambda > \lambda_\infty. \end{cases} \tag{2.73}$$

Figure 2.1a shows a plot of both the group velocities (2.72). As the wavelength approaches either side of the rejection band, the group velocity decreases rapidly to zero

producing slow light. Figure 2.1b shows the accompanying group delay dispersion. Again at the band edges, the group delay dispersion is very strong and diverges rapidly. This means that slow light induced by a Bragg grating will also result in significant pulse broadening.

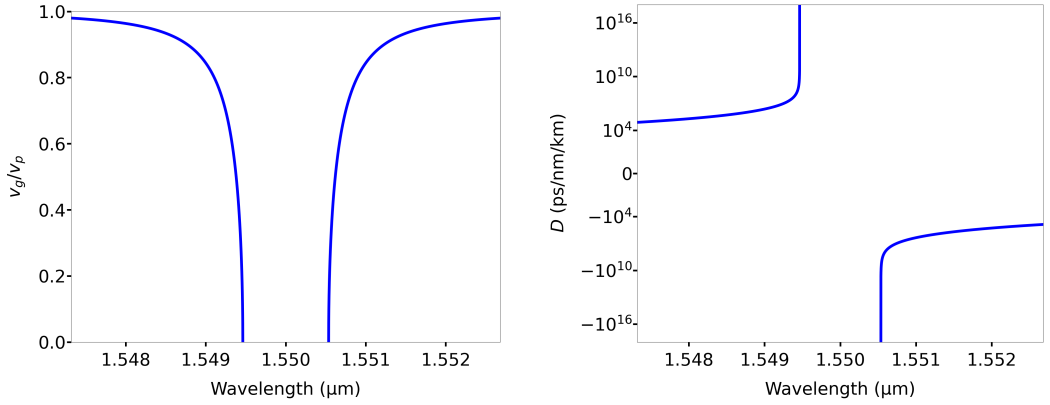

(a) (b)

FIGURE 2.1: (a) The group velocity v_g and (b) group delay dispersion D for a semi-infinite Bragg grating with parameters $\lambda_B = 1550\,\text{nm}$, $\bar{n} = 1.445$, $\delta n = 10^{-3}$ and $\Lambda = 2\bar{n}/\lambda_B$.

As has been demonstrated, the band gap leads to exponentially decaying solutions which couple the incoming power into the backwards propagating mode. The amount of incoming power reflected by the grating by coupling into the backwards mode can by quantified by the reflectance which is defined by

$$R = \left| \frac{V(0)}{U(0)} \right|^2 \tag{2.74}$$

As before, careful attention has to be paid in order to extract a physically meaningful solution for a forward propagating pulse. By carefully inspecting the electric fields (2.61) and (2.62), the reflectance can be defined either side of the singular wavelength (2.71) by

$$R = \begin{cases} \left| \frac{\alpha_B - \Delta}{\kappa} \right|^2 & \lambda < \lambda_\infty \\ \left| \frac{\alpha_B + \Delta}{\kappa} \right|^2 & \lambda > \lambda_\infty. \end{cases} \tag{2.75}$$

Figure 2.2 shows a plot of the reflectance (2.75). Within the band gap the grating is strongly reflecting so that all the incoming light is coupled into the backward modes. Outside the band gap the reflectance decreases rapidly. As the grating is semi-infinite, there are no finite length interference effects causing side lobing which will be looked at in section 2.2.2.

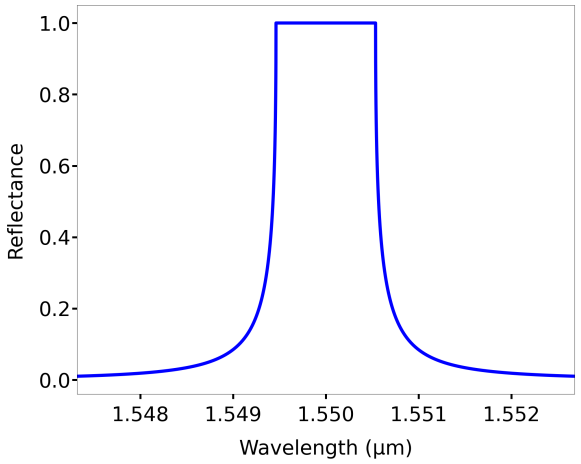

FIGURE 2.2: Plot of the reflectance for a semi-infinite Bragg grating with parameters $\bar{n} = 1.445$, $\delta n = 10^{-3}$, λ_B =1550 nm.

2.2.1.3 Solutions for finite Bragg gratings

The previous section looked at Bragg grating solutions without applying boundary conditions which corresponded to semi-inifite gratings. Here we look at solutions where realistic boundary conditions are imposed, which correspond to finite length gratings. If the initial amplitude of the field entering the grating is A, then this imposes the boundary condition $U(0) = A$. If the grating has a length L, then to ensure no light is coupled into the end of the grating the boundary condition $V(L) = 0$ is required. These boundary conditions fix the constants in solutions (2.58) and (2.59) which are then given by

$$c_1 = \frac{A}{\Gamma e^{2i\alpha_B L} + 1} \tag{2.76}$$

$$c_2 = \frac{\Gamma A e^{2i\alpha_B L}}{\Gamma e^{2i\alpha_B L} + 1} \tag{2.77}$$

where

$$\Gamma = \frac{\alpha_B - \Delta}{\alpha_B + \Delta} \tag{2.78}$$

Consider the solutions (2.58) and (2.59) with these boundary conditions at the Bragg wavelength λ_B. In this case $\Delta = 0$, $\alpha_B = i\kappa$ and $\Gamma = 0$ so that the constants become

$$c_1 = \frac{A}{e^{-2\kappa L} + 1} \tag{2.79}$$

$$c_2 = \frac{Ae^{-2\kappa L}}{e^{-2\kappa L} + 1}. \tag{2.80}$$

The solutions (2.58) and (2.59) at the start of the grating at the Bragg wavelength reduce to

$$U(0) = c_1 + c_2 = A \tag{2.81}$$

$$V(0) = i(c_1 - c_2) = iA \tanh \kappa L \tag{2.82}$$

By equation (2.74), the reflectance is then given by

$$R = \tanh^2(\kappa L) \tag{2.83}$$

which corresponds to the maximum reflectance of the grating. The reflectance can be increased by either increasing the length of grating L or the coupling strength κ.

2.2.2 Grating apodisation

The reflectance for a semi-inifite grating shown in figure 2.2 does not exhibit any side-lobing. This is in contract to a grating of finite length, where the reflectance as shown in figure 2.3a has characteristic oscillations.

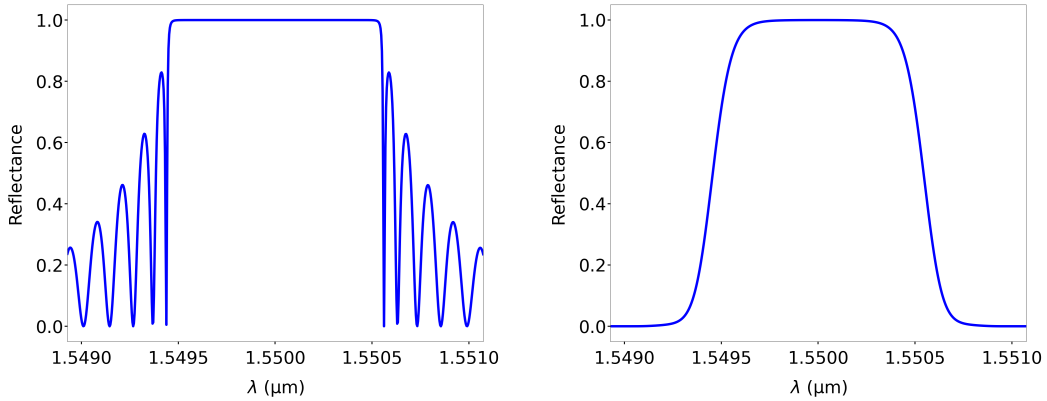

FIGURE 2.3: Bragg grating reflectance with (a) no apodisation applied and (b) a Gaussian apodisation with $\alpha_A = 16$. Additional parameters $\lambda_B = 1550\,\text{nm}$, $\bar{n} = 1.445$, $\delta n = 10^{-3}$ and $L = 5\,\text{mm}$.

This behaviour can be understood by considering a grating profile of the form

$$n(z) = \bar{n} + \delta n \, f(z) \cos(2\pi z/\Lambda_B) \tag{2.84}$$

where $f(z)$ is an apodisation function. For a finite Bragg grating considered in the previous section, the apodisation function can be taken to be a square wave with $f(z) = 1$ along the length of the grating. The Fourier transform of a square wave is a sinc function which has the form $\text{sinc}(a) = \sin(a)/a$. This leads to oscillations as a function of the wavenumber which manifests in reflectance as the sidelobing.

As the sidelobing is due to the profile of the apodisation, an appropriate profile can be choosen to suppress it. A commonly used profile is a Gaussian of the form

$$f(z) = e^{-\alpha_A (z-z_0)^2/L^2} \tag{2.85}$$

where α_A is the apodisation strength. The Fourier transform of a Gaussian is a Gaussian and so the apodisation smooths out the sidelobing. With $\alpha_A = 0$ the profile reduces to a square wave so that no sidelobing suppression is applied. As α_A increases the amount of sidelobing suppression also increases. Increasing α_A also results in decreasing the average coupling strength of the grating. From equation (2.83) this results in reduction in the overall reflectance of the grating. Therefore, applying an apodisation is a trade off between sidelobe suppression and the overall reflectance of the grating. To increase the reflectance of an apodised grating it is necessary to make it longer, which again can be seen from equation (2.83).

2.2.3 Moiré and superstructure gratings

We have seen that a Bragg grating induces slow light at wavelengths approaching the band gap and that this is accompanied by strong group delay dispersion causing pulse broadening. At wavelengths approaching the start of the band gap, the second order dispersion is anomalous and at wavelengths approaching the end of the band gap the dispersion is normal. This suggests that by superimposing two grating periods, a dual band gap structure can be created with a transmission band that cancels second order dispersion with a zero dispersion wavelength at its centre. If the transmission band is sufficiently small, then the dispersion generated from the band edges will generate slow light within the transmission band. Such a grating is called a moiré grating [35, 36] and is given by the grating index profile

$$n = \bar{n} + \frac{\delta n}{2} \, f(z) \left[\cos\left(\frac{2\pi z}{\Lambda_1}\right) + \cos\left(\frac{2\pi z}{\Lambda_2}\right) \right], \tag{2.86}$$

where Λ_1 and Λ_2 are the two grating periods. A moiré grating is an example of a superstructure grating and can be written in the form

$$n(z) = \bar{n} + \delta n a(z) \cos\left(\frac{2\pi z}{\Lambda_B}\right), \tag{2.87}$$

where $a(z)$ is a superstructure envelope. The general property of a superstructure envelope is that it is periodic with a superstructure period Λ_S

$$a(z + \Lambda_S) = a(z). \tag{2.88}$$

In the case of the moiré grating, the superstructure envelope is given by

$$a(z) = \cos\left(\frac{2\pi z}{\Lambda_S}\right), \tag{2.89}$$

so that the grating periods Λ_1 and Λ_2 are related to grating periods Λ_S and Λ_B by

$$\Lambda_S = \frac{\Lambda_1 \Lambda_2}{\Lambda_2 - \Lambda_1} \tag{2.90}$$

$$\Lambda_B = \frac{\Lambda_1 \Lambda_2}{\Lambda_2 + \Lambda_1}, \tag{2.91}$$

where $\Lambda_2 > \Lambda_1$. The grating period Λ_B is as before the Bragg period. Therefore a moiré grating can also be thought of as a Bragg grating composed with a sinusoidal envelope. Developing coupled mode equations to describe the moiré grating is then quite straight forward. Provided that the moiré envelope (2.89) is slowly varying with respect to the underlying Bragg grating, then following the same analysis as was given in section 2.2.1.2, the coupled mode equations are given by

$$\frac{dU}{dz} = i\kappa f(z) a(z) V e^{-2i\Delta z} \tag{2.92}$$

$$\frac{dV}{dz} = -i\kappa f(z) a(z) U e^{2i\Delta z}. \tag{2.93}$$

The effect of the moiré envelope in the equations leads to a transmission band opening within the rejection band centred on the Bragg wavelength λ_B. Figure 2.4 shows the reflectance for a typical apodised moiré grating.

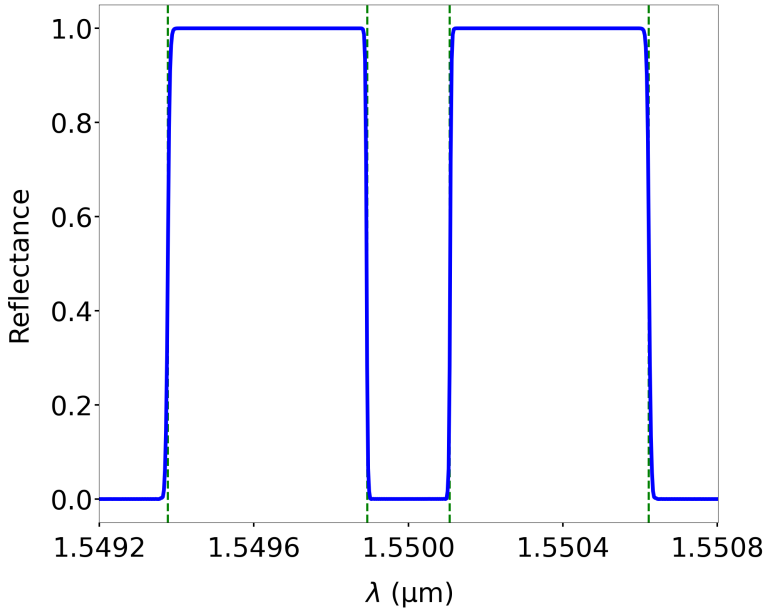

FIGURE 2.4: Reflectance for a Gaussian apodised moiré grating with parameters $\bar{n} = 1.445$, $\delta n = 10^{-3}$, $\lambda_B = 1550\,\text{nm}$, $\Lambda_S = 2.68\,\text{mm}$, $\alpha_A = 16$ and $L = 10\,\text{cm}$.

Applying an apodisation is particularly important with a moiré grating, otherwise sidelobing will occur within the transmission band.

The two different ways to express the moiré grating profile (2.87) and (2.89), give two different ways to think about the grating. Either as two separated Bragg gratings or as a single Bragg grating with a transmission window. The validity of these two view points is discussed in more detail in Chapter 4.

If looked at as two separate Bragg gratings, the size of the transmission band separating the two rejection bands gets smaller as the difference between the grating period Λ_1 and Λ_2 is reduced. By equation (2.90), this corresponds to a larger moiré period. Therefore, a narrower transmission band results from a slower oscillating moiré envelope. As the transmission band narrows the group velocity within the transmission band reduces. Figure 2.5a shows the group velocity produced by a moiré grating calculated using equation (3.78) which is discussed in more detail in chapter 3. Just as with a Bragg grating, at the band edges the group velocity tends to zero. Within the transmission band the group velocity is reduced but in contrast to a Bragg grating there is a cancellation of second order dispersion which can be seen in figure 2.5b. This means that the moiré grating produces not a only a slow light resonance but also can compensate second order pulse broadening effects.

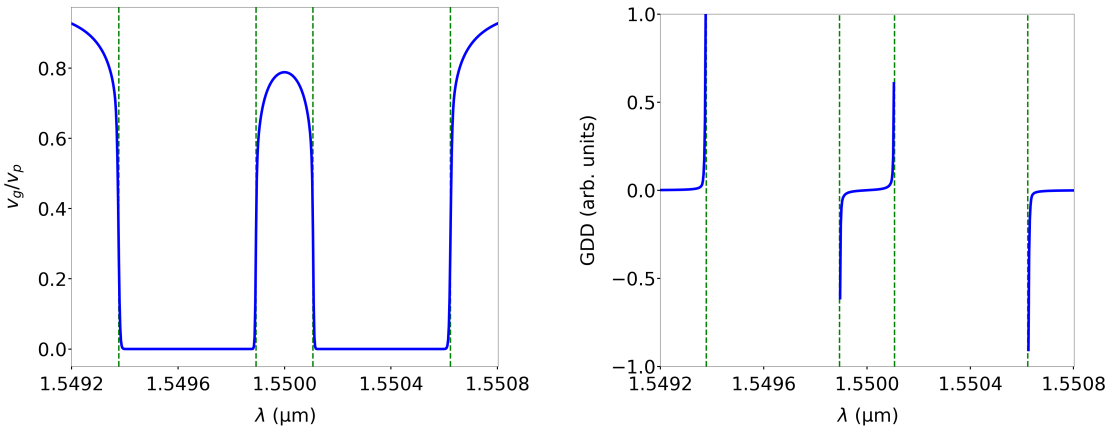

(a) (b)

FIGURE 2.5: (a) Group velocity and (b) group delay dispersion for a Gaussian apodised moiré grating with parameters the same as in figure 2.4

2.3 Nonlinear optics

In section 2.1.4 matter was introduced into Maxwell's equations that responded linearly to the applied fields. In general, however, matter can respond to an applied field nonlinearly. If an applied electric is not too large then the nonlinear response can be expressed as a Taylor series of the polarisation giving

$$P_i = \epsilon_0 \chi^{(1)}_{ij} E_j + \chi^{(2)}_{ijk} E_j E_k + \chi^{(3)}_{ijkl} E_j E_k E_l + ... \tag{2.94}$$

The nonlinear susceptibility tensors $\chi^{(2)}_{ijk}$ and $\chi^{(3)}_{ijkl}$ quantify the strength of the interaction between the medium and the square and the cubic of the applied field respectively. In general, as the order of interaction increases, the strength decreases by many orders of magnitude. Therefore, much of nonlinear optics is concerned with second and third order processes. In this work we are interested in second-harmonic generation through a second order interaction and the Kerr effect through a third order interaction.

2.3.1 Second-harmonic generation and periodic poling

Second-harmonic generation (SHG) is a second order nonlinear interaction which converts a fundamental mode of frequency ω to the second-harmonic with frequency 2ω [42, 43]. The strength of a second order interaction is characterised by the nonlinear $\chi^{(2)}$ susceptibility tensor. $\chi^{(2)}$ is very weak in comparison to the linear $\chi^{(1)}$ susceptibility and as a consequence either long device lengths or high intensities are required to achieve efficient SHG. A set of coupled mode equation can be derived which describes

the transfer of power of the fundamental mode U_1 to a second-harmonic mode U_2. The equations are given by [44]

$$\frac{\partial U_1}{\partial z} = -\frac{i\chi^{(2)}\omega_1}{c\bar{n}_1} U_2 U_1^* e^{i\Delta_\beta z} \tag{2.95}$$

$$\frac{\partial U_2}{\partial z} = -\frac{i\chi^{(2)}\omega_1}{c\bar{n}_2} U_1^2 e^{-i\Delta_\beta z}. \tag{2.96}$$

An important factor affecting conversion efficiency is phase matching between the two modes which is given by

$$\Delta_\beta = \beta_2 - 2\beta_1, \tag{2.97}$$

where β_1 and β_2 are the propagation constants for the fundamental and second-harmonic modes respectively. If Δ_β is large, then the exponential terms will oscillate rapidly with respect to the modes reducing the coupling between them. Therefore, in order to achieve efficient second-harmonic conversion, Δ_β must be close to zero. Unfortunately bulk material dispersion prevents this from happening. There are a number of different techniques that can be used to achieve phase matching, two commonly used approaches are to use either a birefringent nonlinear crystal or to employ quasi-phase-matching (QPM) [45]. This last technique works by periodically modulating the sign of the $\chi^{(2)}$ susceptibility with a period Λ so that

$$\chi^{(2)}(z) = \chi^{(2)}\mathrm{sgn}\big[\sin(2\pi z/\Lambda)\big] \tag{2.98}$$

which introduces an extra wavevector component $2\pi/\Lambda$. The phase matching condition is then modified to $\Delta_\beta = \beta_2 - 2\beta_1 - 2\pi/\Lambda$. Therefore, by setting the poling period to

$$\Lambda = \frac{2\pi}{\Delta_\beta}, \tag{2.99}$$

the phase matching condition is satisfied allowing efficient coupling between the modes. To incorporate the poling into the coupled mode equations (2.95) and (2.96), the poling function (2.98) can be expanded as a Fourier series giving

$$\mathrm{sgn}\big[\sin(2\pi z/\Lambda)\big] = \frac{4}{\pi}\sum_{m=1}^{\infty}\frac{\sin\big(2\pi(2m-1)z/\Lambda\big)}{2m-1}. \tag{2.100}$$

The first order term in the series is the dominant term and so the poling function can be approximated by

$$\chi^{(2)}(z) \approx \frac{2i\chi^{(2)}}{\pi}\left(e^{-i\Delta_\beta z} - e^{i\Delta_\beta z}\right) \tag{2.101}$$

Then substituting equation (2.101) into the coupled mode equations (2.95) and (2.96) and making a rotating wave approximation gives the quasi-phase matched coupled mode equations

$$\frac{\partial u_1}{\partial z} = \frac{4\chi^{(2)}}{\lambda_1 \bar{n}_1} 2u_1^*, \tag{2.102}$$

$$\frac{\partial u_2}{\partial z} = -\frac{4\chi^{(2)}}{\lambda_1 \bar{n}_2} u_1^2. \tag{2.103}$$

2.3.2 Kerr effect

The Kerr effect is a third order $\chi^{(3)}$ nonlinear process which describes the change in the linear refractive index as a result of an externally applied field. The Kerr effect can occur due to an applied optical pump field which is known as the optical Kerr effect, or by an external applied quasi-static electric field known as the electro-optic Kerr effect. These processes are also commonly referred to as the AC and DC Kerr effects respectively. In this work we are concerned only with the optical Kerr effect.

To understand how an applied optical field alters the linear refractive index, consider a nonlinear polarisation of the form

$$P = \epsilon_0 \chi^{(1)} E + \chi^{(3)} E^3. \tag{2.104}$$

If the applied optical field has an electrical field E of the form

$$E = A\cos(\beta z - \omega t), \tag{2.105}$$

the polarisation terms of interest for the Kerr effect are given by

$$P = \epsilon_0 \left(\chi^{(1)} + \frac{3}{4}\chi^{(3)}|A|^2\right) E. \tag{2.106}$$

By equation (2.33), this modifies the refractive index such that

$$n \approx \bar{n} + \frac{3\chi^{(3)}}{8\bar{n}}|A|^2. \tag{2.107}$$

It is more common to express the change in the refractive index using the nonlinear refractive index n_2 and the field intensity I so that

$$n = \bar{n} + n_2 I \tag{2.108}$$

where

$$n_2 = \frac{3\chi^{(3)}}{4\epsilon_0 c\bar{n}^2} \tag{2.109}$$

$$I = \frac{c\epsilon_0\bar{n}}{2}|A|^2 \tag{2.110}$$

This analysis is an example of self phase modulation (SPM), where the refractive index has been varied at the wavelength of the applied field. It causes the applied field to pick up an additional phase shift which causes spectral broadening as the wave propagates. Another Kerr interaction is cross phase modulation (XPM). This is where the refractive index variation at one wavelength of light is induced by another. Typically this involves a strong pump field at a carrier wavelength λ_1 inducing a refractive index change for a weak signal field at a carrier wavelength λ_2. The XPM interaction creates a refractive change which is a factor of two larger than SPM.

Chapter 3

Lagrangian approach to coupled mode theory

In this chapter we apply the methods of the calculus of variations and in particular the Lagrangian formalism to generate coupled mode equations for optical systems. This differs from the usual approach in the field which is to start directly from the wave equation arising from Maxwell's equations as shown in section 2.2.1. Although the Lagrangian approach does not offer any additional physical information as both formalisms describe the same physics, it does offer a systematic way of generating coupled mode equations which can be readily extended to include nonlinear materials. This thesis makes substantial use of coupled mode theory and all further derivation will be made using variational methods.

3.1 Background review of the Lagrangian formalism

As the calculus of variations and the Lagrangian formalism [46, 47, 48] are not standard background material within the field of photonics, this section serves to provide a brief overview of the subject.

3.1.1 Lagrangian mechanics

Lagrangian mechanics is a reformulation of Newtonian mechanics. It was developed by a number of leading figures of 17th and 18th mathematics and physics culminating in the work by Italian-French mathematician Joseph-Louis Lagrange in his two volume treatise Mécanique analytique [49, 50]. It has its origins in optics going back to the work of Fermat and his principle of least time. Fermat observed that a light ray travelling between two points will always take the path that minimises the amount of time taken to

travel between the points. Another related problem that led to the development of the Lagrangian formalism was the brachistochrone problem introduced Johann Bernoulli. Bernoulli made an open challenge to find the curve that minimises the time for an object to travel between two points whilst under the influence of gravity. The challenge was taken up and solved independently by both Leibniz and Newton. It is a well known piece of historical trivia that Newton published his solution anonymously, however, Bernoulli was able to decipher the solver by recognising "the lion by its claw".

What these and other similar systems seemed to have in common was that nature was optimising something. That something is known as the action which was named by the great mathematical physicist William Hamilton and is denoted by the letter S. Every physical system has an action and its dynamical evolution will always extremise the action. This is known as the principle of stationary action and leads to an alternative approach for finding equations of motion using the Euler-Lagrange equations rather than Newton's second law of motion.

To obtain some intuition for the action, consider a space with generalised coordinates q_i and an object travelling through the space on a path $q_i(t)$ between the points A and B. If $q_i(t)$ represents the true path taken by nature, then any other path can written in the form $q_i(t) + \Delta q_i(t)$ where $\Delta q_i(t)$ represents the deviation of a path from the true path. If the true path has an action S, then a deviating path will have an action $S + \Delta S$. Figure 3.1 shows a schematic of the true path and deviations from it. Finding the true path then becomes the problem of finding the path that makes $\Delta S = 0$

To make progress in finding the stationary action, a functional L called the Lagrangian is introduced. It takes as its arguments the positions q_i and velocities $\dot{q}_i$ such that a value can be assigned to each point in time along a path's trajectory. The action can then be expressed as an integral over the Lagrangian

$$S = \int_{t_0}^{t_1} dt\ L\Big(q(t), \dot{q}(t)\Big). \tag{3.1}$$

The problem of finding the stationary action then amounts to finding the extremum of the following expression

$$\delta S = \int_{t_0}^{t_1} dt\ \delta L\Big(q(t), \dot{q}(t)\Big). \tag{3.2}$$

This can be done by making an infinitesimal change to the position δq, and an infinitesimal change to the velocity $\delta \dot{q}$. Substituting the infinitesimal changes into the Lagrangian and Taylor expanding gives

$$L(q + \delta q, \dot{q} + \delta \dot{q}) = L(q, \dot{q}) + \frac{\partial L}{\partial q_i}\delta q_i + \frac{\partial L}{\partial \dot{q}_i}\delta \dot{q}_i, \tag{3.3}$$

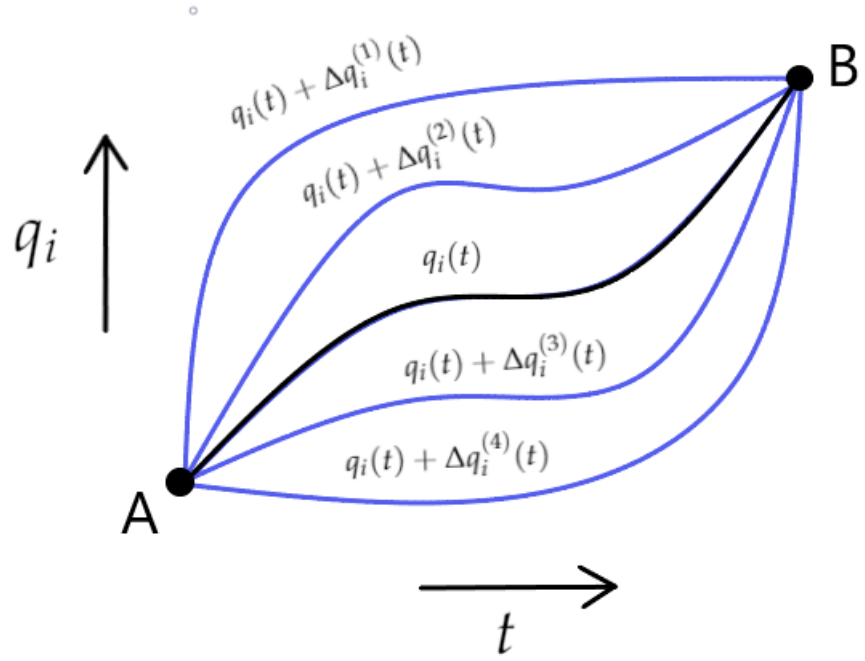

FIGURE 3.1: A schematic of a paths between points A and B. The path indicated by the black line corresponds to the true path taken by nature and blue lines indicate paths that are deviations from the true path

making the change in the Lagrangian

$$\delta L = \frac{\partial L}{\partial q_i}\delta q_i + \frac{\partial L}{\partial \dot{q}_i}\delta \dot{q}_i. \tag{3.4}$$

By using the following application of the chain rule

$$\frac{d}{dt}\left(\frac{\partial L}{\partial \dot{q}_i}\delta q_i\right) = \frac{d}{dt}\left(\frac{\partial L}{\partial \dot{q}_i}\right)\delta q_i + \frac{\partial L}{\partial \dot{q}_i}\delta \dot{q}_i, \tag{3.5}$$

the change in the action can be written as

$$\delta S = \int_{t_0}^{t_1} dt \left(\frac{\partial L}{\partial q_i} - \frac{d}{dt}\left(\frac{\partial L}{\partial \dot{q}_i}\right)\right)\delta q_i + \frac{d}{dt}\left(\frac{\partial L}{\partial \dot{q}_i}\delta q_i\right). \tag{3.6}$$

In equation (3.6) we have the boundary term

$$\int_{t_0}^{t_1} dt \, \frac{d}{dt}\left(\frac{\partial L}{\partial \dot{q}_i}\delta q_i\right) = \frac{\partial L}{\partial \dot{q}_i}\delta q_i \Big|_{t_0}^{t_1}. \tag{3.7}$$

Looking again at figure 3.1, we have by definition that the change in the position δq_i is zero at the start and end the path which occur at times t_0 and t_1 respectively. We can

conclude therefore the boundary term (3.7) is zero and that the change in the action reduced to

$$\delta S = \int_{t_0}^{t_1} dt \left(\frac{\partial L}{\partial q_i} - \frac{d}{dt}\left(\frac{\partial L}{\partial \dot{q}_i} \right) \right) \delta q_i. \tag{3.8}$$

Imposing the principle of stationary action requires that the integrand be zero giving

$$\frac{\partial L}{\partial q_i} - \frac{d}{dt}\left(\frac{\partial L}{\partial \dot{q}_i} \right) = 0, \tag{3.9}$$

which is known as the Euler-Lagrange equation. This equation contains all the dynamical information about the system and is equivalent to Newton's second law of motion. We can make this equivalence explicit by looking at a general Lagrangian of the form

$$L = T(\dot{q}) - V(q) \tag{3.10}$$

where the function T gives the kinetic energy and the function V gives the potential energy. Substituting the Lagrangian (3.10) into Euler-Lagrange equation (3.9) gives

$$\frac{d}{dt}\left(\frac{\partial T}{\partial \dot{q}_i} \right) = -\frac{\partial V}{\partial q_i}. \tag{3.11}$$

Then defining the kinetic energy by $T = m\dot{q}_i^2/2$ and the force by $F_i = -\partial V/\partial q_i$ recovers Newtons second law of motion

$$F_i = m\ddot{q}_i. \tag{3.12}$$

The comparison with Newtons equations shows that the quantity

$$\pi_i = \frac{\partial L}{\partial \dot{q}_i} \tag{3.13}$$

is playing the role of the momentum and is consequently known as the conjugate momentum and is traditionally denoted by π_i.

3.1.2 Lagrangian field theory

So far we have introduced the variational formalisms for mechanical systems, however, electromagnetism is a field theory and therefore in order to describe it using variational

principles the ideas from the previous section need to be generalised for fields [47, 48]. Fortunately only a small amount of additional work is required to do this. Firstly we need to place time and space on an equal footing. This can be done by expressing the Lagrangian in terms of the Lagrangian density $\mathcal{L}$ with the relationship

$$L = \int d^3x \; \mathcal{L}, \tag{3.14}$$

The Lagrangian has units of energy and therefore $\mathcal{L}$ has units of $[energy][length]^{-3}$. It is common practice in field theory to refer to the Lagrangian density as the Lagrangian and therefore it is for the reader to determine what is meant from the context and I shall continue with that convention going forward. The field action can then be written as

$$S = \int d^4x \; \mathcal{L}. \tag{3.15}$$

where the integral measure is short hand notation for

$$\int d^4x \equiv \int_{-\infty}^{\infty}\int_{-\infty}^{\infty}\int_{-\infty}^{\infty}\int_{-\infty}^{\infty} dt dq_1 dq_2 dq_3, \tag{3.16}$$

so that the field is integrated over all of space and time. Expressions in field theory can be become long and cumbersome and so simplifying notation is common. One important convention is Greek and Roman indices. Greek indices μ, ν etc run from 0 to 3 with the 0 index being time and the 1, 2, 3 indices being the positions. Roman indices i, j, k etc run from 1 to 3 so run only over positions. It is common practice as well to suppress indices whenever context makes the situation clear and so a set of coordinates x^μ will often be written simply as x.

Finding the Euler-Lagrange equation follows just as before, by making the variation of the field action (3.15) stationary. To do this, the generalised coordinates q_i used for mechanical systems become parameters in a set of generalise fields $\psi_a(t, q_i)$. The same is done for velocities $\dot{q}_i$ by generalising them to partial derivatives of the fields $\partial_\mu \psi_a(t, q_i)$. With short hand these can be written as $\psi_a(x)$ and $\partial_\mu \psi_a(x)$. The derivative has been expressed using relativistic notation so that $\partial_\mu = (\frac{1}{c}\partial_t, \partial_i)$. While it is convenient to work with relativistic notation, it turns out that the subsequent results hold equally well for non-relativistic field theories.

The Lagrangian is now a function of the fields and 4-derivatives $\mathcal{L}\big(\psi_a(x), \partial_\mu \psi_a(x)\big)$. Deriving the Euler-Lagrange equations follows from making infinitesimal transformations of the fields to $\psi_a(x) + \delta\psi_a(x)$ and $\partial_\mu \psi(x) + \delta\partial_\mu \psi(x)$. Then requiring that the action is stationary leads to the following Euler-Lagrange equations

$$\frac{\partial \mathcal{L}}{\partial \psi_a} - \partial_\mu \left(\frac{\partial \mathcal{L}}{\partial_\mu \psi_a} \right) = 0. \tag{3.17}$$

The factors of c in the partial derivatives cancel and so equation (3.17) can be equally written in its non-relativistic form by

$$\frac{\partial \mathcal{L}}{\partial \psi_a} - \partial_t \left(\frac{\partial \mathcal{L}}{\partial_t \psi_a} \right) - \partial_i \left(\frac{\partial \mathcal{L}}{\partial_i \psi_a} \right) = 0. \tag{3.18}$$

The conjugate field momentum is defined by

$$\pi_a = \frac{\partial \mathcal{L}}{\partial_t \psi_a}, \tag{3.19}$$

which is of course an important quantity in the Hamiltonian formulation and in canonical quantisation. Solving the Euler-Lagrange field equations gives the equations of motion for the fields. The analysis so far has only been applied to a scalar field $\psi(x)$, but the formalism can be equally applied to a 3-vector field, a 4-vector field, a spinor field or any other exotic field type. The only restriction is that Lagrangian must be dimensionally consistent and a scalar so that all of the field components must be properly contracted.

When considering the mechanical Lagrangian given by (3.10), the Lagrangian is the difference between kinetic and potential energy. In field theory this idea is generalised so that the Lagrangian is given by

$$\mathcal{L} = \mathcal{L}_{free} + \mathcal{L}_{int}, \tag{3.20}$$

which is the sum of the free and interacting parts of the Lagrangian.

3.1.3 Stress-energy tensor

The conservation of energy and momentum can be generalised to fields by the stress-energy tensor which in a general form is given by

$$T^{\mu\nu} = \frac{\partial \mathcal{L}}{\partial(\partial_\mu \psi_a)} \partial^\nu \psi_a - g^{\mu\nu} \mathcal{L}. \tag{3.21}$$

where $g^{\mu\nu}$ is the metric. The field energy density corresponds to the zero zero component of the stress-energy tensor

$$\mathcal{H} = T^{00} \tag{3.22}$$

and the field momentum density corresponds to

$$P_i = T^{i0}. \tag{3.23}$$

For the the stress-energy tensor to conserve angular momentum, it is a necessary condition that it be symmetric [47]. Therefore the field momentum density should also be equal to the T^{0i} components. In general, however, the stress-energy tensor (3.21) will not be symmetric. Electromagnetism is one such example where this is the case. There is a level of ambiguity to the way the stress-energy tensor is defined and it is possible to add an additional term to the stress-energy tensor to make it symmetric [48]. However, it is not of particular importance to us here so the above definitions of the energy and momentum densities are sufficient.

The stress-energy tensor obeys a set of 4 continuity equations given by

$$\partial_\mu T^{\mu\nu} = 0. \tag{3.24}$$

The one of principle interest in electromagnetism come from setting $\nu = 0$

$$\partial_\mu T^{\mu 0} = \frac{1}{c}\partial_t \mathcal{H} + \partial_i P_i, \tag{3.25}$$

then defining the Poynting vector by

$$S_i = cP_i \tag{3.26}$$

the continuity equations leads to Poynting's theorem

$$\frac{\partial \mathcal{H}}{\partial t} = -\vec{\nabla} \cdot \vec{S}. \tag{3.27}$$

3.1.4 The electromagnetic Lagrangian

Electromagnetism is a Lorentz invariant theory and therefore its Lagrangian should be constructed out of Lorentz invariant scalar quantities. This ensures that the resulting equations of motion are the same in every reference frame. There are two fundamental electromagnetic Lorentz invariants:

$$\epsilon_0 E_i E_i - \frac{1}{\mu_0} B_i B_i \tag{3.28}$$

and

$$\sqrt{\frac{\epsilon_0}{\mu_0}} E_i B_i \tag{3.29}$$

which both have units of energy per unit volume so are viable candidates for a Lagrangian density. It turns out that the first invariant (3.28) as a Lagrangian gives Gauss's law and Ampere's law and the second invariant gives Gauss's law for magnetism and Faraday's law. However, only the first invariant is typically used to construct the Lagrangian. The standard electromagnetic Lagrangian written in non-relativistic notation is then given by

$$\mathcal{L} = \frac{\epsilon_0}{2} E_i E_i - \frac{1}{2\mu_0} B_i B_i \tag{3.30}$$

It is more common to see it written in relativistic notation by

$$\mathcal{L} = -\frac{1}{4\mu_0} F_{\mu\nu} F^{\mu\nu}, \tag{3.31}$$

where $F_{\mu\nu}$ is the electromagnetic field tensor defined by

$$F^{\mu\nu} = \begin{bmatrix} 0 & -E_x/c & -E_y/c & -E_z/c \\ E_x/c & 0 & -B_z & B_y \\ E_y/c & B_z & 0 & -B_x \\ E_z/c & -B_y & B_x & 0 \end{bmatrix}. \tag{3.32}$$

The electromagnetic Lagrangian is Lorentz invariant so that transforming the electric and magnetic fields by any arbitrary Lorentz transformation will result in the same Lagrangian. The relativist form given by equation (3.31) is also called the covariant formulation. This is because the fully contracted upstairs and downstairs 4 indices explicitly imply Lorentz invariance.

The Lagrangians (3.30) and (3.31) describe electromagnetism in vacuum, with no interactions so that the Lagrangians constitute only $\mathcal{L}_{free}$. Matter can be incorporated into (3.30) by adding the linear matter susceptibilities as follows

$$\mathcal{L} = \frac{\epsilon_0}{2} (\delta_{ij} + \chi^{(e)}_{ij}) E_i E_j - \frac{1}{2\mu_0} (\delta_{ij} - \chi^{(m)}_{ij}) B_i B_i. \tag{3.33}$$

Adding matter incorporates interactions into the Lagrangian so that

$$\mathcal{L}_{int} = \chi_{ij}^{(e)} E_i E_j + \chi_{ij}^{(m)} B_i B_i. \tag{3.34}$$

However, adding matter to electromagnetism breaks Lorentz invariance, which is a well known feature of Maxwell's matter equations. The general explanation for this is that adding matter picks out the reference frame in which the matter is at rest. Therefore the matter Lagrangian (3.33) cannot be faithfully written in a covariant form like equation (3.31). This is not a problem for the purposes of this work, as previously discussed the Euler-Lagrange field equations work equally well for non-relativistic fields.

Both Lagrangians (3.30) and (3.33) as they are written do not contain dynamical terms and so the Euler-Lagrange field equations cannot be directly applied to them. In order to make them dynamical the electric and magnetic fields must be substituted for the scalar and vector potentials given in equations (2.22) and (2.23). The equations of motion then follow from varying the Lagrangian with respect to the potentials.

It is convenient to assume that the matter susceptibilities in the Lagrangian (3.33) are dispersionless. As the Lagrangian is written in the time domain, the dispersion could be taken into account by making the susceptibilities time dependent. However, when applying the Euler-Lagrange equations this would lead to time derivatives of the susceptibilities. Therefore, the susceptibilities in the Lagrangian and in Maxwell's equations would be related through differential equations. As the rest of the work in this thesis focuses on small spectral widths where structural dispersion is dominant, it is convenient to approximate the Lagrangian matter susceptibility as being dispersionless.

3.2 Lagrangian methods in a nonlinear medium

This section looks to extended the electromagnetic matter Lagrangian to non-linear materials and show that the resulting equations of motion give the well known Maxwell equations for non-linear materials. While nonlinear Lagrangian field theories form the foundation of the standard model of particle physics [51], I have been unable to locate in the literature their application for nonlinear optics in the form given subsequently in this section. Therefore, to the best of my knowledge the following section represents a novel contribution.

3.2.1 The nonlinear electromagnetic Lagrangian

The linear matter Lagrangian given by equation (3.33) can be extended to include nonlinear materials by incorporating the nonlinear matter susceptibilities. The Lagrangian must be a scalar, so all of the susceptibility indices must be fully contracted and each term must have units of energy density. The process of deducing a Lagrangian is to effectively work backwards from known equations of motion and find the Lagrangian which when varied gives back the equations of motion. For the nonlinear Maxwell equations the appropriate form of the Lagrangian incorporating 2nd and 3rd order nonlinearities is given by

$$\mathcal{L} = \frac{\epsilon_0}{2}(\delta_{ij} + \chi^{(1)}_{ij})E_iE_j - \frac{1}{2\mu_0}B_iB_i + \frac{\epsilon_0}{3}\chi^{(2)}_{ijk}E_iE_jE_k + \frac{\epsilon_0}{4}\chi^{(3)}_{ijkl}E_iE_jE_kE_l, \tag{3.35}$$

where the interacting part of the Lagrangian is now given by

$$\mathcal{L}_{int} = \chi^{(e)}_{ij}E_iE_j + \chi^{(m)}_{ij}B_iB_i + \frac{\epsilon_0}{3}\chi^{(2)}_{ijk}E_iE_jE_k + \frac{\epsilon_0}{4}\chi^{(3)}_{ijkl}E_iE_jE_kE_l. \tag{3.36}$$

In order to incorporate dynamic terms, just as before the electric and magnetic fields need to expressed in terms of the scalar and vector potentials given by equations (2.22) and (2.23). The Lagrangian then becomes

$$\begin{aligned}\mathcal{L} = \frac{\epsilon_0}{2}(\delta_{ij} + \chi^{(1)}_{ij})(\partial_i\phi + \partial_tA_i)(\partial_j\phi + \partial_tA_j) - \frac{1}{2\mu_0}\partial_iA_j(\partial_iA_j - \partial_jA_i)\\ - \frac{\epsilon_0}{3}\chi^{(2)}_{ijk}(\partial_i\phi + \partial_tA_i)(\partial_j\phi + \partial_tA_j)(\partial_k\phi + \partial_tA_k)\\ + \frac{\epsilon_0}{4}\chi^{(3)}_{ijkl}(\partial_i\phi + \partial_tA_i)(\partial_j\phi + \partial_tA_j)(\partial_k\phi + \partial_tA_k)(\partial_l\phi + \partial_tA_l).\end{aligned} \tag{3.37}$$

In order to recover the equations of motion, the Euler-Lagrange equation must be applied to both the scalar and vector potentials which are given by

$$\frac{\partial\mathcal{L}}{\partial\phi} = \partial_t\left(\frac{\partial\mathcal{L}}{\partial(\partial_t\phi)}\right) + \partial_i\left(\frac{\partial\mathcal{L}}{\partial(\partial_i\phi)}\right) \tag{3.38}$$

$$\frac{\partial\mathcal{L}}{\partial A_i} = \partial_t\left(\frac{\partial\mathcal{L}}{\partial(\partial_tA_i)}\right) + \partial_j\left(\frac{\partial\mathcal{L}}{\partial(\partial_jA_i)}\right). \tag{3.39}$$

Looking first at the scalar potential ϕ, the Lagrangian (3.37) only contains spatial derivatives of ϕ and so

$$\frac{\partial \mathcal{L}}{\partial \phi} = 0 \tag{3.40}$$

$$\frac{\partial \mathcal{L}}{\partial(\partial_t \phi)} = 0. \tag{3.41}$$

The spatial derivative with respect to ϕ is a somewhat more involved calculation the final result of which is

$$\begin{aligned}\frac{\partial \mathcal{L}}{\partial(\partial_i \phi)} = \epsilon_0 \delta_{ij}(\partial_j \phi + \partial_t A_j) + \frac{\epsilon_0}{2}\left(\chi^{(1)}_{ij} + \chi^{(1)}_{ji}\right)(\partial_j \phi + \partial_t A_j) \\ - \frac{\epsilon_0}{3}\left(\chi^{(2)}_{ijk} + \chi^{(2)}_{jik} + \chi^{(2)}_{kji}\right)(\partial_j \phi + \partial_t A_j)(\partial_k \phi + \partial_t A_k) \\ + \frac{\epsilon_0}{4}\left(\chi^{(3)}_{ijkl} + \chi^{(3)}_{jikl} + \chi^{(3)}_{kjil} + \chi^{(3)}_{ljki}\right)(\partial_j \phi + \partial_t A_j)(\partial_k \phi + \partial_t A_k)(\partial_l \phi + \partial_t A_l).\end{aligned} \tag{3.42}$$

Taking the derivative which respect to each of the ϕ fields results in permutations of the susceptibility indices. Therefore if the susceptibilities possess the following symmetry properties

$$\chi^{(1)}_{ij} = \chi^{(1)}_{ji} \tag{3.43}$$

$$\chi^{(2)}_{ijk} = \chi^{(2)}_{jik} = \chi^{(2)}_{kji} \tag{3.44}$$

$$\chi^{(3)}_{ijkl} = \chi^{(3)}_{jikl} = \chi^{(3)}_{kjil} = \chi^{(3)}_{ljki}, \tag{3.45}$$

then the spacial derivative of ϕ can be expressed in terms of the electric field by

$$\frac{\partial \mathcal{L}}{\partial(\partial_i \phi)} = -\epsilon_0(\delta_{ij} + \chi^{(1)}_{ij})E_j + \epsilon_0 \chi^{(2)}_{ijk} E_j E_k - \epsilon_0 \chi^{(3)}_{ijkl} E_j E_k E_l \tag{3.46}$$

$$= -D_i, \tag{3.47}$$

and so we find that the spacial derivative of ϕ is proportional to the auxiliary electric field. Then the Euler-Lagrange equation recovers Gauss's law

$$\partial_i D_i = 0. \tag{3.48}$$

The set of symmetries given in equations (3.43-3.45) are known as the Kleinman symmetries [44]. They are valid in an approximately lossless medium when the input frequency is far from any material resonance. Next we turn to varying (3.37) with respect to vector potential. The Lagrangian only contains terms with time and spatial derivatives of the vector potential and so

$$\frac{\partial \mathcal{L}}{\partial A_i} = 0. \tag{3.49}$$

Calculating the time derivative gives the conjugate momentum, which can be done by noticing that it is equivalent to taking the spacial derivative with respect to ϕ and so

$$\frac{\partial \mathcal{L}}{\partial(\partial_t A_i)} = -D_i. \tag{3.50}$$

The corresponding spatial derivative with respect to vector potential leads to

$$\partial_j\left(\frac{\partial \mathcal{L}}{\partial(\partial_j A_i)}\right) = \frac{1}{2\mu_0}(\partial_i\partial_j A_j - \partial_j\partial_j A_i) \tag{3.51}$$

$$= \epsilon_{ijk}\partial_j B_k. \tag{3.52}$$

Combined with the time derivative of the vector potential (3.50) lead to Amperes law

$$\epsilon_{ijk}\partial_j B_k = \partial_t D_i. \tag{3.53}$$

Therefore, equation (3.35) provides the correct Lagrangian for the nonlinear Maxwell equations provided that the susceptibility tensors satisfy the Kleinman symmetries.

3.2.2 The nonlinear electromagnetic stress-energy tensor

To calculate the stress-energy tensor working with a Lagrangian written in 3-vector notation like equation (3.35) presents a problem. As the Lagrangian does not contain time derivatives of the scalar potential, the conjugate momentum of the scalar potential is zero. Consequently calculating the Hamiltonian directly using equation (3.21) leads to the wrong expression. This problem can be mitigated by working with the covariant formalism but as discussed, this cannot be done when matter is included. Fortunately, there is another solution which is to work in the Weyl gauge. This gauge effectively sets the scalar potential to zero. This is achieved by choosing a gauge field f such that its time derivative is equal the scalar potential $\phi = \partial_t f$. Then when making a gauge

transformation the scalar potential is identically zero leaving only the vector potential. After applying a Weyl gauge transformation, the nonlinear electromagnetic Lagrangian reduces to

$$\begin{aligned}\mathcal{L} = \frac{\epsilon_0}{2}(\delta_{ij} + \chi^{(1)}_{ij})\partial_t A_i \partial_t A_j - \frac{1}{2\mu_0}\partial_i A_j(\partial_i A_j - \partial_j A_i) \\ - \frac{\epsilon_0}{3}\chi^{(2)}_{ijk}\partial_t A_i \partial_t A_j \partial_t A_k + \frac{\epsilon_0}{4}\chi^{(3)}_{ijkl}\partial_t A_i \partial_t A_j \partial_t A_k \partial_t A_l.\end{aligned} \tag{3.54}$$

The Hamiltonian in the Weyl gauge takes the form

$$\mathcal{H} = \frac{\partial \mathcal{L}}{\partial(\partial_t A_i)}\partial_t A_i - \mathcal{L}, \tag{3.55}$$

and after some calculation is given by the expression

$$\begin{aligned}\mathcal{H} = \frac{\epsilon_0}{2}(\delta_{ij} + \chi^{(1)}_{ij})\partial_t A_i \partial_t A_j + \frac{1}{2\mu_0}\partial_i A_j(\partial_i A_j - \partial_j A_i) \\ - \frac{2}{3}\epsilon_0\chi^{(2)}_{ijk}\partial_t A_i \partial_t A_j \partial_t A_k + \frac{3}{4}\epsilon_0\chi^{(3)}_{ijkl}\partial_t A_i \partial_t A_j \partial_t A_k \partial_t A_l.\end{aligned} \tag{3.56}$$

The Hamiltonian can then be written in a more familiar form by expressing it in terms of the electric and magnetic fields

$$\begin{aligned}\mathcal{H} = \frac{\epsilon_0}{2}(\delta_{ij} + \chi^{(1)}_{ij})E_i E_j + \frac{1}{2\mu_0}B_i B_i \\ + \frac{2}{3}\epsilon_0\chi^{(2)}_{ijk}E_i E_j E_k + \frac{3}{4}\epsilon_0\chi^{(3)}_{ijkl}E_i E_j E_k E_l.\end{aligned} \tag{3.57}$$

3.3 Coupled mode equations

This section uses Lagrangian methods to derive the coupled mode equations that are used in the subsequent chapters.

3.3.1 Gauge choice and vector potential ansatz

The main difficulty in developing coupled mode equations from a Lagrangian is determining the form of the scalar and vector potentials. One approach to solve this is to work again in the Weyl gauge so that the scalar potential ϕ is zero. Consider a 1d

model where z denotes the propagation direction, then the vector potential for a general problem can be written as a sum over the modes by

$$A_i = \sum_n a_{i,n}(t,z)e^{ib_n(t,z)} + c.c. \tag{3.58}$$

For the linear gratings previously discussed in sections (2.2.1) and (2.2.3), the vector potential ansatz takes the following form

$$A_z = -\frac{i}{\omega}u(t,z)e^{i(\beta z-\omega t)} - \frac{i}{\omega}v(t,z)e^{-i(\beta z+\omega t)} + c.c, \tag{3.59}$$

where u and v are forward and backward modes respectively. The angular frequency is denoted by ω and β is the propagation constant which is dependent on the underlying effective refractive index. The associated electric field is found by taking the negative time derivative of the vector potential which gives

$$E_x = \left[u(t,z) + \frac{i}{\omega}\partial_t u(t,z)\right]e^{i(\beta z-\omega t)} + \left[v(t,z) + \frac{i}{\omega}\partial_t v(t,z)\right]e^{-i(\beta z+\omega t)} + c.c. \tag{3.60}$$

Comparing this to the electric field ansatz (2.42), the modes are related by

$$U(t,z) = u(t,z) + \frac{i}{\omega}\partial_t u(t,z) \tag{3.61}$$

$$V(t,z) = v(t,z) + \frac{i}{\omega}\partial_t v(t,z). \tag{3.62}$$

In section 2.2.1, the modes U and V were taken to be in a steady state and therefore independent of time. In this case, the time derivatives of the $u(t,z)$ and $v(t,z)$ are zero and there is an equivalence between the two sets of mode $U(z) = u(z)$ and $V(z) = v(z)$. In the time dependent case, the time derivatives are proportional to $1/\omega$. As ω is typically very large, the time derivative terms will be small for a slowly varying envelope and so the two sets of modes are approximately equivalent $U(t,z) \approx u(t,z)$ and $V(t,z) \approx v(t,z)$. The electric field can then be written as

$$E_x \approx u(t,z)e^{i(\beta z-\omega t)} + v(t,z)^{-i(\beta z+\omega t)} + c.c, \tag{3.63}$$

so that the vector potential ansatz (3.59) and the electric field ansatz (2.42) give effectively equivalent descriptions. The magnetic field can be found by taking the spatial derivative of the vector potential, which gives

$$B_y = \Big[\frac{\beta}{\omega}v(t,z) + \frac{i}{\omega}\partial_z u(t,z)\Big]e^{i(\beta z-\omega t)} - \Big[\frac{\beta}{\omega}v(t,z) + \frac{i}{\omega}\partial_z v(t,z)\Big]e^{-i(\beta z+\omega t)} + c.c. \quad (3.64)$$

By the same analysis as applied to the electric field, the magnetic field can be approximated by

$$B_y \approx \frac{1}{v_p}u(t,z)e^{i(\beta z-\omega t)} - \frac{1}{v_p}v(t,z)e^{-i(\beta z+\omega t)} + c.c. \quad (3.65)$$

where v_p is the phase velocity of the mode given by ω/β.

3.3.2 Coupled mode equations for linear superstructure gratings

Chapter 4 is based on superstructure gratings with time dependent forward and backward propagating modes. In this section the corresponding coupled mode equations are derived using a Lagrangian approach. The Lagrangian for a linear isotropic medium with an x-polarised vector potential propagating in the z-direction is given by

$$\mathcal{L} = \frac{\epsilon_0}{2}n^2(\partial_t A_x)^2 + \frac{1}{2\mu_0}(\partial_z A_x)^2. \quad (3.66)$$

Coupled mode equations can be developed from the Lagrangian by substituting the vector potential ansatz (3.59) for linear forward and backward propagating modes and the superstructure grating profile (2.87). The subsequent expression is fairly long and complex, however, applying rotating wave and slowly varying envelope approximations the important dynamics can be extracted and the Lagrangian reduces to

$$\begin{aligned}\mathcal{L}_{lin} = &\frac{i\epsilon_0\bar{n}^2}{\omega}\big(u^*\partial_t u - u\partial_t u^* + v^*\partial_t v - v\partial_t v^*\big)\\ &+ \frac{i\epsilon_0\bar{c}^2\beta}{\omega^2}\big(u^*\partial_z u - u\partial_z u^* + v^*\partial_z v - v\partial_z v^*\big)\\ &+ \epsilon_0\bar{n}\delta n\big(v^*u\,e^{2i\Delta z} + u^*v\,e^{-2i\Delta z}\big).\end{aligned} \quad (3.67)$$

The explicit time and spatial dependence of the modes has been dropped for simplicity. To find the coupled mode equations for u and v, the Lagrangian has to be varied with respect to modes u^* and v^*. Similarly, the coupled mode equations for u^* and v^* are found by varying the Lagrangian with respect to u and v. However, as these are simply complex conjugates of each other the dynamics of the modes are fully determined by

one set of the coupled mode equations. First applying the Euler-Lagrange equation to the mode u gives

$$\frac{\partial \mathcal{L}}{\partial u^*} = \frac{i\epsilon_0 \bar{n}^2}{\omega}\partial_t u + \frac{i\epsilon_0 c^2 \beta}{\omega^2}\partial_z u + \epsilon_0 \bar{n}\delta n\, v\, e^{-2i\Delta z} \tag{3.68}$$

$$\partial_t\left(\frac{\partial \mathcal{L}}{\partial(\partial_t u^*)}\right) \approx -\frac{i\epsilon_0 \bar{n}^2}{\omega}\partial_t u \tag{3.69}$$

$$\partial_z\left(\frac{\partial \mathcal{L}}{\partial(\partial_z u^*)}\right) = -\frac{i\epsilon_0 c^2 \beta}{\omega^2}\partial_z u \tag{3.70}$$

where terms proportional to $\delta n/\omega$ have been neglected as a small. Then combining the equations (3.68-3.70) gives the coupled mode equation

$$\frac{1}{v_p}\partial_t u + \partial_z u = i\kappa f(z)a(z)ve^{-2i\Delta z}. \tag{3.71}$$

Varying the action with respect to v^* and applying the same approximation yields the second coupled mode equation

$$\frac{1}{v_p}\partial_t v - \partial_z v = i\kappa f(z)a(z)ue^{2i\Delta z}. \tag{3.72}$$

where in both equations the coupling is given by

$$\kappa = \frac{\delta n \beta}{2\bar{n}}. \tag{3.73}$$

In the steady state case where $\partial_t u = 0$ and $\partial_t v = 0$, these equations are equivalent to the coupled mode equations in section 2.2.3.

3.3.3 Energy and group velocity

Using the expression for the electric and magnetic fields (3.63) and (3.65) it is possible to calculate the group velocity. It is a general result that in a lossless medium the group velocity is equal to the energy velocity $v_g = v_E$ [52]; where the energy velocity is equal to ratio of the Poynting vector and the Hamiltonian [53]

$$v_{E,i} = \frac{S_i}{\mathcal{H}}. \tag{3.74}$$

For a linear non-magnetic medium this leads to

$$v_{E,i} = \frac{2c\epsilon_{ijk}E_jB_k}{(\delta_{lm} + \chi^{(1)}_{lm})E_lE_m + cB_lB_l}. \tag{3.75}$$

Using this expression, the energy velocity for a superstructure grating can be calculated. First the electric susceptibility is set to $\chi^{(1)}_{ij} = n^2(z)\delta_{ij}$, where $n(z)$ is given by equation (2.87). Then taking the expressions for the electric and magnetic fields given by equations (3.63) and (3.65) respectively, and substituting them into the energy velocity (3.75) yields

$$v_g(t,z) = v_p\frac{|u|^2 - |v|^2}{|u|^2 + |v|^2} \tag{3.76}$$

after making slowly varying envelope and neglecting small term approximations. With this expression the group velocity is both dependent on position and time. It is useful to consider an effective group velocity over the the entire length of a device which can be calculated by taking the spatially averaged Hamiltonian and Poynting vector

$$v_g = \frac{\langle S\rangle}{\langle \mathcal{H}\rangle}. \tag{3.77}$$

Then the group velocity is given by

$$v_g(t) = v_p\frac{\int_0^L dz\ |u|^2 - |v|^2}{\int_0^L dz\ |u|^2 + |v|^2}. \tag{3.78}$$

In the case where the modes are taken to be in a steady state, equation (3.78) is equivalent to the expression for the group velocity found by Janner et al [36]. However, they arrived at the expression using the Hellman-Feynman theorem of quantum mechanics, whereas using the energy velocity allows for the expression to be arrived at classically.

3.4 Summary

This chapter has introduced an alternative approach to developing coupled mode equations for optical devices by using the Lagrangian method rather than Maxwell's equations. A brief overview of the techniques and methods used in the Lagrangian formalism have been given along with how they can be applied to coupled mode theory. While both the Lagrangian formalism and Maxwell's equations give physically equivalent descriptions, the Lagrangian formalism provides a systematic way of generating

coupled mode equations. This was demonstrated by deriving the couple mode equations for a time-dependent superstructure grating. The methods introduced in this chapter will be used throughout the rest of this work to develop the necessary coupled mode equations.

Chapter 4

Dynamic moiré gratings

This chapter is based on the journal publication [54] and looks at the effect of dynamically varying the grating strength or AC component of a grating and its applications for optical storage. It was established in section 2.2.1 that the rejection bandwidth of a Bragg grating is dependent on the size of the grating strength. This relationship is given by equation (2.68). Making the grating strength larger increases the size of the band gap and conversely making it smaller reduces the size the band gap. Therefore, by dynamically varying the grating strength it is possible to create variable transmission bands by increasing and decreasing the rejection bands. Bragg gratings with dynamic grating strengths of this type have been looked in the context of Brillouin scattering [55].

In this chapter we focus not on varying the grating strength of Bragg gratings but of a moiré gratings. Moiré gratings were introduced in section 2.2.3 and their properties will be discussed in more detail in this chapter. The moiré grating is created by taking a Bragg grating and applying a spatially periodic modulation to the grating strength. The effect this has is to open a transmission band in the centre of the rejection band. The reflectance of the grating can then be thought of as two rejection bands separated by a transmission band. Increasing the grating strength of a moiré grating has the same effect as a Bragg grating except both rejection bands increase in size, which in turn reduces the size of the transmission band.

With this in mind, a device analogous to EIT can be created for optical storage. An EIT device works by taking a gas which in its unperturbed state is opaque. A strong laser in then used to induce a transparency window allowing a pulse to propagate through the gas. By switching the laser off, the transparency window closes and the pulse becomes trapped inside. Switching the laser back on reopens the transmission window and the pulse can escape. It was demonstated by Hau et al. [18, 20, 21] that EIT could be used to bring a pulse to an almost complete stand-still. A dynamic moiré grating can

create a similar storage device by effectively behaving in the opposite way to EIT. Initially the grating has a transmission with a large enough bandwidth to a accommodate a probe pulse. Then by dynamically increasing the grating strength, the transmission band closes, thereby trapping the pulse. By decreasing the grating strength, the transmission returns to its original bandwidth allowing the pulse to be released. Such a device has the potential to realise the longstanding goal of replicating the astonishing results observed in EIT using a solid-state photonic crystal device [5].

Using an EIT device, when the pump laser is switched off, the transmission band is completely closed, trapping the pulse. With the moiré grating, increasing the grating strength cannot completely close the transmission band, only narrow it. A property of moiré gratings is that the group velocity in the transmission band decreases with the width of the transmission band[8, 35]. So as the grating strength is increased, the group velocity decreases. If the group velocity is decreased sufficiently then the pulse becomes trapped. Of course, trapping the pulse is time limited. The pulse is still moving through the grating albeit at a reduced group velocity, and will eventually emerge out. If, however, the required storage time is less than time taken for the pulse to propagate the length of the grating, then the device can be used as an effective optical storage device. Moreover, over the time scale that the pulse is trapped within the device, the pulse can be released on demand by decreasing the grating strength. This is a long sought after goal in optical storage devices, and a problem with optical delay lines where release times are limited to integer multiples of the time taken for the pulse to propagate the length of the device. In the moiré grating, the release time is limited to the time taken to switch the grating strength.

Another benefit of this device is that it is able to overcome the delay-bandwidth product limit. Typically, any slow light device will induce a delay Δt due to the decreased group velocity over the bandwidth of the slow light resonance Δf. The product $\Delta t \Delta f$ is approximately constant for any given slow light device when varying the size of the resonance. The delay-bandwidth product limits the performance of any slow device and there are a number of papers which discuss the limitation of various devices [12, 13, 14]. The dynamic moiré grating is not bound by the delay-bandwidth product as the product does not remain constant as the size of the transmission band is dynamically varied. The slow light resonance bandwidth is equal to the bandwidth of the transmission band before the grating strength is varied. However, the induced group delay is dependent on the change in the grating strength. Increasing the grating strength increases the group delay and therefore the delay-bandwidth product can be made arbitrary large by squeezing the pulse spectrum; allowing the dynamic moiré grating to break the constraint.

The idea of enhancing the delay-bandwidth product by using a time-varying structure has been looked at before [56]. All such structures work by same the principle, dynamically varying the bandwidth of the resonance. A device with an initially larger

bandwidth and group velocity is dynamically altered such that the device has a smaller bandwidth and group velocity. The delay-bandwidth product is then given by the product of the initially larger bandwidth and the increased delay due to the lower group velocity after the time variation. This leads to an overall enhancement of the delay-bandwidth product. This behaviour has been demonstrated theoretically using a slow light device with coupled resonators [57, 58] replicating the results of EIT [59]. There have been more general theoretical studies of such devices [60, 61] and studies applied to specific devices such as a quasi-phase-matched waveguide using backward frequency conversion [62], a p-i-n integrated photonic crystal nanocavity [63], a waveguide with moving index fronts [64] and in a grating coupled metal-dielectric-metal waveguide [65].

This chapter is split into four main sections. The first section explores moiré gratings in more depth than was presented in chapter 2 and highlights the important features for optical storage. The second section looks abstractly at dynamic moiré gratings and presents simulations for storing optical pulses. The third section looks at another application of dynamic moiré gratings, pulse bandwidth modulation. Optical storage relies on symmetrically switching the grating strength to trap and release the pulse. By asymmetrical switching the grating strength the pulse bandwidth can be stretched and compressed. The final section looks a possible realisation of dynamic moiré gratings by using an electro-optic grating.

4.1 Properties of moiré gratings

The moiré grating is a superstructure grating that was introduced in chapter 2. It is created by superimposing two Bragg gratings which is what gives the grating its name. As discussed in section 2.2.3 it has the interesting feature that it creates a slow light transmission band between two rejection bands. The dual band gap structure offers an additional benefit. The band edges either side of the transmission band produce opposite normal and anomalous dispersion. This results in cancellation of second order dispersion at the centre of the transmission band and reduces pulse broadening. This is in contrast to the slow light band edges of a Bragg grating where dispersion causes pulse broadening.

The superimposed Bragg gratings that make up a moiré grating can be reformulated into a single Bragg grating multiplied by a superstructure envelope given by equation (2.87). The superstructure envelope is periodic with period Λ_S which is in general called the superstructure period, but when discussing moiré grating is termed the moiré period.

4.1.1 Relationship between moiré and π phase shifted gratings

The moiré grating is very closely related to another superstructure grating, the π phase shifted grating. To see this, note that as the moiré envelope oscillates it is changing sign which creates π phase shifts in the Bragg envelope. Therefore the moiré grating can be rewritten in the form

$$n(z) = \bar{n} + \delta n(z)|\cos(K_S z)| \cos\Big(K_B z + \pi\theta\big(-\cos(K_S z)\big)\Big), \tag{4.1}$$

where the superstructure wavenumber is given by

$$K_S = \frac{2\pi z}{\Lambda_S}. \tag{4.2}$$

Expressed this way, it is the modulus of the moiré envelope that multiplies the Bragg envelope and therefore remains non-negative. This effectively applies a cosine apodisation over the length of each half moiré period. The sign changes are implemented directly into the phase of the Bragg envelope with the Heaviside θ function which is defined by

$$\theta(x) = \begin{cases} 0 & x \leq 0 \\ 1 & x > 0. \end{cases} \tag{4.3}$$

This means that when the moiré envelope $\cos(K_S z)$ is negative, the Heaviside function evaluates to one, and a π phase shift is inserted into the Bragg phase. When the moiré envelope is positive the Heaviside function evaluates to zero and the π phase shift is removed. Therefore, equation (4.1) makes the essential features of the moiré envelope clear, it inserts π phase shifts into the Bragg envelope and applies a cosine apodiation over the length of each half moiré period.

A π phase-shift grating is a commonly used grating where a single π phase shift is added into the Bragg envelope at the centre of the grating. A well-known feature of this grating is that it opens a small transmission band at the centre of the Bragg resonance [66]. By setting $\Lambda_S = L$ and neglecting the local apodisation term $|\cos(K_S z)|$, the profile for the π phase-shift grating can be written as

$$n(z) = \bar{n} + \delta n(z) \cos\Big(K_B z + \pi\theta\big(-\cos(K_S z)\big)\Big). \tag{4.4}$$

By making Λ_S smaller multiple phase shifts can be introduced. This has the effect of broadening the transmission band. Equation (4.4) then also defines the π phase-shifted

grating which contrasts with the π phase-shift grating by having multiple phase shifts instead of a single phase shift. Although equations (4.4) makes clear the insertion of π phase shifts, it is more convenient to express the grating in the equivalent form

$$n(z) = \bar{n} + \delta n(z)\ \mathrm{sgn}\big(\cos(K_S z + \phi_S)\big)\cos(K_B z), \tag{4.5}$$

where sgn is the sign function defined by

$$\mathrm{sgn}(x) = \begin{cases} -1 & x \leq 0 \\ 1 & x > 0. \end{cases} \tag{4.6}$$

Equation (4.5) makes clear the connection between the moiré grating and the π phase shifted grating, where the latter can be generated by the former by replacing the moiré with a square wave of the same periodicity.

4.1.2 Analytical solutions

The steady-state coupled mode equations for the moiré grating given by equations (3.71) and (3.72) have in general no analytical solutions and have to be solved numerically. However, they do permit an analytical solution when no apodisation is applied and when the wavelength is taken to be the Bragg wavelength. In this case the detuning given by equation (2.53) is zero and therefore the oscillating terms $e^{2i\Delta z}$ and $e^{-2i\Delta z}$ evaluate to one. In this case the equations have the general solutions

$$u(z) = c_1 \cosh\big(F(z)\big) + ic_2 \sinh\big(F(z)\big) \tag{4.7}$$

$$v(z) = c_2 \cosh\big(F(z)\big) - ic_1 \sinh\big(F(z)\big), \tag{4.8}$$

with arbitrary constants c_1 and c_2. The hyperbolic phase term is given by

$$F(z) = \kappa \int_0^z dz' \cos(K_S z' + \phi_S) f(z'), \tag{4.9}$$

where $f(z)$ is an apodisation function and ϕ_S is an arbitrary initial phase. The particular solution for a realistic grating is given by imposing the boundary conditions $u(0) = A$ and $v(L) = 0$. This ensures that the backwards mode is zero at the end of the grating and gives the input forward mode an initial amplitude A. The boundary conditions impose the following constraints on the constants

$$c_1 = A \tag{4.10}$$

$$c_2 = ic_1 \tanh\left(F(z)\right) \tag{4.11}$$

and results in the following expression for the reflectance

$$R = \left|\frac{c_2}{c_1}\right|^2 = \tanh^2\left(F(L)\right). \tag{4.12}$$

If we compare equation (4.12) with the reflectance for a Bragg grating given by equation (2.83), a Bragg grating has $F(L) = \kappa L$. As the length of a Bragg grating is increased, so is its reflectance. For a moire grating, the oscillating moiré envelope in equation (4.9) causes the reflectance to oscillated with the length of the grating. Figure 4.1a shows a plot of $F(L)$ against the moiré period. The gratings all have length of $L = 10$ cm, a grating strength of $\delta n = 10^{-3}$ and Bragg wavelength of $\Lambda_B = 1550$ nm. A Gaussian apodisation of the form given by equation (2.85) has been used. The figure shows how the oscillations in $F(L)$ vary by the Gaussian apodisation parameter α_A, where $\alpha_A = 0$ corresponds to no apodisation and $\alpha_A = 16$ is the strongest apodisation in the figure. The apodisation has the effect of suppressing $F(L)$, with a stronger apodisation causing greater suppression. The corresponding reflectance is shown in figure 4.1b. With no apodisation applied, the grating oscillates between strong reflectance and transmission. Increasing the apodisation suppresses the high reflectance regions so that good transmission can be achieved for all moiré periods.

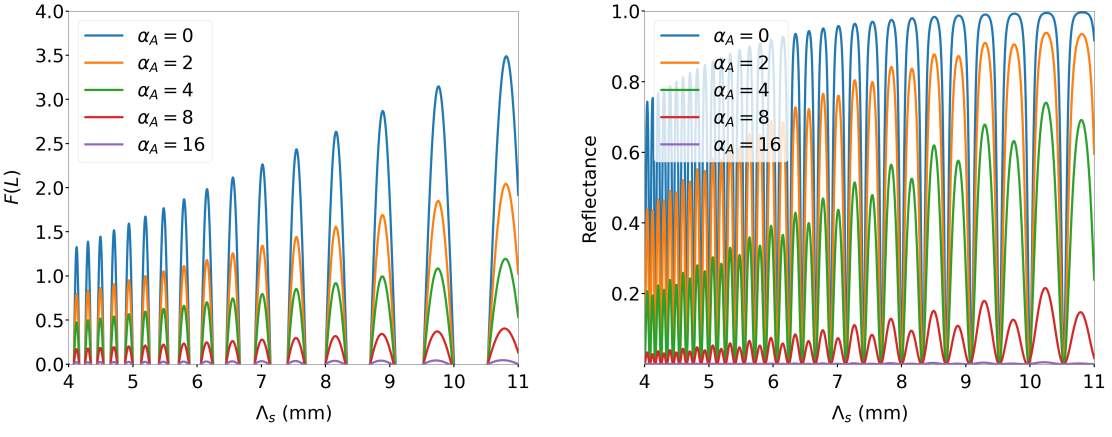

(a) (b)

FIGURE 4.1: (a) shows the hyperbolic phase terms (4.9) for analytical solutions of the moiré grating when varying the strength of a Gaussian apodisation and moiré period. 4.1b shows the corresponding reflectance

With no apodisation applied and $\phi_S = 0$, the hyperbolic phase term has the solution

$$F(L) = \frac{\kappa}{K_S} \sin(K_S L). \tag{4.13}$$

The moiré periods giving maximum transmission correspond to minimising $F(L)$ and are given by

$$\Lambda_S = \frac{2L}{m}, \tag{4.14}$$

where m is a positive integer. Conversely the moiré periods corresponding to maximum reflectance correspond to maximising $F(L)$, which gives

$$\Lambda_S = \frac{2L}{2m+1}. \tag{4.15}$$

Figure 4.2 shows the group velocity calculated using equation 3.78 for the associated modes for the gratings given in figures 4.1a and 4.1b. As with the reflectance, when no apodisation is applied the group velocity oscillates between maximum and minimum values. In contrast to the reflectance, the maximum group velocity values occurs when the moiré period minimises $F(L)$, and the minimum group velocity occurs when the moiré period maximises $F(L)$. Therefore, moiré periods that give higher reflectance also produce lower group velocity. The effect of increasing the apodisation is to again smooth out the group velocity so that it approaches a monotonically decreasing function with respect to the moiré period.

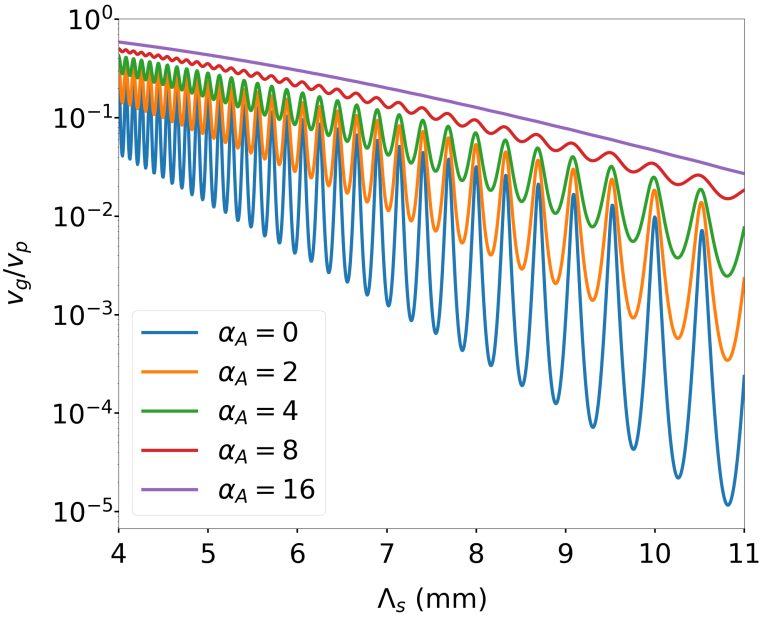

FIGURE 4.2: Figure showing the group velocity of a moiré grating by moiré period for varying Gaussian apodisation strengths

4.1.3 The transmission band

The feature of the moiré grating which is of principal interest is the transmission band. Unfortunately, just like the coupled mode equations, there is no analytical solution for the band edges of the transmission band. In the case where the moiré period is small, so that there are a large number of π phase shifts, then moiré grating is well approximated by two distinct Bragg gratings. The band edges for a Bragg resonance were derived in section 2.2.1. If we take one Bragg grating with a Bragg period Λ_1 and second Bragg grating with Bragg period Λ_2, then the wavelength corresponding to the upper band edge of the first grating is $\Lambda_2(\bar{n} + \delta n/2)$, and the wavelength corresponding to the lower band edge of the second grating is $\Lambda_2(\bar{n} - \delta n/2)$. Using these wavelengths and relationship between the Bragg periods and moiré period given by equations (2.91) and (2.90), the transmission bandwidth is given by

$$\Delta f = \frac{c}{\bar{n}}\left(\frac{1}{\Lambda_S} - \frac{\delta n}{\lambda_B}\right). \tag{4.16}$$

From this expression the two parameters that chiefly determine the size of the transmission band are the moiré period and the grating strength. If the size of either of these quantities is increased, the size of the transmission band is reduced. Conversely, decreasing the size of the quantities increases the size of the transmission band. As the group velocity within the transmission band is dependent on the size of the transmission bandwidth, lower group velocities correspond to larger values of the moiré period and the grating strength.

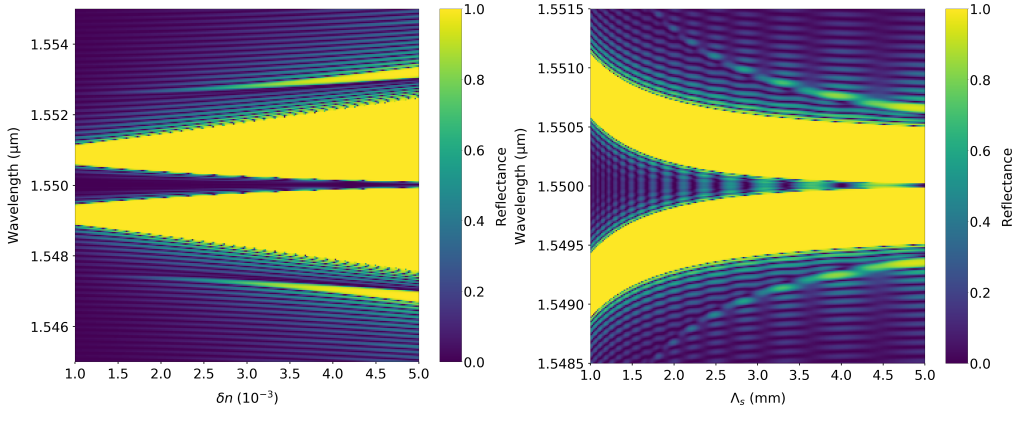

FIGURE 4.3: (a) Reflectance for a moiré grating when varying δn with $\Lambda_S = 1\,\text{mm}$ and $L = 10\,\text{mm}$ and (b) Reflectance for a moiré grating when varying Λ_S with $\delta n = 10^{-3}$ and $L = 5\,\text{mm}$.

Figure 4.3(a) shows a plot of the reflectance of a moiré grating by grating strength. As the grating strength is increased, the band gaps broaden which reduces the size of the available transmission band. Figure 4.3(b) shows a plot of the reflectance as the moiré

period is increased. In this case, the band gaps maintain their size but move closer together which decreases the transmission band. The point where the approximation (4.16) begins to break down can be determined by considering the bandwidth for a Bragg band gap which is given by

$$\Delta f_B = v_p \delta n / \lambda_B. \tag{4.17}$$

Taking the expression for the transmission band given by equation (4.16) and setting it equal to the Bragg band gap bandwidth given by equation (4.17) gives the moiré period

$$\Lambda_S = 2\lambda_B / 3\delta n. \tag{4.18}$$

For moiré periods less than this value, equation (4.16) gives a good approximation to the moiré transmission band. For larger moiré period equation 4.16 starts to breakdown and an alternative numerical approach needs to be used. One way of doing this is to use the position-averaged energy density which is given by

$$\langle U \rangle = \frac{2\epsilon_0 \bar{n}^2}{L} \int_0^L dz \; |u|^2 + |v|^2. \tag{4.19}$$

As the wavelength approaches the band edge of the transmission band, the group velocity tends to zero which can be seen in figure 2.5a in section 2.2.3. At these wavelengths, there is strong coupling between the medium and modes which causes an increase in the energy density. The transmission band edges can then be numerically detected by finding the maxima in $\langle U \rangle$. Figure 4.4(a) shows a plot of the $\langle U \rangle$ for a moiré grating with the vertical lines indicating the maxima. Figure 4.4(b) shows the corresponding reflectance spectrum where the vertical lines are again maxima in $\langle U \rangle$ and clearly show that they correspond to the band edges of the transmission band.

Figure 4.5(a) shows a comparison of the two methods of calculating the transmission bandwidth. The blue line shows the transmission band calculated from equation (4.16) using Bragg theory and the dotted red line shows the transmission band calculated by numerically detecting the band edges using U. The vertical line corresponds to the moiré period given by equation (4.18), where the Bragg theory approach to calculating the transmission band starts to fail. From the figure the two approaches agree well before this moiré period and start to diverge afterwards. Figure 4.5(b) shows the corresponding group velocity. For moiré periods after the vertical line, the group velocity begins to decrease more rapidly and the transmission band becomes a slow light resonance.

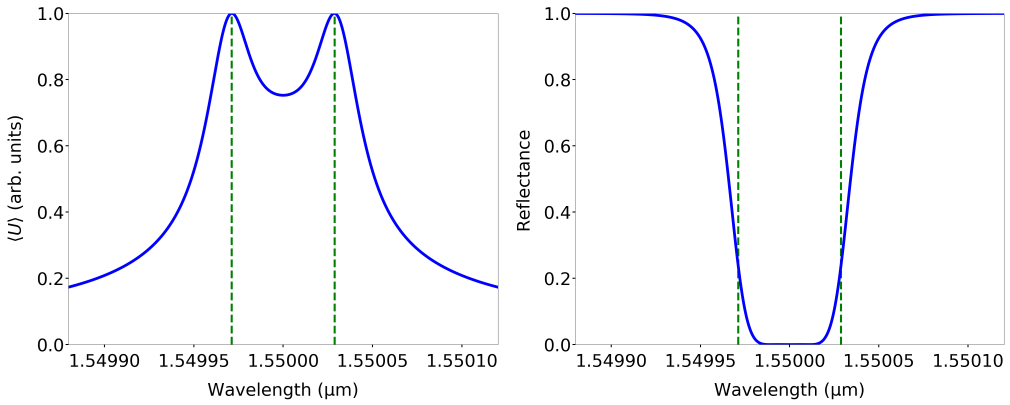

(a) (b)

FIGURE 4.4: (a) the position-averaged energy density and (b) the transmission band of a moiré grating. The maxima of the the position-averaged energy density is indicated with vertical lines which correspond to the band edges of the transmission band.

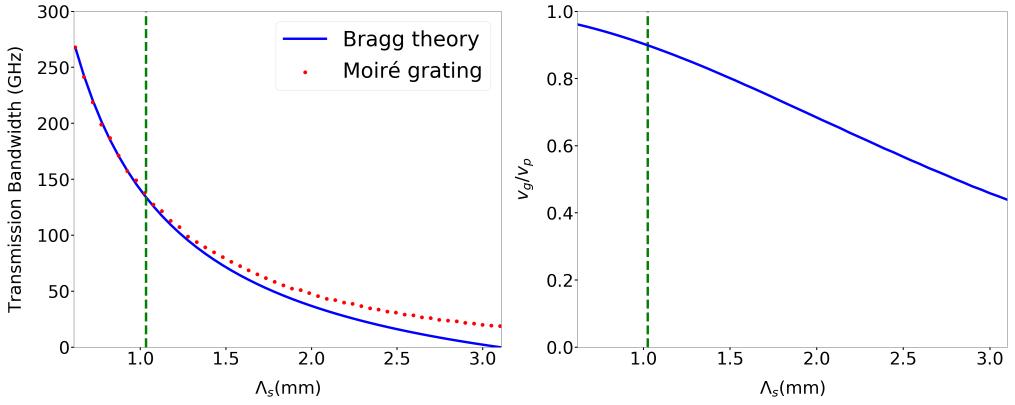

(a) (b)

FIGURE 4.5: (a) Moiré transmission bandwidth calculated from Bragg theory and a numerical calculation, and (b) group velocity of a moireé grating versus moireé period Λ_S. The grating has a Gaussian apodization with parameters $L = 20$ cm, $\lambda_B = 1.55\mu$m, $\bar{n} = 1.445$, $\delta n = 10^{-3}$. The vertical green line indicates the moireé period beyond which the approximation of the moireé grating by two Bragg gratings begins to break down.

4.2 Dynamic moiré gratings and optical storage

4.2.1 Coupled mode equations with dynamic coupling

In this section we look at dynamically varying the grating strength of a moiré grating and the effect that this has on a pulse propagating through the grating. Increasing the grating strength decreases the size of the transmission band which was demonstrated in figure 4.3(a). As the group velocity within the transmission band is dependent on the size of the transmission band, increasing the grating strength decreases the group velocity. If the bandwidth of the pulse falls spectrally within the transmission band,

then it is natural to suppose that as the grating strength is increased, the pulse will slow due to the reduction in the group velocity. And if the grating strength is increased sufficiently, then it should be possible to bring the pulse to a practical stand still.

To model the behaviour, the grating strength needs to become time dependent $\delta n(t)$. This is analogous to a spatial apodisation. A spatial apodisation varies the grating strength in space, the purpose of which is suppress the grating sidelobing. Throughout this work an arbitrary grating function has been denoted by $f(z)$. To avoid confusion the temporal variation of the grating strength shall be denoted by the function $g(t)$ and referred to as the windowing function. Just as with the apodisation it varies between zero and one. The set of coupled mode equations which describe the behaviour were derived in section 3.3.2 and given by equations (3.71) and (3.72). In this case the grating strength was constant in time. Fortunately, including the time dependence is fairly straight forward. It is a simple case of replacing the grating strength with its time dependent version so that the coupled mode equations become

$$\frac{1}{\bar{v}_p}\frac{\partial u}{\partial t} + \frac{\partial u}{\partial z} = i\kappa(t,z)ve^{-2i\Delta_B z} \tag{4.20}$$

$$\frac{1}{\bar{v}_p}\frac{\partial v}{\partial t} - \frac{\partial v}{\partial z} = i\kappa(t,z)ue^{2i\Delta_B z} \tag{4.21}$$

and then the coupling constant is given by

$$\kappa(t,z) = \frac{\delta n(t,z)a(z)\beta}{2\bar{n}} \tag{4.22}$$

As the coupling constant is proportional to the grating strength, talking of a time varying grating strength is equivalent to talking of a time varying coupling strength and both will be referred to either depending on the context.

The justification for equations (4.20) and (4.21) can be seen by looking by looking at the Lagrangian given by equation (3.67) and taking only the terms which contain the grating strength which are

$$\mathcal{L}_{\delta n} = \epsilon_0 \bar{n}\delta n\left(v^* u\, e^{2i\Delta z} + u^* v\, e^{-2i\Delta z}\right). \tag{4.23}$$

The terms proportional to the grating strength do not contain time derivatives of the u and v modes. This means that when the Euler-Lagrange equation (3.18) is applied to give the equations of motion for the modes, there will be no time derivatives of the grating strength. Therefore, the coupling strength is simply proportional to the time-dependent grating strength and not its derivatives.

4.2.2 Grating strength and temporal windowing

Some choice needs to be made about how to define the time dependent grating strength. Ideally it should generalise an apodised grating such that in a limiting case it is equivalent to a time independent grating. An appropriate choice is then

$$\delta n(t,z) = \delta n f(z)\big(1 + \mu g(t)\big) \tag{4.24}$$

The parameter for the windowing strength μ has been introduced to set the magnitude of the variation of the grating strength. It is constrained such that $\mu \geq 0$. The limiting case comes when $\mu = 0$, then the grating strength reduces to a time independent grating. As the windowing function varies between zero and one, the grating will have double its originally value when $\mu = 1$, triple its value at $\mu = 2$ and so on.

We are principally interested in the change in group velocity as ultimately the purpose of the device is storing an optical pulse. To this end, figure 4.6a and 4.6b show the group velocity change by varying the strength μ for a given moiré period Λ_S for a moiré grating and a π phase shifted grating respectively.

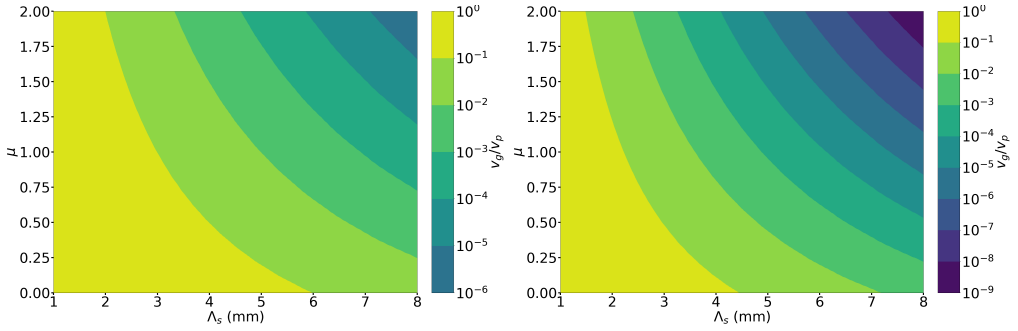

(a) (b)

FIGURE 4.6: Group velocity of (a) a moiré grating and (b) a π phase-shifted grating versus Λ_S and μ. The grating has a raised cosine apodization with 70% flat top with parameters $L = 20$cm, $\lambda_B = 1.55\mu$m, $\bar{n} = 1.445$, $\delta n = 10^{-3}$.

The figures are generated by solving the steady state version of equations (4.20) and (4.20) at the Bragg wavelength which is taken to be 1550 nm. The gratings are 20 cm long and have an initial grating strength of $\delta n = 10^{-3}$. The windowing function is set to one and the windowing strength μ is increased from zero to two, which as discussed corresponds to tripling the initial grating strength. The effect this has on the group velocity is stark. For a small moiré period where the transmission band is large, the increase in μ has little influence. As the length of the moiré period is increased, meaning a smaller initial transmission band, the squeezing of the transmission band by increasing μ has a greater effect on the group velocity reduction. For a moiré grating in figure 4.6(a) with period 4 mm, the decrease in group velocity is roughly two orders magnitude. For a π phase shifted grating with the same period, the group velocity reduction

is even greater, roughly three orders of magnitude as can be seen in figure 4.6(b). This can be contributed to the overall higher average grating strength of a π phase shifted grating that comes from neglecting the local sine apodisation of the moiré grating.

It was discussed in the introduction to this chapter that dynamically changing the size of the transmission band alters the delay-bandwidth product $\Delta f \Delta t$, which is a general figure of merit for slow light device. The delay time for the dynamic grating in its initial state is given $\Delta t = L/v_g$ and its delay time with the full windowing strength applied is $\Delta t^{'} = L/v_g^{'}$ where v_g is the initial group velocity and $v_g^{'}$ is altered group velocity. In both cases the acceptance bandwidth is Δf. Therefore, the enhancement in the delay-bandwidth product is given $\Delta t^{'}/\Delta t$, which is equal to $v_g/v_g^{'}$.

Figures 4.6(a) and 4.6(b) show that the group velocity can be decreased by many orders of magnitude, which correspondingly means the delay-bandwidth product can be enhanced by many orders of magnitude. Ultimately the change in the group velocity is dependent on the change in the grating strength with is proportional to $\mu\delta n$. Therefore, maximising the delay-bandwidth product corresponds to maximising $\mu\delta n$.

4.2.3 Coupled mode pulse simulation

To perform a simulation of a pulse propagating through a moiré grating with a time dependent grating strength, we first take the expression for the grating strength given by (4.24) and substitute it into the coupled mode equations (4.20) and (4.21). Figures 4.7(a) and 4.7(b) show the corresponding simulations for a pulse with a bandwidth of 320MHz at FWHM.

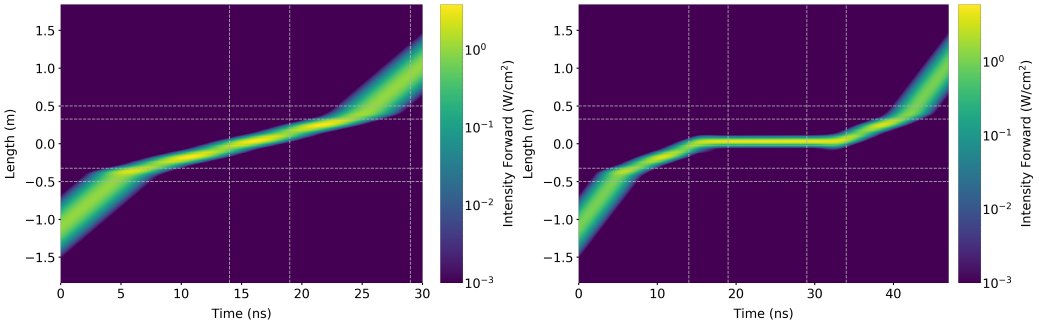

FIGURE 4.7: Intensity distribution in space and time of a pulse propagating through (a) a static moiré grating and (b) a dynamic moiré grating with $\mu = 2$. The grating has a raised cosine apodization with 65% flat top with parameters $L = 1\,\text{m}$, $\Lambda_S = 4\text{mm}$, $\lambda_B = 1.55\mu\text{m}$, $\bar{n} = 1.445$, $\delta n = 10^{-3}$. The pulse has FWHM spectral bandwidth of 320MHz with carrier wavelength λ_B.

In both simulations the grating is 1 meter long with a raised cosine apodisation which has a 70% flat top. The horizontal lines show the start and end of the grating and indicate the flat top region where the apodisation has a constant value of 1. Figure 4.7(a) shows the pulse entering and propagating through the grating without varying the grating strength so that $\mu = 0$ for the duration of the simulation. Figure 4.7(b) shows the same simulation but with grating strength modulated in time. The windowing function at time $t = 14$ ns is smoothly increases over a period of 5 ns from 0 to 1 with a windowing strength of $\mu = 2$. The effect is to reduce the group velocity by a further two orders of magnitude. At time $t = 24$ ns, the windowing smoothly decreases over a period of 5 ns from 1 to 0, restoring the pulse to its original group velocity. The vertical lines in the figure show where the windowing function increases and decreases, and where it is held constant at a maximum value of 1. Comparing the two figures, it is clear that when the change in grating strength is applied, the pulse is slowed appreciable compared to when grating strength is static. This demonstrates that dynamically varying the coupling strength with a pulse localised within the grating can dramatically decrease the group velocity of the pulse.

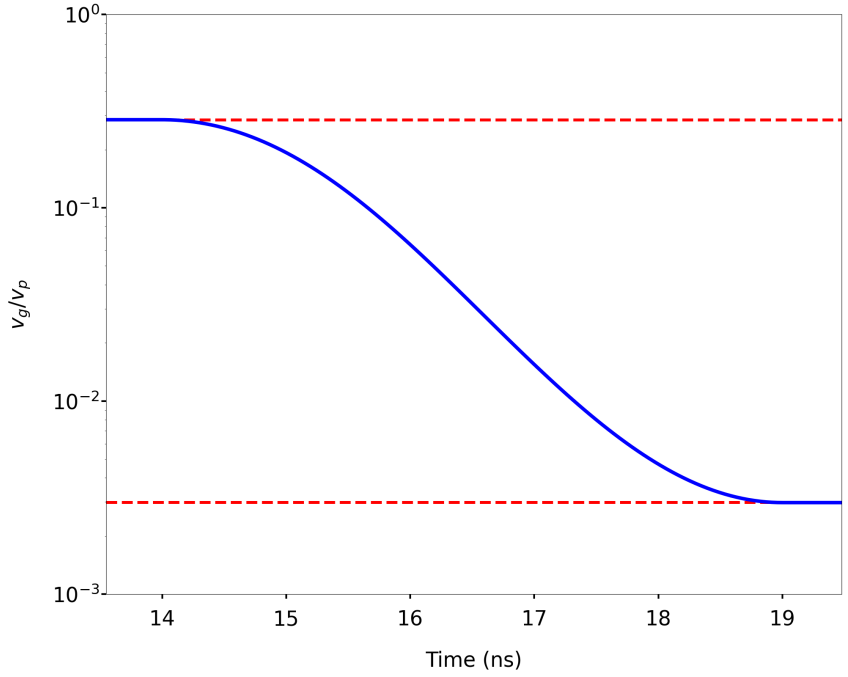

FIGURE 4.8: Plot showing the pulse group velocity in a dynamic grating as the windowing strength is μ is increased from zero to one. The horizontal lines show the corresponding steady state calculations for the group velocity when μ equals zero and one

In the previous section the change in group velocity was calculated using steady-state gratings. Figure 4.8 shows the change in group velocity calculated using equations (3.78) for the pulse simulated in figure 4.7(b). The horizontal lines shows the steady-state group velocity calculations for the grating when $\mu = 0$ and $\mu = 2$. As can be seen

in the figure, the group velocity of the pulse smoothly varies between the steady-state values. Therefore, the steady-state calculations do provide a good approximation for the full dynamical system. The steady-state analysis from the previous section showed that the enhancement in the delay-bandwidth product is determined by the change in the group velocity $v_g/v_g^{'}$. The simulated group velocity change in figure 4.7(b) is two orders of magnitude. As figure 4.8 demonstrates the steady-state analysis is valid, it follows that the delay-bandwidth product in figure 4.7(b) has been enhanced by two orders of magnitude.

4.2.4 Coupled mode pulse simulation importance of apodisation

In this section we look at the effect of the apodisation profile. In the previous section, the simulations were carried out with a raised cosine apodisation profile. The reason for this is that the raised cosine has a flat top region where the apodisation is held constant. This means that when the grating strength is modulated in time, the entire pulse experiences the same change in grating strength and therefore change in group velocity. If we consider figures 4.6a and 4.6b, the change in the group velocity is dependent not only on the change of the grating strength but also its initial value. For a raised cosine apodisation profile, the group velocity change will be uniform along its flat top region as the initial grating strength is constant. In contrast to this, the grating strength with a Gaussian apodisation is constantly varying along the length of the grating. Consequently, the group velocity is also varying along the length of the grating. Therefore, in such a grating, when the grating strength is dynamically varied, the change in group velocity varies along the length of the pulse. Figure 4.9 demonstrates this behaviour.

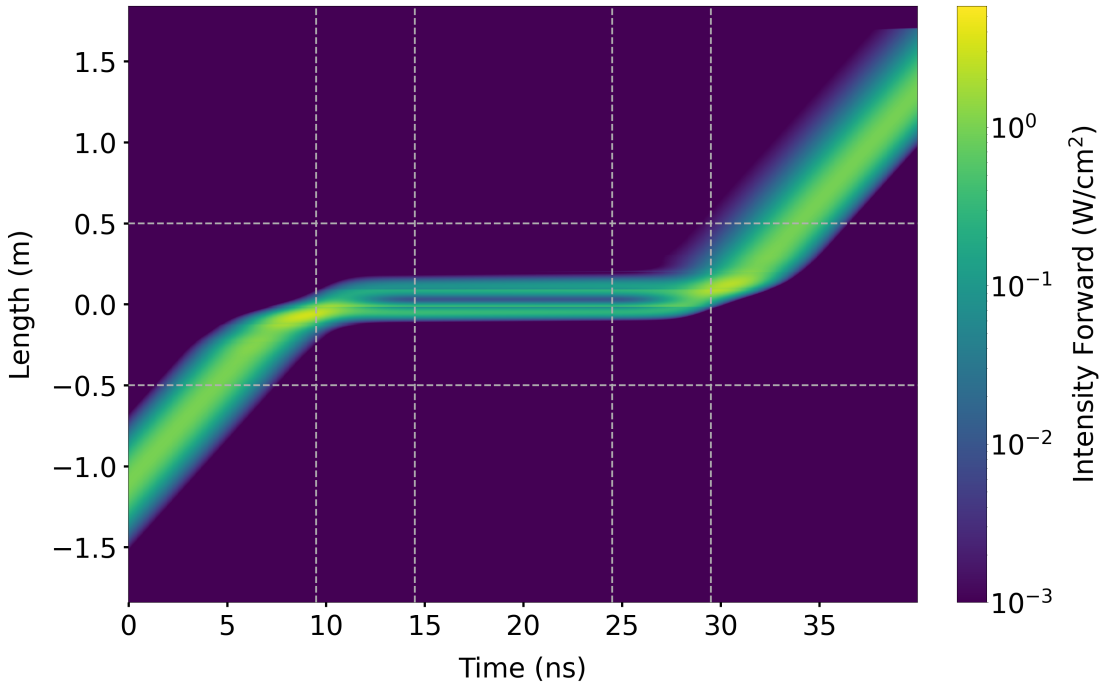

FIGURE 4.9: Figure showing the same simulation as figure 4.7(b) but with a Gaussian apodisation profile.

The figure shows the same simulation as figure 4.7(b) but with a Gaussian apodisation. In this case the varying grating strength and group velocity causes pulse dispersion. This can be seen in the figure as the pulse that exits the grating is been distorted by the modulation of the grating strength. Therefore, in order for the pulse to return to its original state after the time variation is applied, a flat top apodisation profile is required so that the group velocity change is uniform along the length of the pulse.

4.2.5 Model verification with finite difference simulations

One consequence of the approximations that went into developing the coupled mode equations for a time dependent coupling strength, is that the dynamics are captured by the grating strength alone and that its derivatives make a negligible contribution. This approximation is now verified by solving Maxwell's curl equations directly using a finite difference method. The starting point is to express the equations as follows

$$\frac{\partial \vec{H}}{\partial t} = -\frac{1}{\mu_0}\vec{\nabla} \times \vec{E} \tag{4.25}$$

$$\frac{\partial \vec{D}}{\partial t} = \vec{\nabla} \times \vec{H} \tag{4.26}$$

$$\vec{E} = \frac{\vec{D}}{\epsilon_0 n(t,z)^2} \tag{4.27}$$

The order in which Maxwell's equations appear above, are the order in which the finite difference update equations will be calculated. First, the $\vec{H}$ field is updated from the $\vec{E}$, then the $\vec{D}$ is updated from the $\vec{E}$ and then finally the $\vec{E}$ is updated from the $\vec{D}$ field. This way, the refractive index only enters into final stage of field update which avoids having to take account explicitly of any derivative terms.

Greater numerical efficiency is achieved by normalising the auxiliary fields as follows

$$\widetilde{H} = \sqrt{\frac{\mu_0}{\epsilon_0}}\vec{H} \tag{4.28}$$

$$\widetilde{D} = \epsilon_0 \vec{D}, \tag{4.29}$$

which transforms the field equations into the more convenient form

$$\frac{\partial \widetilde{H}}{\partial t} = -c\vec{\nabla} \times \vec{E} \tag{4.30}$$

$$\frac{\partial \widetilde{D}}{\partial t} = c\vec{\nabla} \times \widetilde{H} \tag{4.31}$$

$$\vec{E} = \frac{\widetilde{D}}{n(t,z)^2}. \tag{4.32}$$

For the simulation we are interesting in linearly polarised light, and therefore choose y-polarisation which reduces the field equations to a form that can be readily written in terms of finite differences

$$\frac{\widetilde{H}_x}{\partial t} = c\frac{E_y}{\partial z} \tag{4.33}$$

$$\frac{\widetilde{D}_x}{\partial t} = c\frac{\widetilde{H}}{\partial z} \tag{4.34}$$

$$E_y = \frac{\widetilde{D}_y}{n(t,z)^2}. \tag{4.35}$$

The finite difference equations are then generated using the procedure devised by Yee [67]. In this scheme, the electric and magnetic fields are staggered on a Yee grid which ensures that fields are divergence free and automatically satisfy boundary conditions. Applying Yee's approach, the finite difference update equations corresponding to field equations (4.33-4.35) are

$$\widetilde{H}\Big|_{t+\frac{\Delta t}{2}}^{z+\frac{\Delta z}{2}} = \tilde{H}\Big|_{t-\frac{\Delta t}{2}}^{z+\frac{\Delta z}{2}} + \frac{c\Delta t}{\Delta z}\left(E\Big|_{t}^{z+\Delta z} - E\Big|_{t}^{z}\right) \tag{4.36}$$

$$\widetilde{D}\Big|_{t+\Delta t}^{z} = \widetilde{D}\Big|_{t}^{z} + \frac{c\Delta t}{\Delta z}\left(\tilde{H}\Big|_{t+\frac{\Delta t}{2}}^{z+\frac{\Delta z}{2}} - H\Big|_{t+\frac{\Delta t}{2}}^{z-\frac{\Delta z}{2}}\right) \tag{4.37}$$

$$E\Big|_{t}^{z} = \frac{\widetilde{D}}{n^2}\Bigg|_{t}^{z}. \tag{4.38}$$

Performing a finite difference simulation is much more computational intensive than using coupled mode equations. Therefore, to perform the simulation the grating length is reduced to 4 mm with a raised cosine apodisation with a 65% flat top. The Bragg wavelength is given by $\lambda_B = 1550$ μm with a moiré period of $\Lambda_S = 24$ μm and a grating strength of $\delta n = 10^{-1}$. While a grating strength this large is not practically realisable, it becomes computationally infeasible to preform a finite difference simulation with a smaller grating strength. Therefore, for the purpose of validating the behaviour observed using the coupled mode equations (4.20) and (4.21), it is appropriate to use the larger grating strength.

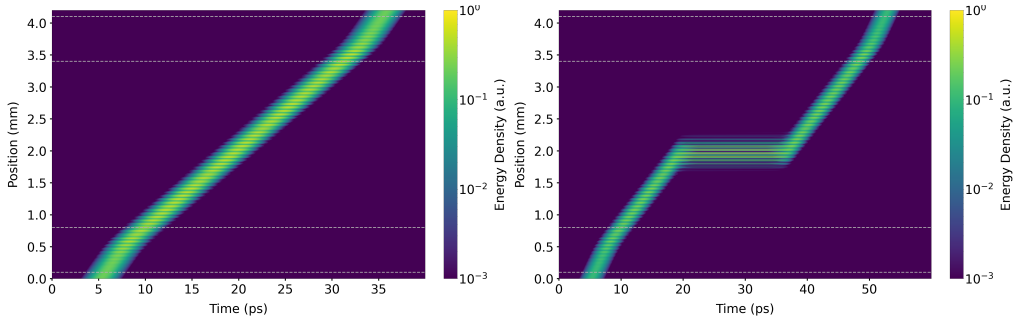

FIGURE 4.10: Finite difference simulation of (a) a pulse prograting through a static moiré grating and (b) a pulse propagating through a dynamic moiré grating

Figure 4.10(a) shows simulations of equations (4.36-4.38) for a Gaussian pulse with a bandwidth of 390 GHz at FWHM. In this simulation the grating is static with no time variation. The pulse enters the grating, experiences a reduction in group velocity and then exits the grating. Figure 4.10(b) shows the same simulation setup but with a time varying grating strength. Once again, the pulse enters the grating and undergoes a

reduction in its group velocity. Then at time $t = 18\,\text{ps}$, μ is increased to a value of 4 over a period of 5 ps. μ is then held at this value for 10 ps before being decreased back to zero over a period of 5 ps.

Figure 4.10b shows that simulating the time-dependent grating strength with finite differences exhibits the same behaviour as the model using coupled mode theory. This justifies the approximations that went into developing the coupled mode equations. Moreover the finite difference simulation was performed with a grating strength two orders of magnitude greater than was demonstrated with coupled mode theory. Therefore, the behaviour is not limited to only small initial grating strengths.

4.3 Bandwidth modulation

4.3.1 Group velocity induced bandwidth modulation

In the previous section the, the grating strength was varied symmetrically to store and release a pulse. When the pulse was fully localised within the device, the grating strength was increased, and with the pulse fully localised within grating, the grating strength was returned to its original value. In this section we look at varying the grating strength asymmetrically. There are of course two ways to do this. Start with a smaller grating strength and increase it, or start with larger grating strength and decrease it. In either case the asymmetric switching means the grating strength is not returned back to its original value. By using asymmetric switching it is possible to stretch or compress the bandwidth of a pulse as will be discussed in the following.

To understand this behaviour, it is first instructive to consider what happens to a pulse propagating through a static moiré grating. If the pulse has a spectral bandwidth that sits within the transmission band, then as the pulse enters the grating, its leading edge will experience a slower group velocity than the part of the pulse outside the grating. Therefore, the pulse outside the grating will travel faster than the part of the pulse inside the grating. This causes the pulse to compress. This can be made more explicit by considering a pulse with a FWHM spatial length of Δz. Then if the group velocity inside the grating is v_g and the group velocity outside is v_0, then Δz will be compressed by a factor of v_g/v_0. The situation is reversed when the pulse exits the grating. The leading edge exits the grating, travelling faster than the rest of the pulse still inside the grating. As a consequence, the pulse is stretched by a factor v_0/v_g. The effect of applying the compression factor and the subsequently the stretching factor means that the net effect is to leave the spatial length Δz unchanged. As the grating considered is static, the pulse compression and stretching is due to grating dispersion and as such the pulse bandwidth is unaltered. This, however, is not the case in a dynamic grating.

Consider now a pulse that is fully localised within a moiré grating. If the grating strength is changed uniformly along the length of the pulse so that its group velocity is altered from v_g to $\tilde{v}_g$, the spatial length of the pulse Δz will not change. This is because, unlike in the previous case considered, the change in group velocity is experienced uniformly along the pulse length, and so there is no spatial compression or stretching as different parts of the pulse experience different group velocities. Now if the variation of the grating strength is asymmetric, so that the grating strength is not returned to its original value, then when the pulse exits the grating, the stretching factor will not be v_0/v_g, but $v_0/\tilde{v}_g$ as the group velocity has been altered by the change in the grating strength. This means that the compression and stretching of the pulse as it enters and exits the grating does not cancel like it did in the case of a static grating. Instead, the spatial length of the pulse is altered by a factor of $v_g/\tilde{v}_g$, giving

$$\Delta\tilde{z} = \frac{v_g}{\tilde{v}_g}\Delta z \tag{4.39}$$

where $\Delta\tilde{z}$ is the modified pulse length. As the spatial length of the pulse exiting the grating is different from that which entered it, varying the grating strength must change the bandwidth of the pulse. For a pulse with a FWHM bandwidth of Δf, its bandwidth is related to its spatial length Δz through a Fourier a transform by $\Delta f = 4c\ln(2)/(\pi\Delta z)$. Then by using equation (4.39), the modified bandwidth is related to the original pulse bandwidth by

$$\Delta\tilde{f} = \frac{\tilde{v}_g}{v_g}\Delta f \tag{4.40}$$

where $\Delta\tilde{f}$ is the modified bandwidth of the pulse exiting the grating. Notice that the $\tilde{v}_g/v_g$ scaling for the bandwidth is the factor by which the delay-bandwidth product was enhanced. Therefore, the delay-bandwidth product transforms by $\Delta t\Delta f \rightarrow \Delta t\Delta\tilde{f}$.

From equation (4.40), if the group velocity is increased by asymmetrically increasing the grating strength, then the pulse bandwidth will decrease. Conversely, if the group velocity is decreased, the result is to stretch the bandwidth. A point to note is that the product of the pulse length and bandwidth remains constant

$$\Delta\tilde{z}\Delta\tilde{f} = \Delta z\Delta f. \tag{4.41}$$

4.3.2 Simulation of compression and streching

This behaviour can be demonstrated by performing simulations similar to those done in section 4.2.3. However, in this case the windowing function is chosen so that it either

only switches on or off the variation in the grating strength, but not both.

First, consider the case of increasing the grating strength when a pulse is localised inside a moiré grating and remains at the increased value. Figure 4.11(a) shows a simulation of a pulse with an initial bandwidth of $\Delta z = 700$ Mhz and spatial length of $\Delta z = 38$ cm. The grating has a length of 1m, an initial grating strength of $\delta n = 10^{-3}$ and moiré period of $\Lambda_S = 4$ mm. The grating has a raised cosine apodisation profile, with the flat top portion of the grating comprising 70% of the total grating length. The grating has a Bragg wavelength of $\Lambda_B = 1550$ nm which is also the carrier wavelength of the pulse which ensures that the pulse bandwidth is centred on the grating transmission band. In the simulation the pulse propagates into the moiré grating and at time $t = 12$ ns the windowing function activates. The activation time for the windowing to go from 0 to 1 is 5 ns and the windowing strength has a value $\mu = 0.33$. As can be seen in the figure, the increase in the grating strength causes the pulse to slow. Without the grating strength reduced back to its original value, the reduced group velocity causes the spatial length of the pulse to stretch by a factor of 2 as it exits the grating.

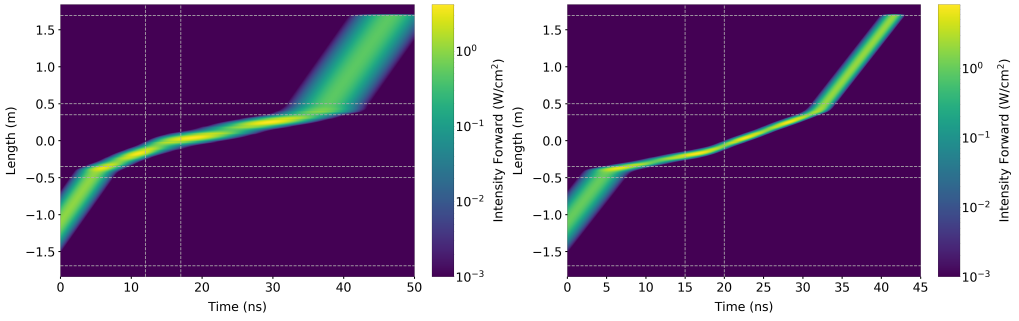

(a) (b)

FIGURE 4.11: Intensity profile of a pulse propagating through (a) a dynamic spectrum-compressing moiré grating and (b) a dynamic spectrum-broadening moiré grating. (c) Comparison of the input and output pulse spectra from (a) and (b). Parameters as in Fig. 4.7. The time variation magnitude has value $\mu = 0.33$ in both (a) and (b).

Figure 4.11(b) shows a simulation of the opposite behaviour. The set up of the simulation is exactly the same as that in figure 4.11(a), but the time windowing is initially set to one and is switched off once the pulse is within the grating. This has the effect of reducing the overall grating strength from its initial value. The simulation starts the same as the previous simulation, and as the pulse enters the grating the initial group velocity is lower compared with figure 4.11(a) which due to the increased initial grating strength. Then at time $t = 12$ ns the windowing is turned off over a period of 5 ns. The pulse then begins to speed up as the grating strength is reduced. When the pulse emerges out of the grating, the increased group velocity causes the spatial length of the pulse to compress by a factor 2.

In both simulations the scaling factor for the spatial length is 2. By equation (4.41), the product of the spatial length and pulse bandwidth must remain constant before and

after the grating. Therefore, in figure 4.11(a) where the spatial length is stretched by a factor of 2, it must be the case that the bandwidth is compressed by the same factor. Similarly, in figure 4.11(b) where the spatial length is compressed by a factor of 2, the bandwidth must also be stretched by a factor of 2. To verify that the analysis leading to equation (4.41) is correct, a Fourier transforms can be taken of the simulations in figures 4.11(a) and 4.11(b). Then the pulse spectrum can be compared before and after the grating which is shown in figure 4.12.

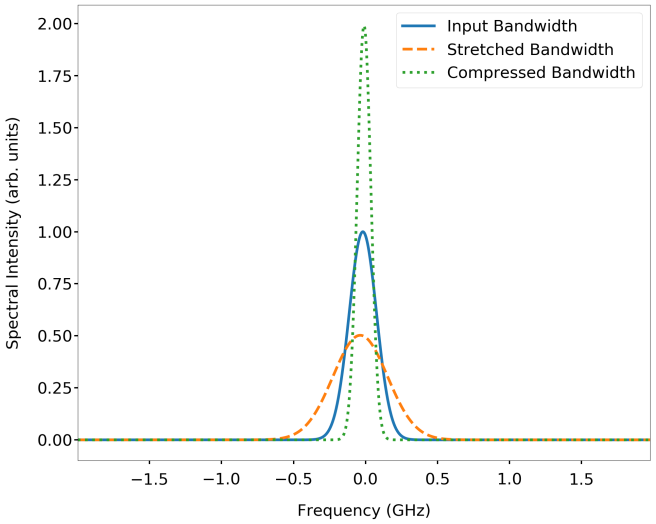

FIGURE 4.12: Comparison of the input and output pulse spectra from figures 4.11(a) and 4.11(b)

The blue line in figure 4.12 shows the initial pulse spectrum in both figures 4.11(a) and 4.11(b) before the pulse enters the gratings. The dotted green and orange dotted lines show the pulse spectrum after exiting the gratings in figures 4.11(a) and 4.11(b) respectively. It is clear form figure 4.12 that the stretching and compression of the bandwidth also scales with a factor of 2 as expected.

Figure 4.13 shows how the spectrum compression factor varies with respect to Λ_S and μ. Comparing figure 4.13 to figures 4.13 and 4.6a, extreme spectrum compression corresponds to ultra-slow group velocities. This is not surprising as the compression factor is dependent on the change in the group velocity. In the case of increasing μ which leads to lower group velocities, the overall change in the group velocity is larger and so, too, is the compression factor. The spectrum stretching factor can be read from figure 4.13 by taking the reciprocal of the compression factor.

By dynamically increasing the grating strength by factors of two or three, it is possible to stretch or compress the pulse by several orders of magnitude. One benefit of this method which can be seen from figure 4.12, is that the spectrum maintains a Gaussian

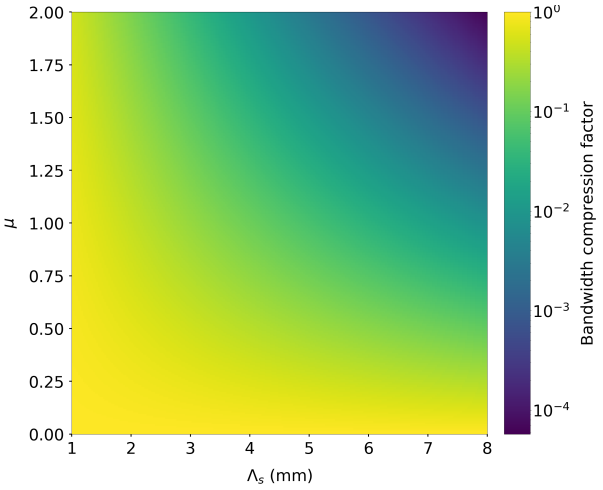

FIGURE 4.13: Bandwidth compression factor depending on Λ_S and μ in a dynamic moiré grating with parameters $L = 20\text{cm}$, $\lambda_B = 1.55\mu\text{m}$, $\bar{n} = 1.445$, $\delta n = 10^{-3}$.

shape. This is due to the refractive index changing uniformly across the pulse, something that does not hold true in other spectral broadening methods such as self-phase modulation in a Kerr medium [68].

4.4 Device realisation in an electro-optic $\chi^{(2)}$ medium

The analysis so far has been kept general so that the underlying features of dynamic moiré gratings can be explored. The task of realising a dynamic grating is not easy. A number of approaches have been looked at previously including using Brillouin scattering [55], an eribium-doped fibre [69] and excited free carriers [70]. This section proposes a new approach using electro-optic gratings based on a $\chi^{(2)}$ nonlinear medium. A common phase-matching method for second order $\chi^{(2)}$ processes is to use quasi-phase matching which involves periodically modulating the sign of the $\chi^{(2)}$ and was discussed in section 2.3.1. Although this produces a grating in the second order material susceptibility, applying an external quasi-static electric field induces a linear grating [71]. To see why this is the case, first consider a standard poling profile for quasi-phase matching given by (2.98). Typically, the poling profile is a square wave so that the change in sign of $\chi^{(2)}$ is discrete. The standard poling profile has only a single grating term and so an additional grating term needs to be added to produce a moiré style grating which can be done as follows

$$\chi^{(2)}(z) = \chi^{(2)}\text{sgn}\big[\sin(K_S z)\big]\text{sgn}\big[\sin(K_B z)\big]. \tag{4.42}$$

There are now two grating envelop terms $\sin(K_S z)$ and $\sin(K_B z)$ which are fulfilling the roles of the moiré and Bragg terms respectively. Written in the form given by (4.42),

the square wave applied to each of the envelop terms means that the profile actually describes a π phase shifted grating. Comparing equations (2.98) and (4.42), the Bragg envelope is now determined by the poling period so that $K_B = 2\pi/\Lambda$. If the moiré period Λ_S is taken to be integer multiples of the poling period, then after every moiré period there will be a single double-length poling period which has the effect of inserting a π phase shift into the phase of the Bragg envelope. An illustration of this is shown in figure 4.14. Superstructure poling profiles have been previously studied for multi-wavelength conversion in quasi-phase matched nonlinear crystals [72, 73].

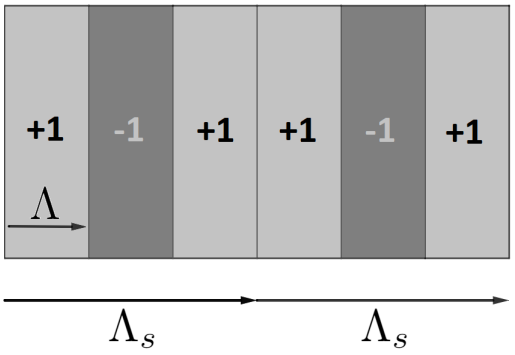

FIGURE 4.14: An example $\chi^{(2)}$ moireé grating with a moireé period that is three times the length of the poling period. The effect of the moireé period is to create a single double-length poling period after each moireé period.

The square wave of the Bragg term $\mathrm{sgn}\big[\sin(K_B z)\big]$ in equation (4.42) can be expressed as Fourier series by

$$\chi^{(2)}(z) = \frac{4\chi^{(2)}}{\pi}\mathrm{sgn}\big[\sin(K_S z)\big]\sum_{m=1}^{\infty}\frac{\sin\big(K_B(2m-1)z\big)}{2m-1}. \tag{4.43}$$

In developing coupled mode equations, making a SVEA means that only oscillations which are slowly varying with respect to the Bragg wavelength survive. Therefore, the only mode in equation (4.43) that contributes is $m = 1$; all other oscillation can be neglected and so the poling profile reduces to

$$\chi^{(2)}(z) = \frac{4\chi^{(2)}}{\pi}\mathrm{sgn}\big[\sin(K_S z)\big]\sin\big(K_B z\big). \tag{4.44}$$

To developed the couple modes equations, the quasi-static electric field has to be added to the overall electric field can can be done with the following expression

$$E(t,z) = E_D(t,z) - \partial_t A_{t,z}. \tag{4.45}$$

where $A_{t,z}$ is the vector potential ansatz given by equation (3.59). From the general nonlinear Lagrangian given by equation (3.35), the terms for second order processes are given by

$$\mathcal{L} = \frac{\epsilon_0}{3}\chi^{(2)}_{ijk}E_iE_jE_k. \tag{4.46}$$

By substituting the poling profile (4.44) and the expression for the electric field (4.45) into the second order Lagrangian term (3.35), the Lagrangian term reduces to

$$\mathcal{L}_{nlin} = \frac{4\epsilon_0 i\chi^{(2)}E_D(t,z)}{\pi}\mathrm{sgn}\big[\sin(K_Sz)\big]\left(v^*u\,e^{2i\Delta z} + u^*v\,e^{-2i\Delta z}\right) \tag{4.47}$$

after making the usual approximations. Combining this with the linear terms gives the full Lagrangian for the system

$$\begin{aligned}\mathcal{L} = {} & \frac{i\epsilon_0\bar{n}^2}{\omega}\left(u^*\partial_tu - u\partial_tu^* + v^*\partial_tv - v\partial_tv^*\right)\\ & + \frac{i\epsilon_0\bar{c}^2\beta}{\omega^2}\left(u^*\partial_zu - u\partial_zu^* + v^*\partial_zv - v\partial_zv^*\right)\\ & + \frac{4\epsilon_0 i\chi^{(2)}E_D(t,z)}{\pi}\mathrm{sgn}\big[\sin(K_Sz)\big]\left(v^*u\,e^{2i\Delta z} + u^*v\,e^{-2i\Delta z}\right).\end{aligned} \tag{4.48}$$

The equations of motion are derived in the usual way by varying the Lagrangian with respect to the forward and backward modes u^* and v^* giving

$$\frac{1}{v_p}\partial_tu + \partial_zu = -\kappa^{(2)}\mathrm{sgn}\big[\sin(K_Sz)\big]ve^{-2i\Delta z}. \tag{4.49}$$

$$\frac{1}{v_p}\partial_tv - \partial_zv = -\kappa^{(2)}\mathrm{sgn}\big[\sin(K_Sz)\big]ue^{2i\Delta z}. \tag{4.50}$$

Comparing with equations (3.71) and (3.72), this set of equations provide coupling between the forward and backward modes through the nonlinear coupling term $\kappa^{(2)}$ which is given by

$$\kappa^{(2)}(t,z) = \frac{2\beta\chi^{(2)}E_D(t,z)}{\bar{n}^2\pi}. \tag{4.51}$$

They have a superstructure envelope given by $a(z) = \mathrm{sgn}\big[\sin(K_Sz)\big]$, which as previously stated gives a π phase shifted grating. By comparing the couplings (4.51) and (4.22), the induced grating strength by the applied quasi-static field is

$$\delta^{(2)}(t,z) = \frac{4\chi^{(2)}E_D(t,z)}{\bar{n}\pi}. \tag{4.52}$$

This equation demonstrates the intended goal. As the change in the grating strength is determined by the applied quasi-static field, and the applied quasi-static field can be varied in time, then so too can the grating strength. A grating can be created by switching the field on and removed by switching it off. Varying the strength of the applied field will serve to broaden and narrow the transmission band; which in turn allows for the dynamic control of the group velocity. The key resource of interest is the change in the grating strength. If an electro-optic grating was used exclusively, some of that resource would need to be used to generate the initial grating. Therefore it would be beneficial to combine an electro-optic grating with a linear grating so that the coupling becomes

$$\kappa(t,z) = \kappa \sin(K_S z) + \kappa^{(2)}(t,z)\mathrm{sgn}\big[\sin(K_S z)\big]. \tag{4.53}$$

Then the linear grating provides the initial grating and the applied quasi static field can be used entirely to vary group velocity through the electro-optic grating. The two gratings need to have the same underlying Bragg and moireé periods. The combined maximum coupling strength is then given by $\kappa + \kappa^{(2)}$.

A natural choice of medium for a realisable device would be a thin film lithium niobate waveguide [74]. Firstly, lithium niobate thin films can have submicron thicknesses. This means that the electric field density within the waveguide can be large without needing to apply a large electric field. This makes the coercive field strength the limiting factor for the maximum field that can be applied; above which the poling is destroyed. The approximate reported coercive field strength for a lithium niobate thin film is 21 V/μm [75]. Another limiting factor affecting fabrication is the poling period. The current technological limits allow poling periods down to approximately 750 nm [76, 77] in lithium niobate thin films. This would correspond to a Bragg wavelength of around 3 μm which sits within the transparency window for lithium niobate. The induced grating strength with an applied quasi-static field of half the coercive strength and at a Bragg wavelength of 3 μm, would be on the order of 10^{-4} which is an order of magnitude small than in the analysis carried out in this chapter.

4.5 Summary

This chapter has explored using dynamic moiré gratings to create an optical storage device. The general properties of moiré gratings and their close connection to π phase-shifted grating were discussed. While there are no analytical solutions for the moiré

grating, it was shown how general solutions could be constructed at the Bragg wavelength and the important role apodisation plays. Next the properties of the slow light transmission band and its dependence of the grating strength and moiré period were discussed. To model pulse propagation through a dynamic moiré grating, coupled mode equations with a time dependent grating strength were introduced. It was then demonstrated through simulations of the coupled mode equations, that increasing the grating strength in time while a pulse was propagating though the grating could result in a significant reduction in the group velocity of the pulse. By subsequently decreasing the grating strength the pulse could be returned to its original state. Therefore by dynamically controlling the grating strength a pulse could be stored and released on demand. To verify the assumptions that went into deriving the couple mode equations a finite difference model applied directly to Maxwell's equations was introduced. It was then demonstrated that simulations using the finite difference model exhibit the same behaviour as the simulations using coupled mode theory, validating the coupled mode model. Next it was shown that asymmetrically varying the grating strength could be used to modulated the frequency spectrum of a pulse causing pulse compression or stretching. Finally a method of realising a dynamic moiré grating was suggested by using an electro-optic grating. By applying a strong quasi-static electric field, an electro-optic grating induces a linear coupling. Varying the strength of the applied electric field results in varying the grating strength, thus producing a dynamic moiré grating.

Chapter 5

Grating Delay Lines

Optical silica fibres have very low losses of around 0.14 dB/km at 1550 nm [78, 79] which has been the culmination of many decades of research and development. Therefore, they represent an ideal candidate for optical storage and quantum memory devices. By creating a loop of fibre, a pulse can circulate around the loop until it needs to be retrieved. The length of the loop places a limitation on the retrieval times of the pulse to integer multiples of the time taken for the pulse to travel the length of the loop.

This chapter looks at investigations into creating a fibre delay line by using dynamic gratings that create adjustable rejection bands using the nonlinear optical Kerr effect. The theoretical analysis will where possible be kept general so that it is applicable to other methods of varying the refractive index, but specific examples will be given using the optical Kerr effect.

The proposed device looks to create analogous behaviour to a fibre delay line by writing two gratings at each end of a length of fibre. A probe pulse inside the fibre that is resonant with the gratings will then be trapped between them. The difficulty is then getting the probe pulse in and out of device. This can be done by dynamically controlling the Bragg wavelength by inducing a small change in the refractive index $\bar{n}$. If the Bragg resonance is shifted sufficiently such that a signal pulse originally resonant with the grating can propagate through it, then varying the refractive index can allow the pulse to enter and exit the device.

Using the optical Kerr effect to induce the refractive index change has the potential of producing switching times on the order of picoseconds. However, due to the very small strength of $\chi^{(3)}$ in silica, the corresponding change in the refractive index is also very small, on the order of $\Delta n \approx 10^{-6} - 10^{-5}$ which is constrained by optical damage threshold of silica [80]. Typically when using the optical Kerr effect, $\chi^{(3)}$ is characterised in terms of the nonlinear refractive n_2. Throughout this chapter, the nonlinear refractive is taken to be $n_2 = 2.74 \times 10^{-16}$ cm^2/W [81] at a carrier wavelength of 1053 nm.

There are two choices for how to construct the device. The first is to make the gratings with a grating strength roughly the same size as the change that can be induced by the optical Kerr effect. Then the entirety of the grating band gaps can be dynamically shifted allowing a pulse to pass through. Gratings with such a weak grating strength will have to be of a considerable length in order to have high enough reflectance to effectively trap a pulse. There have been recent developments in constructing very long silica fibre gratings with lengths up to 1 m [82]. Long gratings present additional switching difficulties using the optical-Kerr effect as the required pump pulse needs to be spatially large enough to shift the Bragg resonance along the length of the grating.

The second option is to use shorter gratings with a larger grating strength. In this case the refractive index change only shifts the band gap partially and therefore the resulting passband is very close to the edge of the band gap. As shown in section 2.2.1.2, the band gap generated by strong grating strengths generates significant amounts of second order dispersion which causes pulse broadening. One way to mitigate this problem is to use a dispersion cancelling moiré grating [35] which was discussed in section 2.2.3.

In either case, the size of the band gap shift is dependent on the change in the refractive index. Therefore, using the optical Kerr effect places a substantial limitation on the available bandwidth. The price paid for faster switching times is reduced bandwidth. This makes such a device, if it could be realised, of little practical use for telecoms applications where pulses typically have gigahertz bandwidths. It could potentially be used with narrow bandwidth single photons.

5.1 Coupled mode equations for linear gratings in a $\chi^{(3)}$ medium

This section develops the coupled mode equations for a device with two linear gratings in a $\chi^{(3)}$ medium using the variational methods developed in chapter 3.1. The grating profile for the device is given by equation 2.84, where the apodisation function used is given by

$$f(z) = \begin{cases} 0 & z < z_1 \\ \exp\left(-\alpha_A \left(\frac{z-(z_1+L_g/2)}{L_g} \right)^2 \right) & z_1 \leq z \leq z_2 \\ 0 & z_2 < z < z_3 \\ \exp\left(-\alpha_A \left(\frac{z-(z_3+L_g/2)}{L_g} \right)^2 \right) & z_3 \leq z \leq z_4 \\ 0 & z > z_4. \end{cases} \tag{5.1}$$

The length of the gratings is denoted by L_g and the starting point of the first grating is denoted by z_1. The end point of the first grating is then given by $z_2 = z_1 + L_g$. Similarly the starting location of the second grating is denoted by z_3 and the end by $z_4 = z_3 + L_g$. In this way, the positions and extents of the two gratings can be handled entirely within the apodisation function.

A signal pulse resonant with the linear gratings will be coupled into forward and backward modes $u(t,z)$ and $v(t,z)$ respectively. An appropriate ansatz for the vector potential is then given by

$$A_s = -\frac{i}{\omega_1}u(t,z)e^{i(\beta_1 z-\omega_1 t)} - \frac{i}{\omega_1}v(t,z)e^{-i(\beta_1 z+\omega_1 t)} + c.c. \tag{5.2}$$

A high intensity pump field that is used to alter the Bragg condition of the linear gratings is chosen such that it is spectrally distinct from the grating resonances and is therefore composed of a forward mode $p(t,z)$ only. An appropriate vector potential ansatz is then

$$A_p = -\frac{i}{\omega_2}p(t,z)e^{i(\beta_2 z-\omega_2 t)} + c.c. \tag{5.3}$$

The total vector potential ansatz is given by the sum of the signal and pump vector potentials,

$$A = A_s + A_p. \tag{5.4}$$

The frequency and propagation constant of the signal modes are given by ω_1 and β_1 respectively and for the pump mode they are denoted by ω_2 and β_2 respectively. The carrier wavelength of the signal is chosen as $\lambda_1 = 1550\,\text{nm}$ to coincide with low loss in silica. The pump wavelength is set to $\lambda_2 = 1053\,\text{nm}$ which is far removed from the grating resonance linewidths and as previously discussed has a non linear refractive of $n_2 = 2.74 \times 10^{-16}\ \text{cm}^2$.

The coupled mode equations can be derived by substituting the grating profile (2.84) and the vector potential (5.4) into the following Lagrangian

$$\mathcal{L} = \frac{\epsilon_0}{2}n^2\left(\partial_t A\right)^2 - \frac{1}{2\mu_0}\left(\partial_z A\right)^2 + \frac{\epsilon_0}{4}\chi^{(3)}\left(\partial_t A\right)^4, \tag{5.5}$$

and then making rotating wave, slowly vary envelope and neglecting small term approximations. The Lagrangian (5.5) follows from equation (3.54) by taking an x-polarised vector potential, neglecting the $\chi^{(2)}$ non linearity and taking $\chi^{(3)} = \chi^{(3)}_{xxxx}$. The linear

part of the Lagrangian, $\mathcal{L}_{lin}$, for the forward and backward signal modes is the same as in equation (3.67). The linear part of the Lagrangian for the pump field is given by

$$\mathcal{L}_{plin} = \frac{i\epsilon_0 \bar{n}_2^2}{\omega_2}\left(p^*\partial_t p - p\partial_t p^*\right) + \frac{i\epsilon_0 c^2 \beta}{\omega_2^2}\left(p^*\partial_z p - p\partial_z p^*\right). \tag{5.6}$$

The signal modes are taken to be at low intensity so that the resulting cross phase and self phase modulations terms are negligible. Then, the only terms relevant in the nonlinear Lagrangian are

$$\mathcal{L}_{pnlin} = \frac{\epsilon_0}{4}\chi^{(3)}(p^*p)(6p^*p + 24u^*u + 24v^*v). \tag{5.7}$$

The total Lagrangian is then the sum of the Lagrangian terms

$$\mathcal{L} = \mathcal{L}_{lin} + \mathcal{L}_{plin} + \mathcal{L}_{pnlin}. \tag{5.8}$$

The coupled mode equations are then derived by varying the Lagrangian with respect to the modes u^*, v^* and p^*, which gives

$$\frac{1}{v_p}\partial_t u + \partial_z u = i\kappa v e^{-2i\Delta z} + \frac{3i\beta_1\chi^{(3)}}{\bar{n}_1^2}(p^*p)u, \tag{5.9}$$

$$\frac{1}{v_p}\partial_t v - \partial_z v = i\kappa u e^{2i\Delta z} + \frac{3i\beta_1\chi^{(3)}}{\bar{n}_1^2}(p^*p)v, \tag{5.10}$$

$$\frac{1}{v_p}\partial_t p + \partial_z p = \frac{3i\beta_2\chi^{(3)}}{2\bar{n}_2^2}(p^*p)p. \tag{5.11}$$

5.2 Steady state requirements for shifting the band gap

5.2.1 Steady state refractive index change

The Kerr effect as described in section 2.3.2, is a $\chi^{(3)}$ nonlinear process which induces a change in the refractive index with the application of a strong pump field. There are two separate interactions. The first is SPM, where the pump induces a refractive index change at its own carrier wavelength. The second is XPM which is an induced refractive index change at a different wavelength to the pump. In equations (5.9) and (5.10), the XPM terms alter the underlying Bragg condition. Therefore, a grating can

be detuned and a signal pulse that would ordinarily be resonant with the gratings can pass through unhindered.

The nonlinear XPM interaction between the pump and probe fields will in general be complicated. It is therefore useful to first look at a simplified case where the fundamental modes are taken to be in a steady state. Along with this an undepleted pump approximation is assumed so that the power transfer from the pump to the signal modes is considered negligible. The pump field can then be taken to be constant and the system of coupled mode equations reduces to

$$\partial_z u = i\kappa v e^{-2i\Delta z} + \frac{i\beta_1}{\bar{n}}\Delta n u \tag{5.12}$$

$$\partial_z v = -i\kappa u e^{2i\Delta z} - \frac{i\beta_1}{\bar{n}}\Delta n v. \tag{5.13}$$

In equations (5.12) and (5.13), Δn is the change in the refractive index induced by XPM from the pump and is given by

$$\Delta n = \frac{3\chi^{(3)}}{\bar{n}}|p|^2. \tag{5.14}$$

It is in general more useful to express the refractive index change (5.14) in terms of the nonlinear refractive index (2.109) and the pump intensity I defined by equation (2.110) giving

$$\Delta n = \frac{8\bar{n}_p n_2}{\bar{n}} I. \tag{5.15}$$

Figure 5.1 shows the change in the refractive index versus intensity. The maximum intensity in the figure goes up to the optical damage threshold for a silica fibre which is approximately 3 GW/cm^2 [80]. This limits the maximum refractive change to approximately 6×10^{-6} which places significant limitations on the shiftable bandwidth.

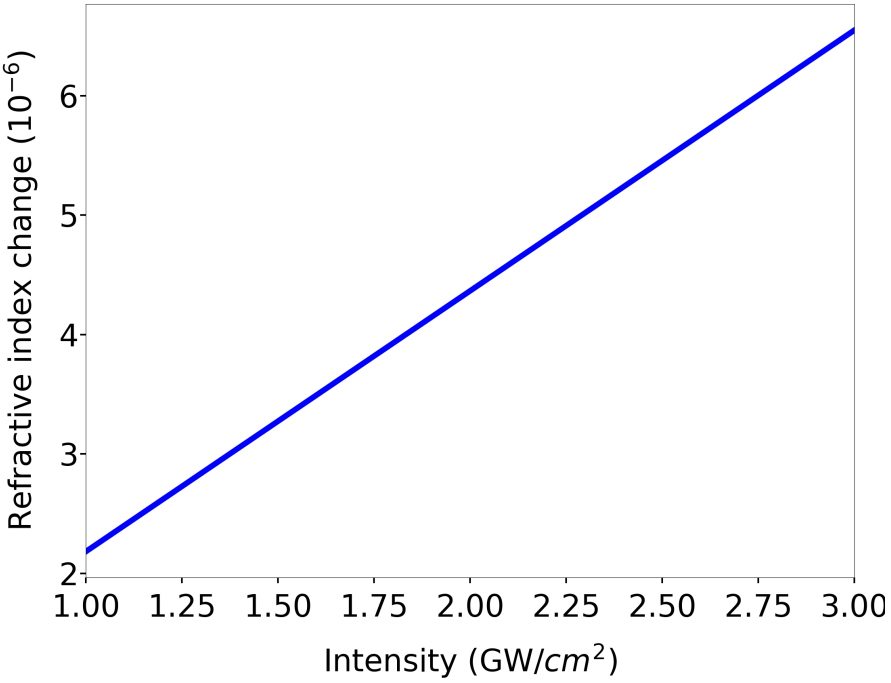

FIGURE 5.1: Refractive index change induced by XPM from a strong pump pulse. The refractive index calculated at 1550 nm, with pump carrier wavelength at 1053 nm

The wavelengths corresponding to the ends of the Bragg band gap were derived in section 2.2.1.2. The band edge wavelengths with a refractive index change Δn become

$$\lambda_{\pm}^{'} = \Lambda_B \Big(2(\bar{n} + \Delta n) \pm \delta n \Big), \tag{5.16}$$

which shifts the Bragg wavelength to

$$\lambda_B^{'} = 2\Lambda_B(\bar{n} + \Delta n). \tag{5.17}$$

Therefore applying a refractive index change Δn increases the Bragg wavelength. The shiftable bandwidth can then be calculated from the change in the Bragg wavelength which is given by

$$\Delta f = \frac{c\Delta n}{2\Lambda_B \bar{n}(\bar{n} + \Delta n)}. \tag{5.18}$$

Figure 5.2 shows a plot of equation (5.18) for increasing pump intensity. The optical damage threshold puts the maximum bandwidth using the optical Kerr effect at close to 900 MHz.

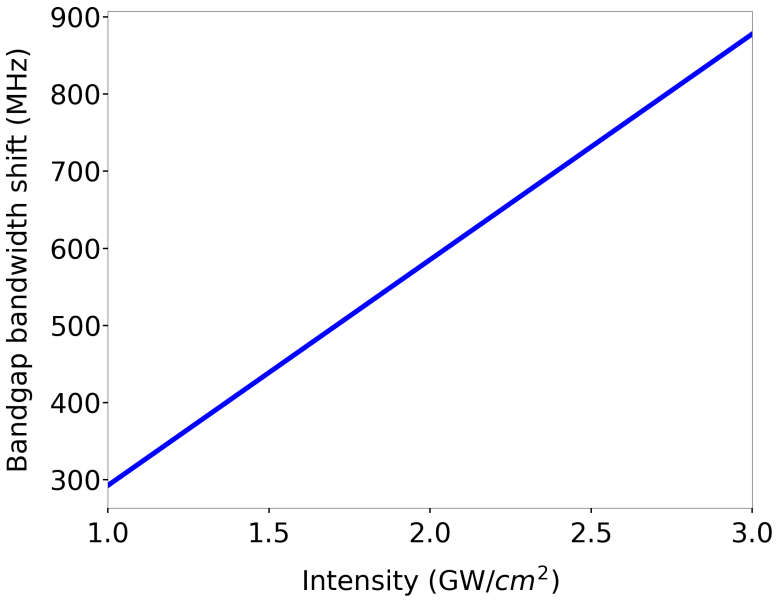

FIGURE 5.2: Shifted band gap bandwidth in a silica fibre Bragg grating induced by XPM from a strong pump pulse. Bragg wavelength is at 1550 nm, with pump carrier wavelength at 1053 nm

If the change in the refractive index is such that the lower wavelength of the shifted band gap is equal to the upper wavelength of the original band gap

$$\lambda_{-}^{'} = \lambda_{+}, \tag{5.19}$$

then the original band gap will have been fully shifted by the refractive index change. Evaluating equation (5.19) shows that in order to shift the entire band gap, the change in the refractive index must be equal to grating strength

$$\delta n = \Delta n. \tag{5.20}$$

Under this circumstance, if the bandwidth of a probe pulse falls completely inside the original band gap, then when the band gap is shifted the probe pulse will no longer be resonant with the grating. It will then be able to propagate unimpeded through the grating. In accordance with equation (5.20), if the refractive index is induced through XPM, then the grating strength will have to be on the order of 10^{-6} by figure 5.1. Having such a small grating strength means that the grating length will have to be of considerable size in order to have high enough reflectance to effectively be able to reflect and subsequently trap the probe pulse. Figure 5.3 shows a plot of the grating length against the maximum grating reflectance as given by equation (2.83).

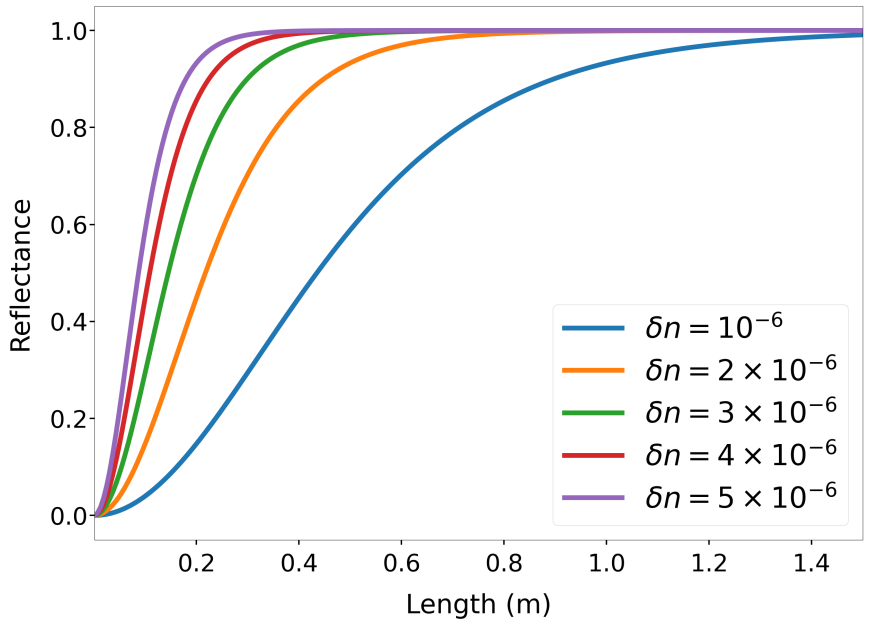

FIGURE 5.3: Reflectance versus grating length for grating strengths from $\delta n = 10^{-6}$ to $\delta n = 5 \times 10^{-6}$. The gratings have a Bragg wavelength given by λ_B =1550 nm.

A grating strength of $\delta n = 2 \times 10^{6}$ needs a grating length of approximately 1 metre in order to have strong reflectance. This corresponds to a pump intensity of 1.16 GW/cm^2 to fully shift the band gap which is well within the damage threshold.

As an example, take a pump pulse with intensity 1.5 GW/cm^2. From figure 5.1 this corresponds to a refractive index change of 3.3×10^{-6}. If a grating has a fully shiftable band gap by this refractive index change, then its grating strength will also have to be 3.3×10^{-6}. Using figure 5.2, the grating will have a band gap of approximately 350 MHz and by figure 5.3 will need a length of 75cm in order to have strong reflectance. Figure 5.4 shows a plot of the reflectance of this grating. The blue line shows its reflectance when it is in an unmodified state and the orange line shows the reflectance when the pump field is applied.

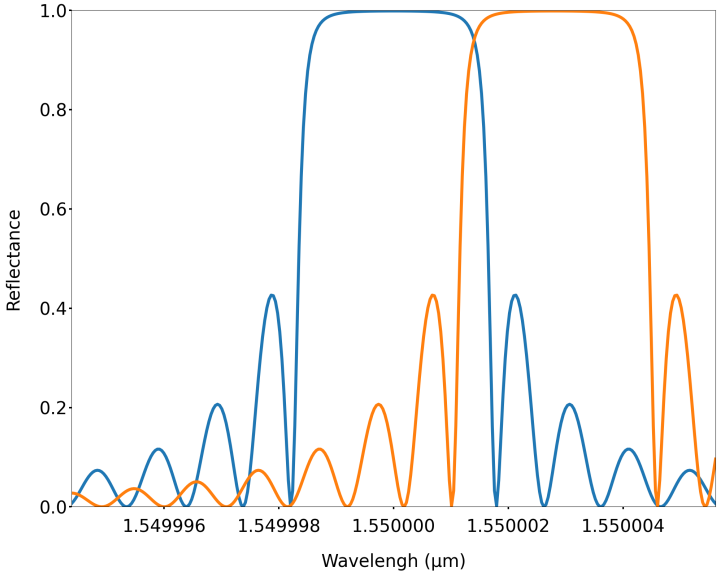

FIGURE 5.4: A plot comparing the reflection spectrums for an unapodised Bragg grating with and without an XPM shifted Bragg wavelength. The blue line shows the unmodified reflection spectum and the orange line the reflection spectrum with XPM applied. The grating has parameters $L = 0.75$ m, $\lambda_B = 1550nm$, $\delta n = 3.3 \times 10^{-6}$ and pump intensity of 1.5 GW/cm^2.

The first issue to notice is that the bandwidth is not totally shifted. There is some overlap between the original and shifted band gap. This is because the band edge wavelength calculations were done using a semi-infinite grating. In practice, the band edges of a grating of finite size are not perfectly sharp. This leaves some overlap between the original and shifted band gap. The second issue is that without apodisation, the shifted bandwidth is now occupied by side lobing. This will cause reflections and pulse distortion meaning that the probe pulse cannot cleanly pass through the grating. To resolve this issue it is necessary to apply an apodisation to surpress the sidelobing. Figure 5.5a. A Gaussian apodiation of the form given by equation (2.85) has been applied with an apodisation strength of $\alpha_A = 16$. This suppresses the side lobbing, but the overall grating strength has been reduced as a result and consequently so has the reflectance. In order to increase the reflectance, the length of the grating needs to be extended. Figure 5.5b shows the same grating but with the grating length increased to two metres so that the grating has strong reflectance. A grating of this length is beyond the current fabrication limits of ultra-long gratings which is at present about one metre [82].

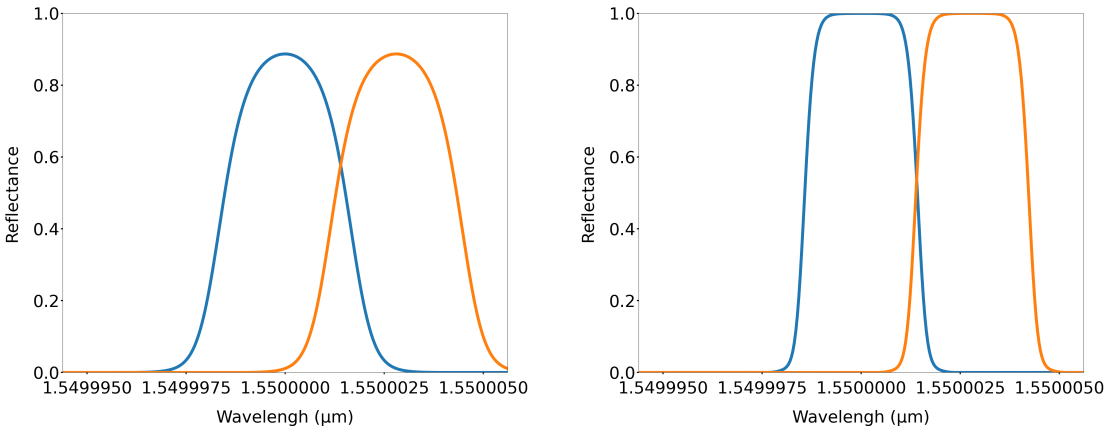

(a) (b)

FIGURE 5.5: Plots comparing the reflection specta for a Gaussian apodised Bragg gratings with and without an XPM shifted Bragg wavelength. The blue line shows the unmodified reflection spectum and the orange line the reflection spectrum with XPM applied. The gratings have parameters $\lambda_B = 1550nm$, $\delta n = 3.3 \times 10^{-6}$ and pump intensity of 1.5 GW/cm^2. Figure (a) has length $L = 0.75$ m and (b) has length $L = 2$ m.

5.2.2 Shifting the band gap edge

One way to reduce the grating length is to relax the requirement that the total band gap be shifted, but instead only shift the edge of the band gap sufficiently to allow a pulse to pass through. In this case, the grating strength can by much stronger. With a stronger grating strength, strong reflectance can be achieved with a shorter grating. Figure 5.6a shows a plot of a grating with a length of 1 cm and a grating strength of $\delta n = 10^{-3}$. The blue line shows the unmodified reflection spectrum and the orange line shows the shifted spectrum by a 2.5×10^9 W/cm^2 intensity pump corresponding to a refractive index change of $\Delta n = 4.3 \times 10^{-6}$.

As can be seen in the figure there is a small shift at the band gap edge. However, as before without an apodisation there is significant sidelobing and so an apodisation is needed. Figure 5.6b shows the same grating but with a Gaussian apodisation with apodisation strength $\alpha_A = 16$. An unfortunate consequence of applying the apodisation is that the decrease in the overall grating strength dramatically decreases the sharpness of the band gap edge over the linewidth of interest. The result is that no transmission band opens up, which can be clearly seen in the figure. The resolution to sharpen the band edge is to again to make the grating longer. To get a clean transmission band from the grating given in figure 5.6b, the grating length has to be increased significantly. Figure 5.7 shows the band edge reflectance for the same grating but with the length increased from 1 cm to 75 cm.

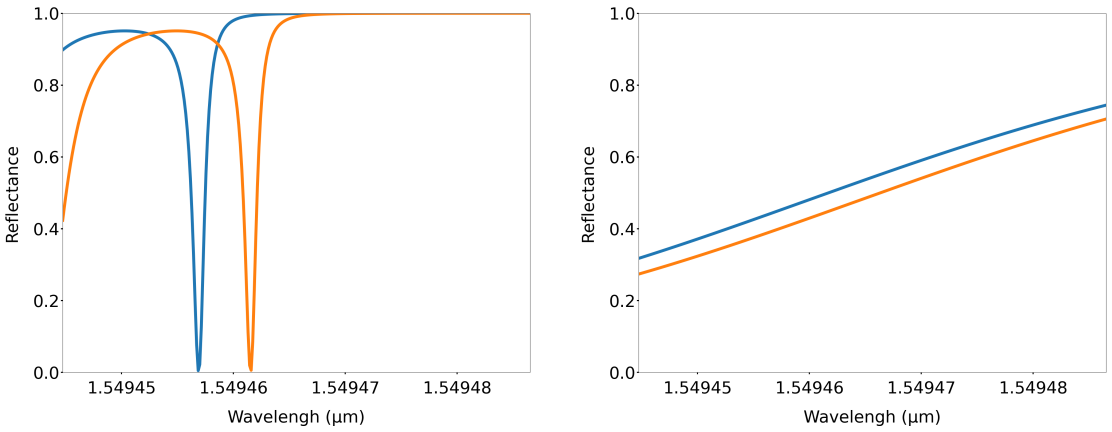

FIGURE 5.6: Plots comparing the reflection spectrums for Bragg gratings with and without an XPM shifted Bragg wavelength. The blue shows the unmodified reflection spectum and the orange line the reflection spectrum with XPM applied. The gratings have parameters $\lambda_B = 1550nm$, $L = 1$ cm, $\delta n = 10^{-3}$ and pump intensity of 1.5 GW/cm^2. Figure (a) has no apodisation and figure (b) has a Gaussian apodisation.

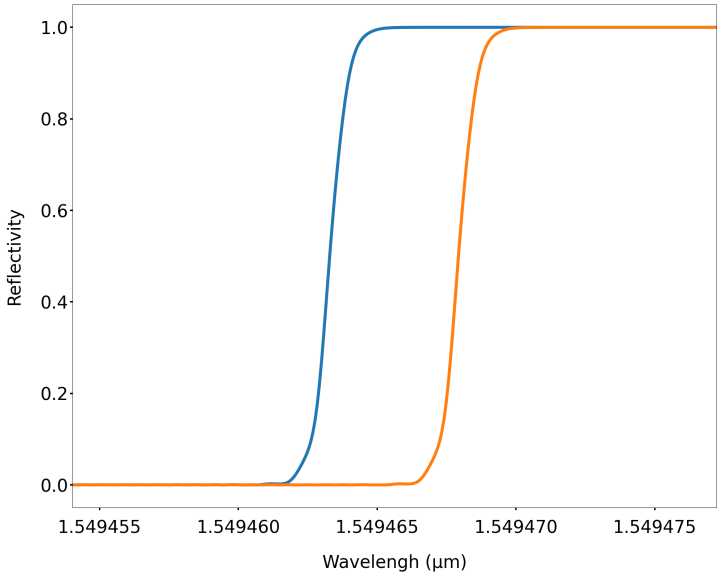

FIGURE 5.7: Figure showing the reflection spectrum for a Bragg grating with a length of 75cm, a Bragg wavelength of $\lambda_B = 1550$ nm, a grating strength of $\delta n = 10^{-3}$ and a Gaussian apodisation profile. The blue line shows the unmodified reflection spectrum. The red line shows the reflection spectrum modified by a 2.5×10^9 W/cm^2 intensity pump.

With the increased grating length, the band edge has become considerably sharper. There is a distinct transmission window that a probe pulse can propagate through. Increasing the grating length from 1 cm to 75 cm is a considerable increase. It is the unfortunate trade off between suppressing the sidelobing and keeping the band edge sharp. As both are needed, a long length grating is required. However, the length is less than what is required to shift the entire band gap as discussed in the previous section.

It is also within the current maximum fabrication length of ultra-long gratings. One drawback to shifting the band edge rather than the full band gap is the increased GVD which was discussed in section 2.2.1. With such a long grating, a probe pulse propagating close to the band edge will cause pulse broadening. This problem increases with the size of the grating strength.

5.2.3 Shifting the moiré transmission band

An alternative to using a Bragg grating is to instead use a moiré grating which was discussed in section 2.2.3 and has grating profile given by (2.87). It differs from a Bragg grating by having a sinusoidal coupling which modifies the steady state coupled mode equations to

$$\partial_z u = i\cos(2\pi z/\Lambda_S)\kappa v e^{-2i\Delta z} + \frac{i\beta_1}{\bar{n}}\Delta n u \tag{5.21}$$

$$\partial_z v = -i\cos(2\pi z/\Lambda_S)\kappa u e^{2i\Delta z} - \frac{i\beta_1}{\bar{n}}\Delta n v. \tag{5.22}$$

The sinusoidal coupling creates a grating with a transmission band between two rejection bands. The centre of the transmission band is located at the Bragg length. Therefore, shifting the Bragg wavelength amounts to shifting the transmission band. If a probe pulse spectrally falls within the transmission band, then if the Bragg wavelength is shifted sufficiently the transmission band can become a rejection band. Then a probe pulse that would initially transmit through the grating would subsequently be reflected. So rather than shifting a band gap to make a transmission band as was the case when using a Bragg grating, the opposite behaviour can be achieved with a moiré grating.

One of the advantages of using the moiré grating is that a stronger grating strength can be used. This is because the transmission band is in general small compared to the rejection bands and so only a small change in the refractive index is necessary to shift it; analogous to shifting the edge of the Bragg band gap. A benefit of using a moiré grating over shifting the Bragg grating band edge is that the transmission band cancel second order dispersion [35] which minimises pulse broadening as discussed in section 2.2.3.

The sinusoidal coupling of a moiré grating is controlled by the moiré period Λ_S. The moiré period has the effect of inserting π phase shifts into the phase of the Bragg grating which opens a transmission window which was discussed in detail in section 4.1.

The shorter the moiré period, the more phase shifts and the wider the resulting transmission band. The other main factor in determining the size of the transmission window is the grating strength. A larger grating strength leads to broadening of the rejection bands and consequently a narrowing of the transmission band. The approximate relationship between the bandwidth of the transmission window and the moiré period and grating strength is given by equation (4.16).

Figure 5.8 shows the transmission band for two moiré gratings with identical parameters except for the grating strength. The blue line shows the transmission band for a grating with $\delta n = 10^{-3}$ and the orange line the transmission band for a grating with grating strength $\delta n = 9 \times 10^{-4}$. The figure shows clearly that the stronger grating strength gives a narrower transmission band.

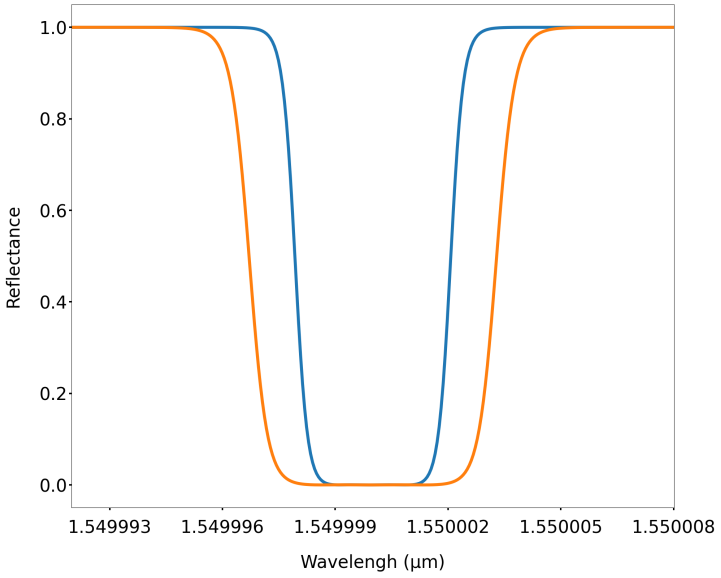

FIGURE 5.8: Figure showing the transmission bandwidth for Moiré grating for different grating strengths. The blue line is for a grating with $\delta n = 10^{-3}$ and the orange line for $\delta n = 9 \times 10^{-4}$. Gratings both have parameters $\lambda_B = 1550$ nm, $L = 10$ cm and a Gaussian apodisation profile

As was seen in the previous section, shorter device lengths are desirable which in turn means using a larger grating strength. Therefore, creating a moiré grating with a transmission bandwidth equal to the shiftable bandwidth given by equation (5.18), should be done by using the highest available grating strength and then adjusting the moiré period to give the desired transmission bandwidth. This will ensure the shortest possible device length.

Figures 5.9a and 5.9b show the shifted transmission band for a moiré grating without and with a Gaussian apodisation respectively and an applied pump intensity of 2.5 GW/cm^2. The device has a length of 10 cm and a moiré period of 8 mm which inserts 25 π phase shifts into the Bragg grating. The transmission bandwidth is approximately 400 MHz and is fully shifted by the pump intensity.

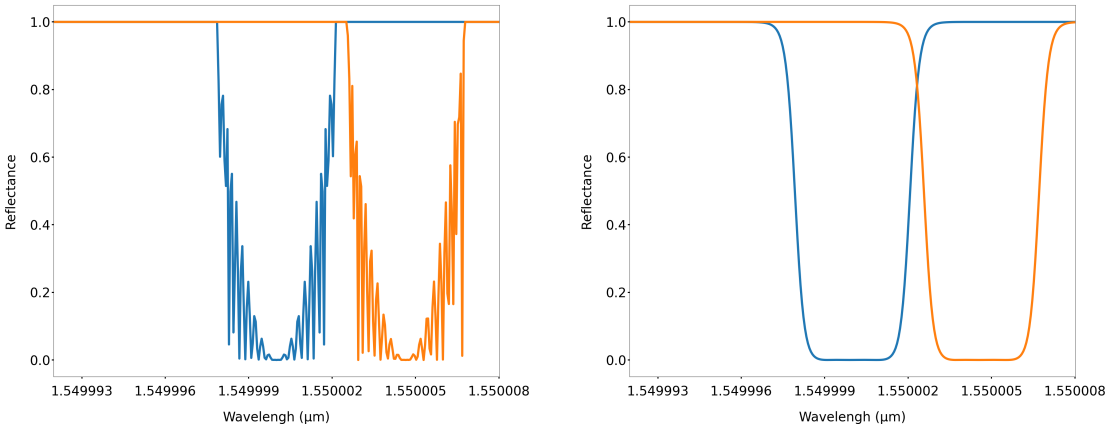

(a) (b)

FIGURE 5.9: Transmission bands for XPM shifted Moiré gratings with (a) no apodisation and (b) a Gaussian apodisation. The blue line shows the unmodified transmission band and the orange line shows the transmission band modified by a 2.5×10^9 W/cm^2 intensity pump. Gratings have a Bragg wavelength $\lambda_B = 1550$ nm, a grating strength of $\delta n = 10^{-3}$ and a length of $L = 10$ cm.

Another benefit of using a moiré grating over a Bragg grating is that applying an apodisation does not lead to the same broadening of the band edge. Applying an apodisation to a moiré grating has little effect of the sharpness of transmission edges which can be seen when comparing figures 5.9a and 5.9b. This provides a distinct advantage over shifting the band edge of a Bragg grating where from the example in the previous section applying an apodisation to suppress the sidelobing required an ultra-long grating to retain a sharp band edge. Therefore, the length of the moiré grating can be kept significantly shorter. The limiting factor in reducing the size of the grating length is the moiré period. A sufficient number of moiré periods are needed to create a clean transmission window and this sets the minimum total length of the grating.

5.3 Simulating pulse propagation

The previous section looked at the steady state requirements for shifting either a Bragg grating band gap or a moiré grating transmission band. This section looks at making the modes time dependent and exploring the behaviour of a probe pulse propagating through bandwidth shifted Bragg and moiré gratings whilst still maintaining an undepleted pump approximation.

5.3.1 Pulse propagation with shifted Bragg gratings

5.3.1.1 Single Bragg gratings

For a single Bragg grating with time dependent modes and where the Bragg wavelength is taken to be the carrier wavelength of the signal so that the detuning is zero, the coupled mode equations become

$$\frac{1}{v_p}\partial_t u + \partial_z u = i\kappa f(z) v + \frac{i\beta_1}{\bar{n}}\Delta n u \tag{5.23}$$

$$\frac{1}{v_p}\partial_t v - \partial_z v = i\kappa f(z) u + \frac{i\beta_1}{\bar{n}}\Delta n v. \tag{5.24}$$

The apodisation function is then given by

$$f(z) = \begin{cases} 0 & z < z_1 \\ \exp\left(-\alpha_A \left(\frac{z-(z_1+L_g/2)}{L_g} \right)^2 \right) & z_1 \leq x \leq z_2 \\ 0 & z > z_2. \end{cases} \tag{5.25}$$

With an undepleted pump approximation applied, Δn is taken to be constant. To demonstrate the band gap shifting, a time-domain simulation is performed using parameters found from the steady state calculations given in figure 5.5b. This gives a two metre Gaussian apodised grating with a band gap bandwidth of approximately 350 MHz. A probe pulse with a FWHM of 135 MHz will spectrally sit inside the band gap bandwidth. The spatial FWHM of the pulse is approximately 2 m.

Figures 5.10a and 5.10b show time-domain simulations for this grating and probe pulse with $\Delta n = 0$. In this case the grating is behaving as a standard Bragg grating and the probe pulse reflects off of the grating as expected.

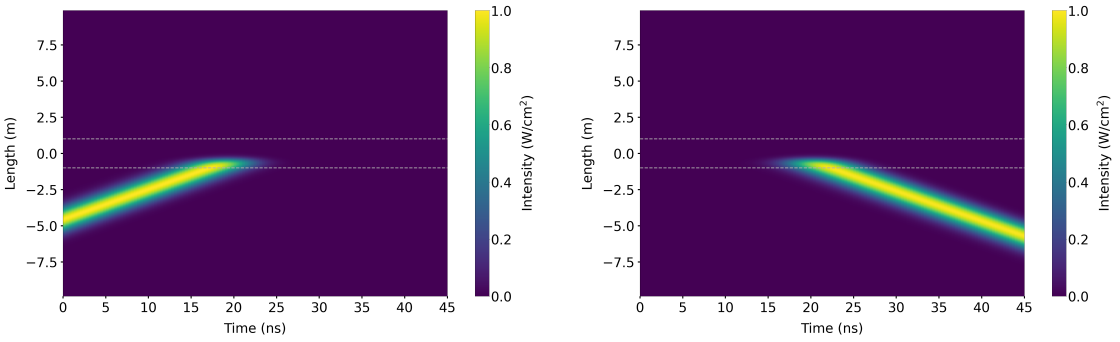

(a) (b)

FIGURE 5.10: Time domain simulation of a Gaussian pulse with a FWHM bandwidth of 135 MHz reflecting from an ultra long Bragg grating with the same parameters as figure 5.5b. Figures (a) and (b) show the forward and backward modes respectively.

To fully shift the band gap, a pump intensity of $1.5\times$ GW/cm^2 is used, which gives a change in the refractive index of $\Delta n = 2.6 \times 10^{-6}$. Figures 5.11a and 5.11b show a simulation of the same grating and probe pulse as in the previous simulation, but with the change of refractive index applied. In this case the probe pulse is able to propagate through the grating with minimal coupling into the backwards mode. This demonstrates that steady-state calculations give a good approximation to the time-dependent behaviour.

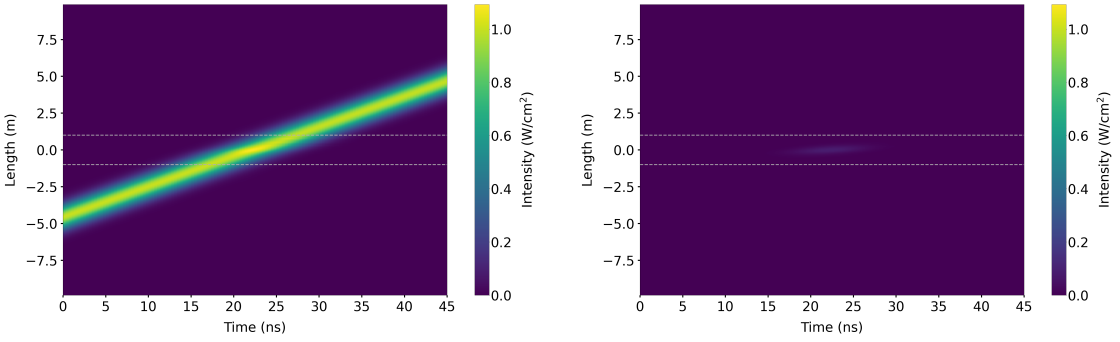

(a) data a (b) data b

FIGURE 5.11: Figure showing the same time domain simulation as figure 5.10 but with an XPM induced refractive index change from a $1.5\times$ GW/cm^2 pump field. Figures (a) and (b) show the forward and backward modes respectively.

5.3.1.2 Two Bragg gratings pulse trap

With the steady-state calculations established as valid for time-domain simulations, two dynamically controlled gratings can be used to create an optical storage device. To do this, the coupled mode equations can be modified to include a time windowing function $g(t)$ to control the refractive index change.

$$\frac{1}{v_p}\partial_t u + \partial_z u = i\kappa f(z)v + \frac{i\beta_1}{\bar{n}}g(t)\Delta n u \tag{5.26}$$

$$\frac{1}{v_p}\partial_t v - \partial_z v = i\kappa f(z)u + \frac{i\beta_1}{\bar{n}}g(t)\Delta n v. \tag{5.27}$$

The windowing function is given by

$$g(t) = \begin{cases} 1 & x < t_s \\ 0 & t_s \leq t \leq t_e \\ 1 & > t_e \end{cases} \tag{5.28}$$

and varies between 0 and 1, which switches the refractive index change Δn off and on. Therefore, the windowing function dynamically controls the shifting of the band gap. The windowing function is initially set to 1 so that the probe pulse can propagate through the first grating and subsequently set to 0 between times t_s and t_e to trap the pulse between the two gratings. When the time is greater than t_e the windowing function is again set to 1 to allow the pulse to be released.

To perform the simulation, the parameters from figure 5.5b are again used with a probe pulse with a bandwidth of FWHM of 135 MHz. Figures 5.12a and 5.12b show the simulation for the forward and backward modes of the probe pulse. With the windowing function initially set to one, the probe pulse can propagate through the first grating. Then as the windowing function switches to zero at time $t_s = 50\,\text{ns}$, the probe becomes resonant with both gratings reflecting off of them. This traps the pulse between the two gratings. When the windowing function is again switched on at time $t_e = 435\,\text{ns}$, the probe pulse can escape through the second grating.

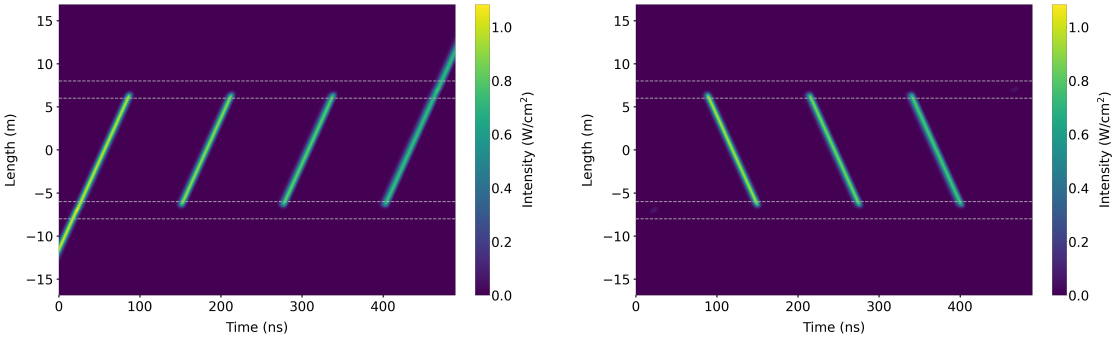

FIGURE 5.12: Time domain simulation of double Bragg gratings with XPM shifted band gaps used to store a probe pulse. The grating and pulse parameters are the same as those in figures 5.5b and 5.10 respectively. Figures (a) and (b) show the forward and backward modes respectively.

The successive reflections off of the grating cause the pulse to distort. This is due to the length of the grating and the apodisation. The apodisation means that the grating strength increases toward the centre of the grating. Therefore, the pulse is able to penetrate further into the grating than if there was no apodisation. For a short length grating this ordinarily would not be a problem, but due to the long length of the grating in the simulation, the pulse penetration into the grating causes dispersion and broadening effects. This can be seen in figures 5.12a and 5.12b as the intensity of the pulse reduces after each reflection. To show this more explicitly, figures 5.13a and 5.13b show the pulse before and after entering the device respectively. Figure 5.13b clearly shows the broadening of the pulse. As the problem is due to the length of the grating, a shorter grating would resolve the issue. However, as previously discussed, shorter gratings require stronger grating strengths which in turn mean only the band gap edge can be shifted. This introduces its own dispersion and so in either case the device will generate pulse broadening.

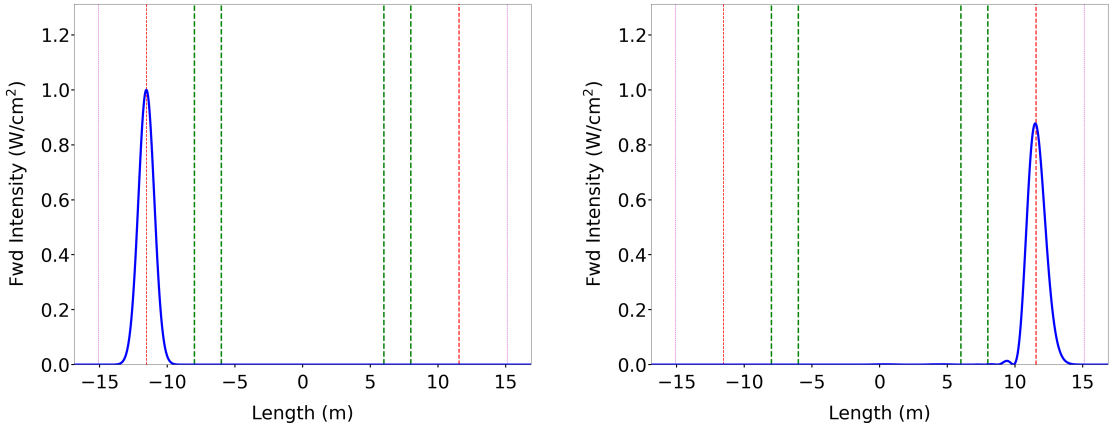

FIGURE 5.13: Figures (a) and (b) showing the before and after pulse profiles respectively for the time domain simulation from figure 5.12.

5.3.2 Pulse propagation with shifted moiré gratings

This section looks at time domain pulse propagation through a moiré grating. First, a single grating is considered and then two gratings to create a pulse trap.

5.3.2.1 Single moiré grating

To include the moiré grating in the time domain simulation the moiré envelope needs to be added to the coupled mode equations which gives

$$\frac{1}{v_p}\partial_t u + \partial_z u = i\cos(2\pi z/\Lambda_S)\kappa f(z)v + \frac{i\beta_1}{\bar{n}}\Delta n u \tag{5.29}$$

$$\frac{1}{v_p}\partial_t v - \partial_z v = i\cos(2\pi z/\Lambda_S)\kappa f(z)u + \frac{i\beta_1}{\bar{n}}\Delta n v. \tag{5.30}$$

The position of the grating can be controlled in the same way as was done with a single Bragg grating using the apodisation function (5.25). However, the change in the refractive index has the opposite effect to what it had with a Bragg grating. With no change in the refractive index the probe pulse is able to propagate through the moiré transmission band and with a refractive index change applied, the transmission band is shifted and the pulse is reflected from the grating.

The moiré grating in figure 5.9b is a 10 cm grating with a with a transmission bandwidth of approximately 500 MHz. A probe pulse that has a FWHM bandwidth of this size will have spatial length that is long compared to the length of the grating. The large difference in sizes is problematic from a simulation perspective as the grid resolution needs to be small enough to resolve the moiré period. Resolving the pulse length at such a small resolution become computationally expensive. Two different mesh sizes could be used inside and outside the grating, but the small comparative size of the grating also means that it is more difficult to see the features of the grating. Therefore, for demonstration purposes, we take a grating with the same parameters as those in figure 5.9b, but decrease the moiré period to 5 mm. This increases the size of the transmission band and therefore the available bandwidth for the probe pulse. This in turn means a spatially shorter probe pulse which is more amenable for using in a simulation. The increased size of the transmission band means a larger change in the refractive index is required to fully shift the refractive index. For this particular grating, the required refractive index change is $\Delta n = 4.4 \times 10^{-5}$, which would correspond to a pump pulse of 25 GW/cm^2 which is beyond the damage threshold for a silica fibre. The transmission band for this grating is large enough to fit a probe pulse with a FWHM bandwidth of 3 GHz.

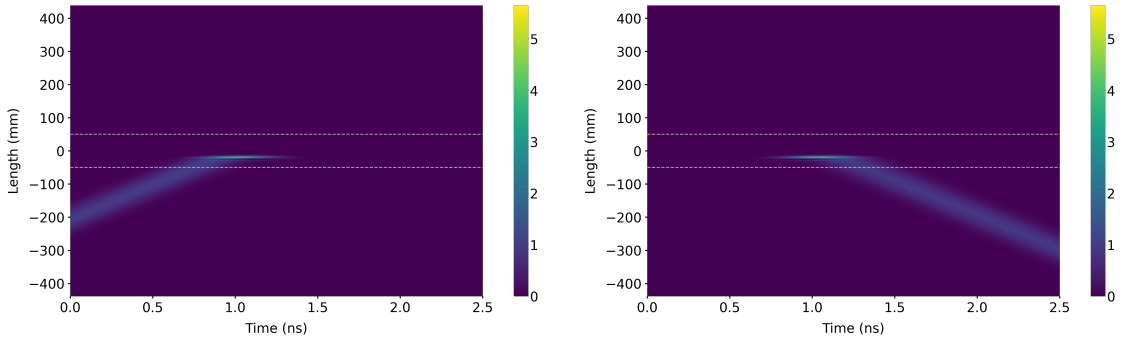

(a) (b)

FIGURE 5.14: Time domain simulation of a probe pulse reflecting from a moiré grating with a refractive index change of $\Delta n = 4.4 \times 10^{-5}$. The grating has parameters $\lambda_B = 1550\,\text{nm}$, $\Lambda_S = 5\,\text{mm}$, $\delta n = 10^{-3}$ and a grating length of $L = 10\,\text{cm}$. The probe pulse is a Gaussian pulse with a FHWM bandwidth of 3 GHz

Figures 5.14a and 5.14b show the forward and backward modes for the probe pulse propagating through the moiré grating with the change in refractive index applied. This causes the transmission band to shift so that the probe pulse falls within a rejection band and so is reflected by the grating. From the figure it can be seen that the pulse is able to penetrate relatively deeply into the grating before being reflected.

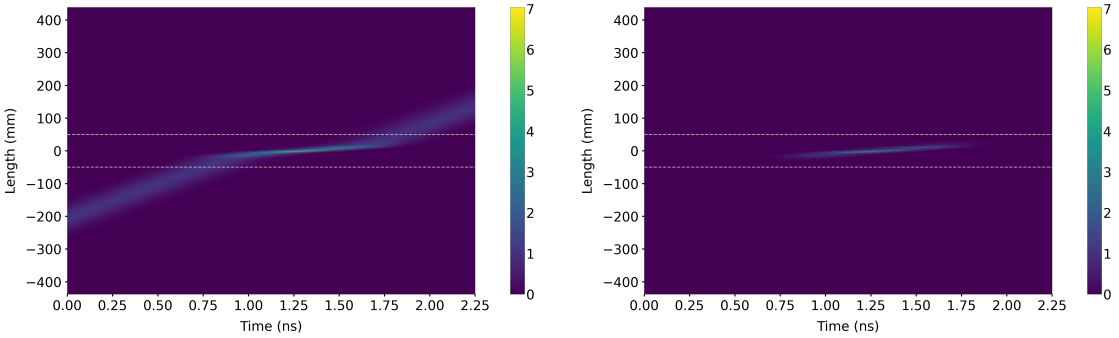

(a) (b)

FIGURE 5.15: Figure showing the time domain simulation of a probe pulse transmitting though a moiré grating. Grating and pulse have the same parameters as in figure 5.14

Figures 5.15a and 5.15b show the forward and backward modes for the probe pulse propagating through the moiré grating without the change in refractive index applied. The probe is then resonant with the transmission band and is able to pass through the grating. The slow light nature of the grating is clear as the pulse is propagating slower through the grating then outside which is in contrast to the behaviour seen in the Bragg grating in figure 5.11 where the group velocity of the pulse remains roughly constant. The increase in intensity of the probe pulse due to slow slight is also clearly visible. And so, just as we saw with the Bragg grating, the moiré grating can be used as a gate to reflect or allow a probe pulse through by inducing a change in the Bragg wavelength.

5.3.2.2 Two moiré grating trap

Now we look at using the moiré grating to create an optical storage device by having two separated moiré gratings and dynamically shifting the transmission bands. Again, the coupled mode equations have to be modified to include a time windowing function $g(t)$ which is given by equation (5.28). The coupled mode equations then become

$$\frac{1}{v_p}\partial_t u + \partial_z u = i\cos(2\pi z/\Lambda_S)\kappa f(z)v + \frac{i\beta_1}{\bar{n}}g(t)\Delta n u \tag{5.31}$$

$$\frac{1}{v_p}\partial_t v - \partial_z v = i\cos(2\pi z/\Lambda_S)\kappa f(z)u + \frac{i\beta_1}{\bar{n}}g(t)\Delta n v. \tag{5.32}$$

The storage device is simulated using the same moiré grating as in the previous section, which had a 10 cm length, a 5 mm moiré period and Gaussian apodisation profile. The probe pulse is a Guassian pulse with a FWHM bandwidth of 3 GHz and a spatial FWHM of approximately 85 mm. Figures 5.16a and 5.16b show the forward and backwards modes of the simulation.

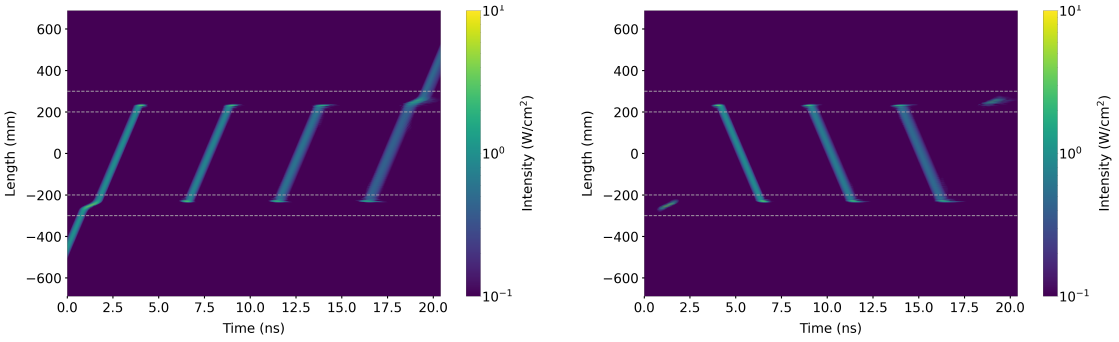

(a) (b)

FIGURE 5.16: Time domain simulation of double moiré gratings with XPM shifted tranmission bands used to store a probe pulse. The grating and pulse parameters are the same as those in figure 5.14. Figures (a) and (b) show the forward and backward modes respectively.

The simulation starts at $t_0 = 0$, from which the probe pulse propagates towards the first grating. The windowing function $g(t)$ is initially set to 0, so that the pulse can propagate though the transmission band. Then at time $t_1 = 3\,\text{ns}$, $g(t)$ is set to 1 which shifts the Bragg wavelength of the gratings closing the transmission bands for the probe pulse. The pulse is then trapped between the two gratings. At time $t_2 = 18\,\text{ns}$, $g(t)$ is set to 0, opening the transmission bands again. The pulse is then able to escape out of the second grating. While again this demonstrates that moiré gratings can be used to create an effective optical storage device, the successive reflections lead to pulse distortions just as in the case where Bragg gratings were used.

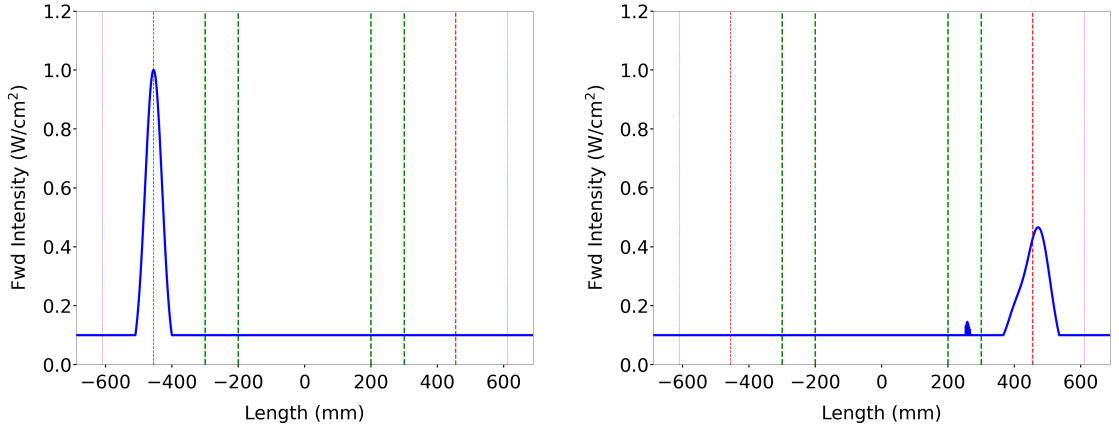

(a) (b)

FIGURE 5.17: Figures (a) and (b) showing the before and after pulse profiles respectively for the time domain simulation from figure 5.16.

Figures 5.17a and 5.17b show the probe pulse before and after the device. As the pulse is able to penetrate some way into the grating, it experiences uneven dispersion along its length which causes pulse broadening. However, in comparison with the before and after pulse profiles using Bragg gratings given in figures 5.13a and 5.13b, the broadening due to the moiré grating is more significant. This may be somewhat of a surprise, as in the case of the Bragg grating, the broadening was due to the long grating length and the apodisation. As the moiré grating is shorter, it might be expected that this problem would be reduced. However, even though over the full length of the grating the reflectance is high, the oscillating moiré term allows the probe field to penetrate deeper into the grating than the Bragg grating causing worse pulse distortion.

5.3.3 Including self phase modulation

Throughout this chapter, the change in refractive index has been taken to be due to XPM from a strong pump pulse. The motivation for this was that using all-optical switching would allow for switching times down in the range of nanoseconds. Combined with a low loss silica fibre this would enable a quick and efficient optical storage device. However, the discussion has been kept general so that the results can also be applied to other methods for inducing a refractive index change.

In order for the pump to work effectively at changing the refractive index and shifting the Bragg wavelength, it must change the refractive uniformly across the entirety of the grating. Furthermore, it must also do this for the duration of the probe pulse propagating through the grating. This is problematic, as the grating lengths must be substantial in order to have high enough reflectance to effectively trap a pulse. In the case of the Bragg grating, ultra-long gratings at the edge of current technological limits are required. The situation is somewhat better when a moiré grating is used and a grating length in region of 10 cm is sufficient. However, in both cases, the bandwidth available for the probe pulse is on the order of hundreds of MHz and therefore the spatial profile of the probe is meters long. The pump pulse will therefore at a minimum have to have a spatial length as long as the probe pulse in order to uniformly change the refractive index.

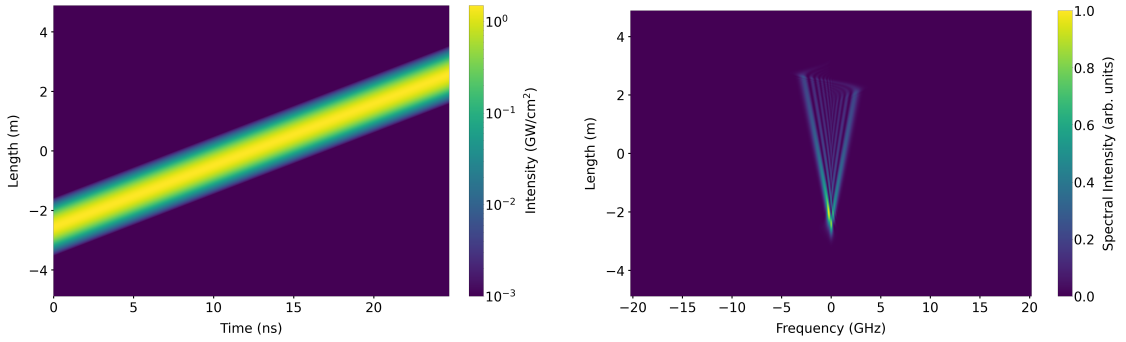

(a) (b)

FIGURE 5.18: a Time domain simulation of Gaussian pulse propagation and b pulse spectrum showing effects of SPM. With parameters FWHM = 3 GHz and a pump intensity of 1.5 GW/cm^2.

Figure 5.18 shows a simulation of equation (5.11) for a Gaussian pump pulse with intensity 1.5 GW/cm^2. The FWHM bandwidth of the pump is 3 GHz which is the same bandwidth used for the probe pulse in figure 5.17. Figure 5.18b shows the effect of the self-phase modulation on the pulse spectrum. As the figure clearly shows, the self-phase modulation causes spectral broadening which in a dispersive medium would cause a change in the spatial shape of the pulse. A potential way to mitigate this problem is to use a super-Gaussian pulse of the form

$$p(x) = A \exp\left(- \left(\frac{(z - z_0)^2}{2\sigma} \right)^m \right). \tag{5.33}$$

Raising the content of the exponent to a power of m has the effect of flattening the Gaussian creating a so called flat-top pulse. Here the super-Gaussian serves a dual purpose. Firstly, with a flat-top profile the maximum intensity of the pulse covers a larger spatial width, which can be seen in figure 5.19a which shows the propagation of a super-Gaussian pulse. The refractive index needs to be uniformly changed along the length of the grating, a flat-top profile with a spatially broader maximum intensity is better suited to this task.

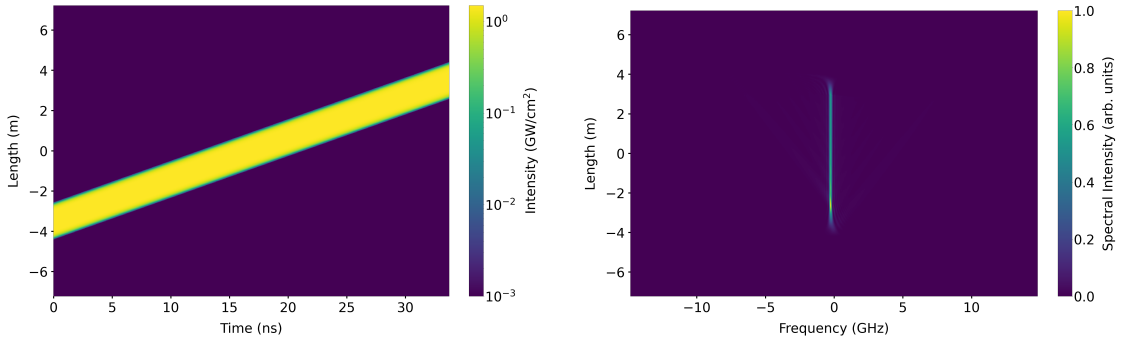

(a) (b)

FIGURE 5.19: a Time domain simulation of super-Gaussian pulse propagation and b pulse spectrum showing effects of SPM. With parameters Guassian FWHM = 3 GHz, super-Gaussian exponent $m = 5$ and a pump intensity of 1.5 GW/cm^2.

The second benefit is that the induced SPM of a super-Guassian pulse is reduced compared to a Gaussian. This can be seen by comparing the figures 5.18b and 5.19b which show the spectrum of a propagating Gaussian pulse and a super-Gaussian pulse respectively. The benefit of this is that there will be less distortion to the spatial pulse shape.

5.4 Summary

In this chapter we have looked at creating an optical storage device using Bragg and moiré gratings. The principal idea behind the device is to induce a change in the DC refractive index component of the grating. This has the effect of altering the Bragg wavelength, creating a tuneable rejection or transmission band. By using two gratings and dynamically controlling the Bragg wavelength, a probe pulse can be trapped between the gratings and subsequently released. Two grating types were looked at for the device. A standard Bragg grating, where shifting the Bragg wavelength shifts the rejection band, and a moiré grating where shifting the Bragg wavelength shifts the transmission band. First the gratings were looked at under steady-state conditions and then subsequently were looked at dynamically.

The motivation for a device of this type is to create a delay line which would have switching times on the order of nanoseconds with low loss. This would be achieved by fabricating the device in a silica fibre and inducing a refractive index change using a strong pump pulse and XPM.

This chapter has shown that there are two fundamental problems with this approach. Firstly, the small refractive index change that can be induced using XPM limits the available bandwidth of the pulse which means that long grating lengths are required. In the case the of Bragg gratings, ultra-long gratings are needed. Shorter grating lengths

can be used with a moiré grating but in both cases the probe pulse can penetrate deeply enough into the gratings to produce pulse distortions. Therefore, each successive reflection within the device leads to greater pulse distortions.

Chapter 6

Slow light enhanced second-harmonic generation

This chapter is based on my paper published in physical review A [83]. It looks at the application of slow light gratings for the enhancement of second-harmonic generation. It was shown in section 4.3 that a pulse entering a slow light grating experiences pulse compression due to the difference in group velocity inside and outside the grating. As a consequence, conservation of energy requires that pulse compression is accompanied by field enhancement. This is another useful property of slow light gratings that can be exploited to enhance nonlinear processes. For any given medium, the nonlinear susceptibilities are many orders of magnitude weaker than the linear susceptibility. As a consequence, in order to achieve efficient nonlinear processes, high intensities are necessary to compensate for the relative weakness of the nonlinear susceptibilities. Therefore, using a slow light grating for intensity enhancement offers the possibility of enhancing nonlinear processes [35, 84].

Second-harmonic generation was introduced in section 2.3. Along with being an intensity dependent process, second-harmonic generation also requires phase matching between the fundamental and second-harmonic. Typically, material dispersion causes dephasing between the two modes and it is necessary to deploy a phase matching scheme. The method of principle interest in this chapter is quasi-phase matching via periodic poling [45].

The idea of using field enhancement to improve conversion efficiency in second-harmonic generation has been looked at before. Perhaps the simplest approach is to enclose a nonlinear crystal within a Fabry–Perot cavity which is resonant with either the fundamental or second-harmonic mode [85]. This method was shown to give an enhancement of 13% [86]. The cavity causes the resonant mode to circulate increasing its intensity and enhancing the second-harmonic generation. Similar ideas have been proposed

using periodic polling by phase matching counter propagating modes [87, 88] which exhibits the same recirculation and enhancement behaviour.

To achieve slow light grating enhancement of second-harmonic generation in a periodically poled medium, it is necessary to have not only the $\chi^{(2)}$ poled grating, but also a linear grating. There have been some theoretical studies on the inclusion of a linear grating in a $\chi^{(2)}$ medium and its effect on harmonic generation [89, 90]. However, it has been problematic to write linear gratings in bulk $\chi^{(2)}$ media with any appreciable index contrast [91, 92]. In recent years there has been progress in producing high index contrast linear gratings in thin-film lithium niobate [93]. This research has been extended to also include demonstrations of π phase shift gratings in thin-film lithium niobate [94, 95]. Therefore, in the near future it may be possible to fabricate devices that incorporate both periodic poling and slow light gratings for enhancing $\chi^{(2)}$ processes.

This chapter examines the continuous wave enhancement of second-harmonic generation by incorporating a slow light π phase shifted grating in a periodically poled $\chi^{(2)}$ medium. The coupling between the fundamental forward and backward modes in a slow light grating causes generation of corresponding forward and backward second-harmonic modes. To suppress the backward second-harmonic, a short Bragg grating is also incorporated into the front of the device to ensure unidirectional forward propagating output of the second-harmonic. It is then shown that by optimising the free parameters of the device, it is possible to achieve significant enhancement in second-harmonic generation when compared to a device with only periodic poling.

6.1 Theoretical Model

6.1.1 Grating profiles

The theoretical device under consideration in this chapter is a periodically poled $\chi^{(2)}$ nonlinear crystal with two linear gratings. It will be shown that carefully engineering the properties of the two linear gratings can lead to a significant enhancement in second-harmonic generation. The starting point for the device is a linear grating profile which has the following form

$$n(x) = \bar{n} + \delta n\Big(f_1(x)a_1(x)a_s(x) + f_2(x)a_2(x)\Big). \tag{6.1}$$

The effective index is given by $\bar{n}$ and the grating strength by δ_n. Then the terms $f_1(x)a_1(x)a_s(x)$ correspond to a superstructure slow light grating and the $f_2(x)a_2(x)$ to a short reflection grating at the start of the device. It is common notation for crystallographers to refer to the propagation direction as x rather than z and so that convention

is adopted for this chapter. Figure 6.1 provides a schematic illustrating the two linear gratings.

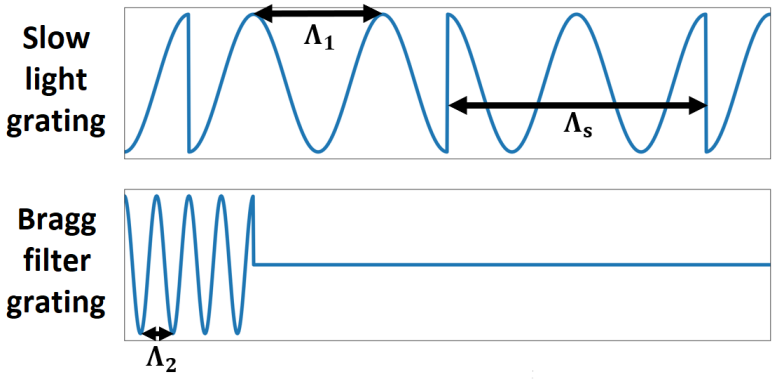

FIGURE 6.1: Schematic of the two linear gratings: a slow light π phase shifted grating with Bragg period Λ_1 and superstructure period Λ_S, and a reflection Bragg grating with period Λ_2 at the input end of the device.

The slow light grating is composed of three terms, an apodisation function $f_1(x)$, a Bragg envelope $a_1(x)$ and a superstructure envelope $a_s(x)$. In the subsequent analysis, the apodisation function is chosen to have a Gaussian profile given by equation 2.85 with an apodisation strength $\alpha_A = 16$. The Bragg and superstructure envelopes take the forms

$$a_1(x) = \cos\left(\frac{2\pi x}{\Lambda_1} + \phi_1\right), \tag{6.2}$$

$$a_s(x) = \text{sgn}\left[\cos\left(\frac{\pi(2x - L)}{\Lambda_S} + \frac{\pi}{2}\right)\right], \tag{6.3}$$

The Bragg envelope has an arbitrary phase constant ϕ_1 and a Bragg period given by $\Lambda_1 = \lambda_1/(2\bar{n}_1)$. This provides a Bragg resonance at λ_1 which is the wavelength of the fundamental mode and where $\bar{n}_1$ is the corresponding effective refractive index. The superstructure envelope produces a π phase shifted grating opening a transmission band at the centre of the Bragg resonance. A constant phase $\phi_s = \pi(1/2 - L/\Lambda_S)$ has been added to the superstructure envelope which ensures for a device of length L, there is a π phase shift at the centre of the device. The purpose of the superstructure grating is to turn the fundamental mode into a slow light wave. The reduction in group velocity will be accompanied by an increase in field enhancement which will improve the conversion efficiency to the second-harmonic.

As previously discussed in section 2.2.3, the superstructure grating will generate both forward and backward second-harmonic modes, and so a short reflection grating is placed at the start of the device to suppress the backwards mode. The reflection grating

is composed of two terms, an apodisation function $f_2(x)$ and a Bragg envelop $a_2(x)$. The latter is given by

$$a_2(x) = \cos\left(\frac{2\pi x}{\Lambda_2} + \phi_2\right), \tag{6.4}$$

where ϕ_2 is a constant phase term. The Bragg period $\Lambda_2 = \lambda_2/(2\bar{n}_2)$ creates a Bragg resonance at the second-harmonic wavelength λ_2 with a corresponding effective refractive index $\bar{n}_2$. The apodisation functions are constrained such that $f_1(x) + f_2(x) \leq 1$. As the apodisation functions effectively scale the grating strength, the constraint ensures that the overall magnitude of grating modulation does not exceed the maximum δn that can be fabricated. Therefore, the reflection grating apodisation is defined by

$$f_2(x) = \begin{cases} 1 - f_1(x) & \text{if} \quad 0 \leq x \leq L_R \\ 0 & \text{if} \quad x > L_R \end{cases} \tag{6.5}$$

where L_R is the length of the reflection grating. For lengths less than L_R the reflection apodisation is simply the magnitude of δn remaining from the superstructure apodisation. For lengths greater than L_R, the apodisation is set to zero so that the reflection grating only occupies the start for the device. Figure 6.2 gives an example of the apodisation profiles for the slow light and reflection gratings.

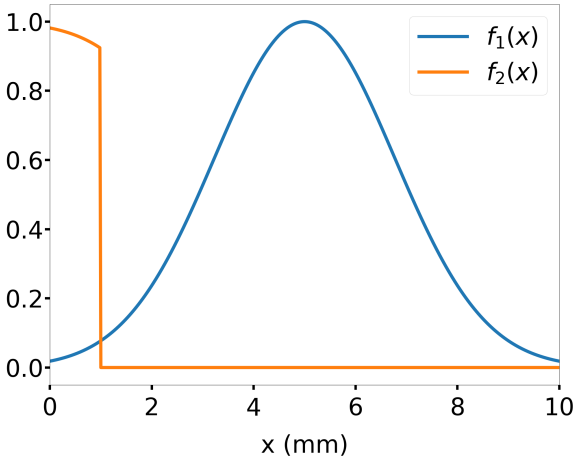

FIGURE 6.2: Slow light grating apodization f_1 and reflection grating profile f_2 with parameters $L = 10$ mm, $\alpha_A = 16$ and $L_R = 1$ mm.

The recent developments in fabricating linear gratings in thin-film lithium niobate [93, 94, 95] make it the natural choice for a potential device. Therefore, throughout this chapter the device medium is taken to be thin-film lithium niobate doped with magnesium oxide (MgO:$LiNbO_3$), which has an increased optical damage threshold [96] compared to lithium niobate. $\chi^{(2)}$ will then refer to the highest nonlinear tensor component for MgO:$LiNbO_3$ which is $d_{33} = 25\,\text{pm/V}$ at a wavelength of 1064 nm. The

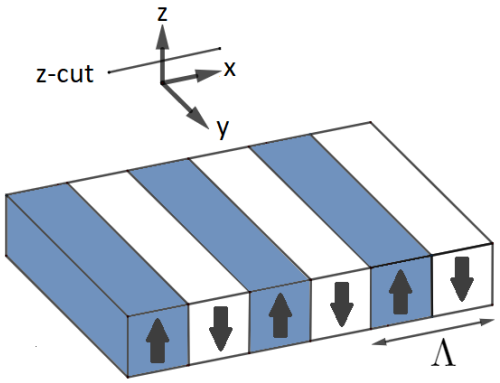

FIGURE 6.3: Schematic of a periodically poled $\chi^{(2)}$ medium showing the poling period Λ.

d_{33} component is accessed by waves polarized vertically along the z-axis. Figure 6.3 shows a schematic of periodically poled z-cut crystal which takes advantage of the d_{33} component.

6.1.2 Coupled mode equations in a $\chi^{(2)}$ medium

In this section the coupled mode equations are derived for the device described in the previous section using the variational techniques introduced in chapter 3.1. The starting point is to define the following vector potential ansatz

$$\begin{aligned} A = &-\frac{i}{\omega_1}u_1(t,x)e^{i(\beta_1 x-\omega_1 t)} - \frac{i}{\omega_1}v_1(t,x)e^{-i(\beta_1 x+\omega_1 t)} \\ &-\frac{i}{\omega_2}u_2(t,x)e^{i(\beta_2 x-\omega_2 t)} - \frac{i}{\omega_2}v_2(t,x)e^{-i(\beta_2 x+\omega_2 t)} + c.c. \end{aligned} \tag{6.6}$$

where u_1 and v_1 are the fundamental forward and backward modes with frequency and propagation constant ω_1 and β_1 respectively. The second-harmonic forward and backward modes are denoted by u_2 and v_2 with frequency and propagation constant ω_2 and β_2 respectively. To develop the coupled mode equations, the ansatz (6.6) and the refractive index profile (6.1) need to be substituted into the nonlinear electromagnetic Lagrangian

$$\mathcal{L} = \frac{\epsilon_0}{2}n^2(\partial_t A)^2 - \frac{1}{2\mu_0}(\partial_x A)^2 - \frac{\epsilon_0}{3}\chi^{(2)}(x)(\partial_t A)^3, \tag{6.7}$$

which is written in the Weyl gauge and where $\chi^{(2)}$ has been made position dependent to take into account the periodic poling. After making rotating wave, slowly varying envelope and neglecting small term approximations the Lagrangian splits into three

terms $\mathcal{L}_{lin1}$, $\mathcal{L}_{lin2}$ and $\mathcal{L}_{nlin}$. The first term $\mathcal{L}_{lin1}$ contains all the linear terms for the fundamental modes

$$\begin{aligned}\mathcal{L}_{lin1} = &\frac{i\epsilon_0\bar{n}_1^2}{\omega_1}\left(u_1^*\partial_t u_1 - u_1\partial_t u_1^* + v_1^*\partial_t v_1 - v_1\partial_t v_1^*\right)\\ &+\frac{i\epsilon_0 c^2\beta_1}{\omega_1^2}\left(u_1^*\partial_z u_1 - u_1\partial_z u_1^* + v_1^*\partial_z v_1 - v_1\partial_z v_1^*\right)\\ &+\epsilon_0\bar{n}_1 f_1 a_s\delta n\left(v_1^* u_1\, e^{i\phi_1}e^{2i\Delta_1 z} + u_1^* v\, e^{-i\phi_1}e^{-2i\Delta_1 z}\right).\end{aligned} \tag{6.8}$$

Similarly, the second term $\mathcal{L}_{lin2}$ contains all the linear terms for the second-harmonic modes

$$\begin{aligned}\mathcal{L}_{lin2} = &\frac{i\epsilon_0\bar{n}_2^2}{\omega_2}\left(u_2^*\partial_t u_2 - u_2\partial_t u_2^* + v_2^*\partial_t v_2 - v_2\partial_t v_2^*\right)\\ &+\frac{i\epsilon_0 c^2\beta_2}{\omega_2^2}\left(u_2^*\partial_z u_2 - u_2\partial_z u_2^* + v_2^*\partial_z v_2 - v_2\partial_z v_2^*\right)\\ &+\epsilon_0\bar{n}_2 f_2\delta n\left(v_2^* u_2\, e^{i\phi_2}e^{2i\Delta_2 z} + u_2^* v\, e^{-i\phi_2}e^{-2i\Delta_2 z}\right).\end{aligned} \tag{6.9}$$

The third term $\mathcal{L}_{nlin}$ contains the coupling terms between the fundamental and the second-harmonic modes

$$\mathcal{L}_{nlin} = -\epsilon_0\chi^{(2)}(x)\left(u_2(u_1^*)^2e^{i\Delta_\beta x} + u_2^*u_1^2e^{-i\Delta_\beta x} + v_2(v_1^*)^2e^{-i\Delta_\beta x} + v_2^*v_1^2e^{i\Delta_\beta x}\right). \tag{6.10}$$

To incorporate the poling into equations (6.10), the poling function given by equation (2.101) can be substituted for $\chi^{(2)}(x)$ which gives

$$\mathcal{L}_{nlin} = \frac{2i\epsilon_0\chi^{(2)}}{\pi}\left(u_2(u_1^*)^2 + v_2^*v_1^2 - u_2^*u_1^2 - v_2(v_1^*)^2\right). \tag{6.11}$$

The total Lagrangian is then given by the sum of its linear and nonlinear parts

$$\mathcal{L} = \mathcal{L}_{lin1} + \mathcal{L}_{lin2} + \mathcal{L}_{nlinp}. \tag{6.12}$$

Then the coupled mode equations follow in the usual way from varying the Lagrangian with respect to modes u_1, v_1, u_2 and v_2,

$$\frac{\partial u_1}{\partial x} = ie^{i\phi_1}\kappa_1(x)v_1 + \frac{\kappa_3}{\bar{n}_1}u_1^*u_2 \tag{6.13}$$

$$\frac{\partial v_1}{\partial x} = -ie^{-i\phi_1}\kappa_1(x)u_1 + \frac{\kappa_3}{\bar{n}_1}v_1^* v_2 \tag{6.14}$$

$$\frac{\partial u_2}{\partial x} = ie^{i\phi_2}\kappa_2(x)v_2 - \frac{\kappa_3}{\bar{n}_2}u_1^2 \tag{6.15}$$

$$\frac{\partial v_2}{\partial x} = -ie^{-i\phi_2}\kappa_2(x)u_2 - \frac{\kappa_3}{\bar{n}_2}v_1^2 \tag{6.16}$$

where the coupling coefficients are given by

$$\kappa_1(x) = \frac{\pi\delta n}{\lambda_1}f_1(x)a_s(x) \tag{6.17}$$

$$\kappa_2(x) = \frac{2\pi\delta n}{\lambda_1}f_2(x) \tag{6.18}$$

$$\kappa_3 = \frac{4\chi^{(2)}}{\lambda_1}. \tag{6.19}$$

6.1.3 Numerical methods

Solving the coupled mode equations (6.13-6.16) presents a challenge. The equations form a boundary value problem with only partially known boundary conditions. In total there are 8 complex (16 real) boundary conditions. There are two known boundary conditions at both the start and the end of the device, which leaves another 4 undetermined. The known boundary conditions at the start of the device are the input amplitudes for the two forward modes. The fundamental forward mode has an initial arbitrary amplitude A and so provides the boundary condition $u_1(0) = A$. The forward second-harmonic mode is initially zero and so $u_2(0) = 0$. At the end of the device the backward modes must satisfy the boundary conditions $v_1(L) = 0$ and $v_2(L) = 0$, which ensures no light is coupled into the device from the end. That leaves the boundary conditions for the two backwards at the start of the device, and the two forward modes and end of the device unknown.

There are standard integration libraries which provide boundary solvers such as numpy's solve_bvp [97] which can solve such boundary value problems. However, the nonlinear nature of equations (6.13-6.16) means that finding solutions is strongly dependent on the choice of initial conditions. This becomes increasing true as the input intensity of the forward fundamental mode is increased, at which point standard solving packages fail to find physically meaningful solutions. It is therefore necessary to develop

a boundary solver from first principles that incrementally adjusts the initial boundary condition to produce correct solutions. A general shooting method for this purpose is described in detail by Ja [98]. The first step is to express as vectors the modes

$$\boldsymbol{y}(z) = [u_1(z), u_2(z), v_1(z), v_2(x)], \tag{6.20}$$

and unknown boundary conditions

$$\boldsymbol{p}(x) = [v_1(0), v_2(0), u_1(L), u_2(L)]. \tag{6.21}$$

Next, an initial guess needs to be made for the unknown boundary conditions $\boldsymbol{p}$. This also make the modes $\boldsymbol{y}(z, \boldsymbol{p})$ a function of $\boldsymbol{p}$. With the initial guess, equations (6.13-6.16) are integrated forward from the start of the device giving the solution $\boldsymbol{y}_f(x, \boldsymbol{p})$. Then similarly the equations are integrated backwards from the end of the device to give the solution $\boldsymbol{y}_b(z, \boldsymbol{p})$. Then for some arbitrary point $x = m$, the correct initial conditions satisfy

$$\boldsymbol{g}(\boldsymbol{p}) = \boldsymbol{y}_f(m, \boldsymbol{p}) - \boldsymbol{y}_b(m, \boldsymbol{p}) = \boldsymbol{0}. \tag{6.22}$$

It is usually beneficial to choose m so that it either corresponds to the start of the device $m = 0$, or the end of the device $m = L$. Then only a forward or backward integration is necessary. Finding the correct initial conditions then reduces to the problem of minimising $\boldsymbol{y}_f(m, \boldsymbol{p}) - \boldsymbol{y}_b(m, \boldsymbol{p})$. While there exist numerous approaches to solving equation (6.22), the approach used in the subsequent analysis is to define the quantity

$$\mathcal{L} = \sum_i |g_i(p_i)|^2 \tag{6.23}$$

which produces a positive real number which can the be minimised to zero using the Nelder–Mead method [99]. The benefit of this method is that it does not require calculating the Jacobian of $\boldsymbol{g}(\boldsymbol{p})$ and therefore its derivatives with respect to $\boldsymbol{p}$.

The process of finding the initial boundary conditions $\boldsymbol{p}$ at a high input intensity, is to first find the boundary conditions for the same device starting with a negligible input intensity. If the input intensity is sufficiently small than equations (6.13-6.16) effectively become a π phase shifted grating to which the exact boundary conditions can be found. Then, to find the solution at a higher input intensity, the initial intensity can be increased incrementally by using the boundary conditions found at the previous increment. This is repeated recursively until the solution for the desired input intensity is a found.

6.2 Group velocity and field enhancement

If the grating strength δn is kept constant, then the key parameter affecting the slow light produced by the superstructure grating is the superstructure period Λ_S. Larger values Λ_S produce lower group velocities and conversely, smaller values of Λ_S produce higher group velocities. As was discussed in section 4.3, a pulse entering a slow light grating will be compressed by a factor v_g/v_0 where v_g and v_0 are the group velocities inside and outside the grating respectively. Consequently, the amplitude of the electric field will increase by the inverse factor v_0/v_g. Figure 6.4 shows how the group velocity induced field enhancement calculated using equation (3.78) varies with Λ_S.

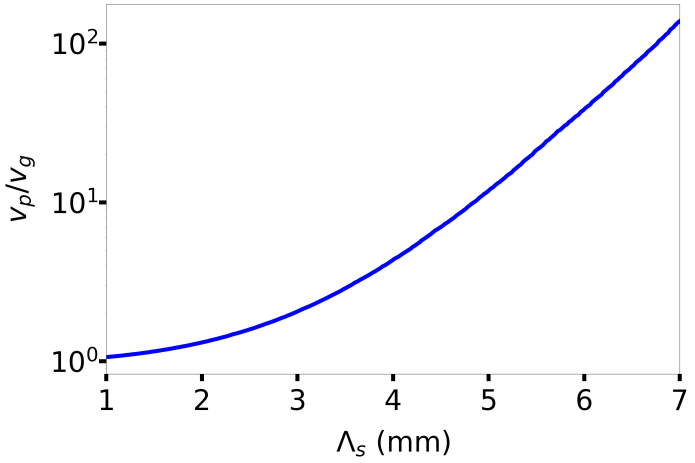

FIGURE 6.4: Group velocity of a Gaussian apodized π-phase shifted grating vs superstructure period Λ_s. With parameters $\alpha_s = 16$, $\lambda_1 = 1064\,\text{nm}$, $\bar{n} = 2.147$, $\delta n = 10^{-3}$ and $L = 4\,\text{cm}$.

As the second-harmonic field increases quadratically with the fundamental field, for a fundamental field enhancement of v_0/v_g the enhancement of second-harmonic generation will be of the order $(v_0/v_g)^2$. However, this does not take into account pump depletion. For longer devices with high initial intensities, the conversion enhancement will decrease as the conversion rate in a standard periodically poled device increases. Therefore, the greatest enhancements will be achieved for shorter length devices with lower pump intensities.

6.3 Device parameters and second-harmonic enhancement

This section looks at how varying the device parameters affects second-harmonic generation and how they can be optimised.

6.3.1 Varying the moiré period

The principle parameter of interest is the moiré period. Increasing the moiré period reduces the size of the transmission band, inducing slow light and enhancing the field intensity. The expectation is that second-harmonic generation will increase with the moiré period. Figure 6.5 shows a simulation calculated using the numerical methods laid out in subsection 6.1.3 of the output powers for the four propagating fields as the superstructure period Λ_S is varied. For the forward propagating modes u_1 and u_2, the output is taken at $x = L$, for the backward propagating modes the output is taken at $x = 0$. The device has a length of $L = 4\,\text{cm}$, a reflection grating length of $L_R = 1\,\text{mm}$, a grating strength given by $\delta n = 10^{-3}$, and grating phases set to $\phi_1 = \phi_2 = 0$. The moiré period is varied from 1 mm to 7 mm with an input intensity of $I = 10^3\,\text{W/cm}^2$.

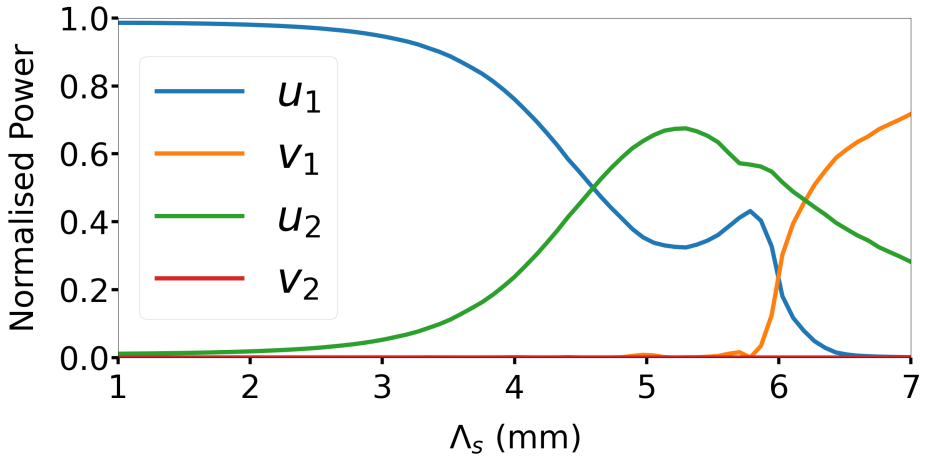

FIGURE 6.5: Output powers for fundamental and second-harmonic fields versus superstructure period Λ_S, where powers are normalised to the input fundamental power. With parameters $\lambda_1 = 1064\,\text{nm}$, $L = 4\,\text{cm}$, $L_f = 1\,\text{mm}$, $\alpha_s = 16$, $\delta n = 10^{-3}$, $\bar{n}_1 = 2.147$, $\bar{n}_2 = 2.223$, $\chi^{(2)} = 25\,\text{pm/V}$, $I = 10^3\,\text{W/cm}^2$, $\phi_1 = 0$ and $\phi_2 = 0$.

As expected, increasing Λ_S causes a corresponding increase in second-harmonic generation. However, the increase does not continue indefinitely but reaches a maximum value at $\Lambda_S = 5.3\,\text{mm}$, corresponding to a slow down factor of 16.6. This gives a conversion efficiency of 67% and an enhancement a factor of 65.5 compared to a periodically poled crystal without linear gratings which will be discussed later in figure 6.9.

Once Λ_S passes its maximum value, the power begins to transfer from the second-harmonic into the backward fundamental mode. This behaviour can be understood by looking at the coupled mode equations (6.13-6.16). There are two different channels for the input power to transfer into the backwards fundamental mode. The first channel is simply via the coupling of the superstructure grating κ_1. The second channel is to couple first into u_2 via κ_3, then into v_2 via κ_2 and then finally into v_1 again via κ_3. For values of Λ_S above the maximum conversion efficiency, this second channel starts to become dominant and power in u_2 transfers to v_1.

6.3.2 Optimising the grating phases

The maximum second-harmonic conversion efficiency and the corresponding moiré period are dependent on the Bragg phases ϕ_1 and ϕ_2. Figure 6.6 shows a simulation of the normalised output power of the forward second-harmonic when ϕ_1 and ϕ_2 are varied through 2π. As the phases are varied, there is an interaction between the two linear gratings which can create a resonance or antiresonance. This behaviour is only seen when both the superstructure grating and reflection grating are present. Varying the phase of the superstructure phase ϕ_1 with the reflection grating removed has no effect on the second-harmonic generation.

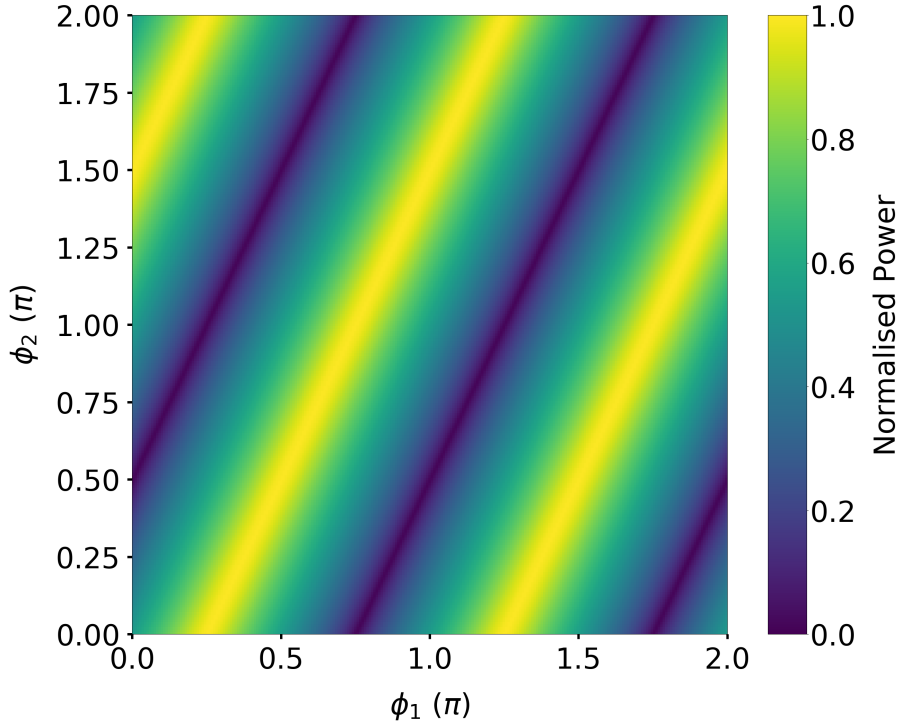

FIGURE 6.6: Normalised output power of the forward second-harmonic field versus Bragg phases ϕ_1 and ϕ_2. $\Lambda_S = 5.3\,\text{mm}$, other parameters as in Fig. 6.5.

Figure 6.7 shows one dimensional slices of figure 6.6 where one of the phases is kept constant at zero. It is possible to deduce that the maximum conversion efficiency occurs when the phases are related by the following constraint

$$\phi_1 - \frac{\phi_2}{2} = \frac{\pi}{4}. \tag{6.24}$$

Similarly, the phase which provides the minimum conversion is given by

$$\phi_1 - \frac{\phi_2}{2} = \frac{3\pi}{4} \tag{6.25}$$

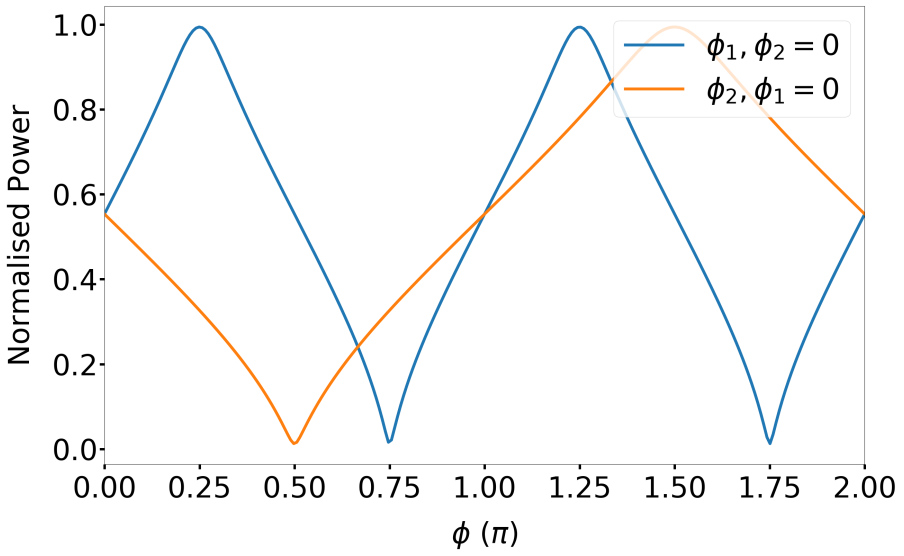

FIGURE 6.7: 1-dimensional cuts through Fig. 6.6 at $\phi_1 = 0$ and $\phi_2 = 0$.

Setting the phases to $\phi_1 = \pi/4$ and $\phi_2 = 0$ satisfies the constraint (6.24) giving maximum conversion efficiency. Figure 6.8 shows again the field output powers versus Λ_S but with the phases optimised. The effect is to increase the second-harmonic conversion efficiency to 99% at $\Lambda_S = 5.8\,\text{mm}$ which corresponds to a slow down factor of 26.2.

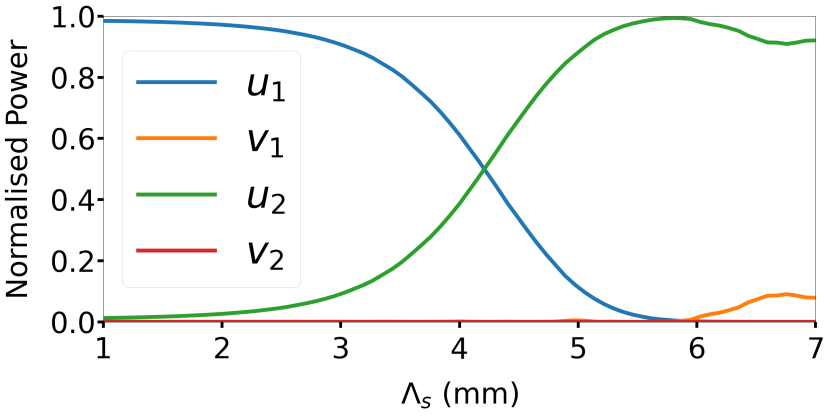

FIGURE 6.8: Phase optimised output powers for fundamental and second-harmonic fields versus superstructure period with $\phi_1 = \pi/4$ and other parameters as in Fig. 6.5.

Figure 6.9 shows the enhancement factor of the forward second-harmonic compared to a standard device when the phases are set to zero, and when they have been optimised. With the optimised phase the enhancement factor has increased from 65.5 to 96.7.

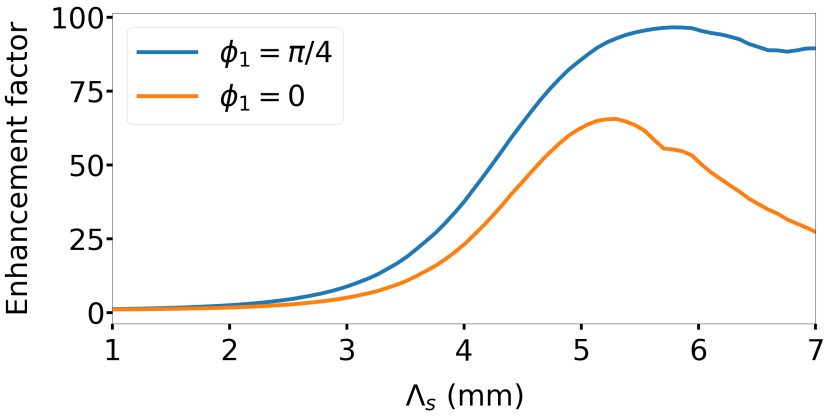

FIGURE 6.9: Enhancement of SHG conversion efficiency compared to a periodically poled crystal without linear gratings with $\phi_1 = \pi/4$ and other parameters as in Fig. 6.5.

When looking at the field distribution of the forward second-harmonic along the length of the device, the maximum and minimum phase constraints given by equations (6.24) and (6.25) give quite different behaviour. Figure 6.10 shows the forward second-harmonic along the device length for the different phase constraints. When the phases satisfy the minimum constraint, there is strong coupling into the backward second-harmonic mode, which is subsequently coupled into the forward second-harmonic mode by the reflection grating. The orange line in figure 6.10 shows this behaviour, where there is a large increase in the forward second-harmonic at the end of the reflection grating. The power is then converted back into the forward fundamental wave, with notable depletion of the second-harmonic at the location of the π phase shifts in the slow light grating. This is in contrast to when the phases satisfy the maximum constraint (6.24), and the forward second-harmonic increases continuously over the length of the device. The grating phases, therefore, have a strong affect on the overall efficiency of the second-harmonic generation.

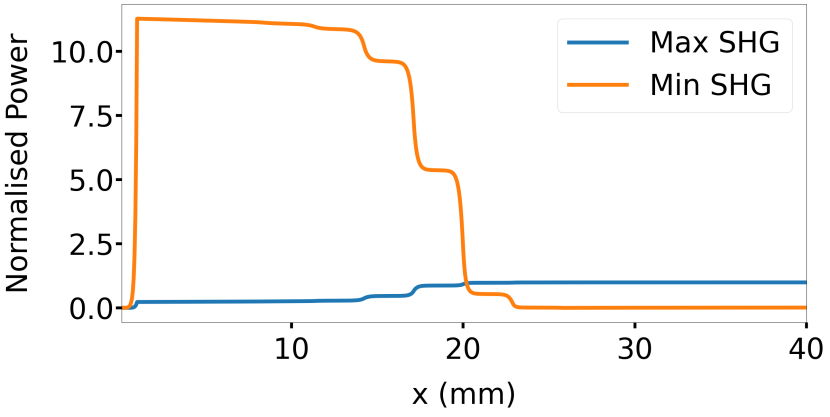

FIGURE 6.10: Comparison of power flow normalised to input power across the device length for the forward second-harmonic mode, with ϕ_1 set to produce maximum and minimum conversion to the second-harmonic, respectively. Here $\Lambda_S = 5.78$ mm, other parameters as in Fig. 6.5

6.3.3 Varying the device lengths

In a standard QPM device, the longer the length of the device, the longer the interaction length and therefore the higher the conversion efficiency. Figure 6.11 shows how the conversion efficiency is affected by the device length when the linear gratings are included. The parameters are the same as used previously with the optimised moiré period $\Lambda_S = 5.8\,\text{mm}$ and grating phases $\phi_1 = \pi/4$ and $\phi_2 = 0$ for a 4 cm long device.

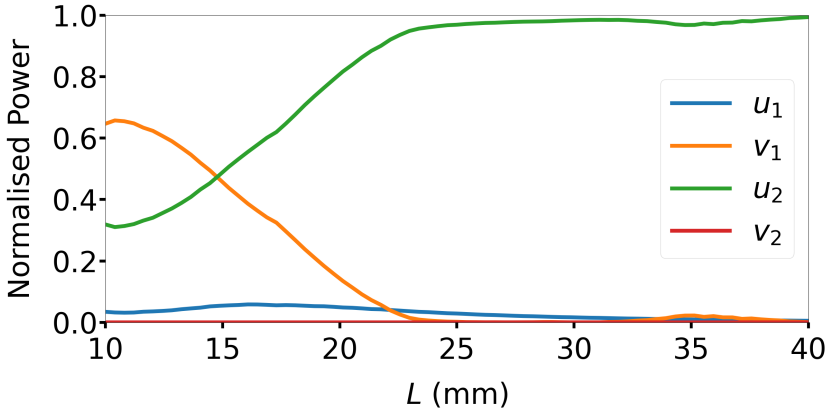

FIGURE 6.11: Normalised output powers for fundamental and second-harmonic modes versus device length L with $\Lambda_S = 5.78\,\text{mm}$, $\phi_1 = \pi/4$ and other parameters as in Fig. 6.5

The figure shows that the conversion efficiency remains close to 100% down to a device length of around 2.5 cm after which the efficiency starts to reduce. At a device length of 10 mm the efficiency reduces down 32% with power being transferred into the backward fundamental mode.

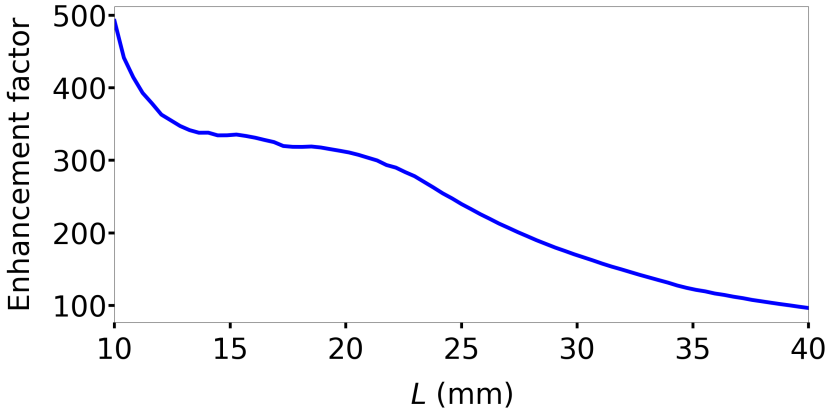

FIGURE 6.12: Enhancement of SHG efficiency compared to a QPM device without linear gratings by device length with $\Lambda_S = 5.78\,\text{mm}$, $\phi_1 = \pi/4$ and other parameters as in Fig. 6.5

Figure 6.12 shows the enhancement factor for the forward second-harmonic in figure 6.11 compared to a QPM device without linear gratings. At a device length of 10 mm

the enhancement factor is 492 which is significantly higher than at a device length of 4 cm for which the parameters are optimised. This is because as the interaction length is increased, the amount of second-harmonic in a standard device is also increased and therefore the overall enhancement is decreased. A general feature of the inclusion of the linear gratings is that shorter devices generate higher enhancement factors, whereas longer devices have higher conversion efficiency.

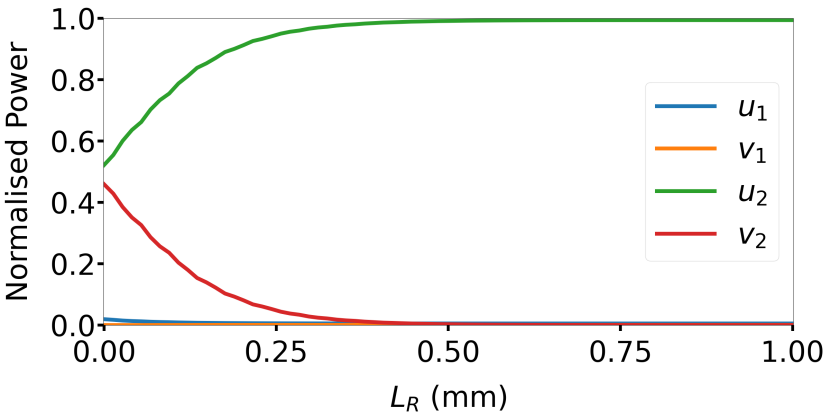

FIGURE 6.13: Output powers versus length of the reflection grating L_R with $\Lambda_S = 5.78\,\text{mm}$, $\phi_1 = \pi/4$ and other parameters as in Fig. 6.5

The other key length associated with the device is the length of the reflection grating L_R. Figure 6.13 shows how varying the reflection grating length from 0 to 1 mm affects the second-harmonic generation. The purpose of the reflection grating is to couple the backwards second-harmonic to the forward second-harmonic so that the second-harmonic exiting the device is unidirectional. When L_R is set to zero, the figure shows that the harmonic generation is split almost evenly between the forward and backward modes. As the length of the reflection grating is increased, the power in the backward mode couples into the forward mode. Once the grating has reached a sufficient length, i.e., for $L_R \gg 1/\kappa_2 = 0.17$ mm, the backward mode becomes almost completely suppressed. As the previous section on optimising the phases showed, there is an interaction between the reflection and slow light grating, one might expect that the length of the reflection grating might affect this relationship. However, once the reflection grating is long enough to suppress the backwards harmonic mode, any further increase does not lead to a further increase in the forwards mode.

6.3.4 Varying the input intensity

The input intensity has so far been fixed to $10^3\,\text{W/cm}^2$ which in a standard 4 cm long QPM device produces low conversion efficiency. As second-harmonic generation scales quadratically with the input intensity, it is instructive to investigate the performance

of the device over a range of input intensities. Figure 6.14 shows how the second-harmonic generation efficiency is affected when the input intensity is varied from $10\,\mathrm{W/cm^2}$ to $10^5\,\mathrm{W/cm^2}$.

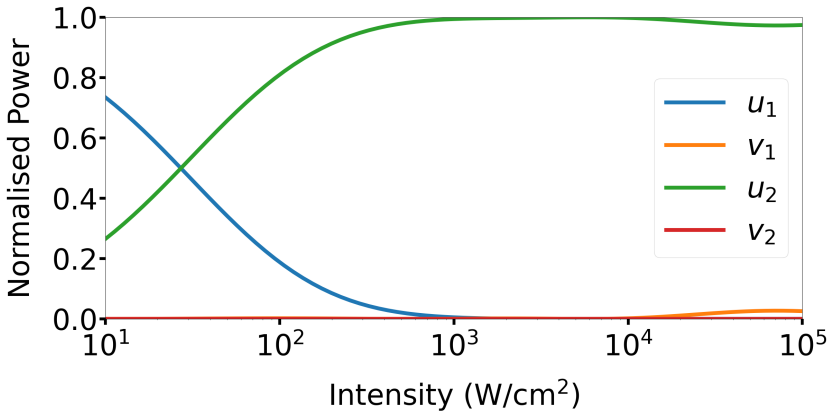

FIGURE 6.14: Output powers for fundamental and second-harmonic modes versus input intensity with $\Lambda_S = 5.78\,\mathrm{mm}$, $\phi_1 = \pi/4$ and other parameters as in Fig. 6.5.

The device parameters used are the ones previously found to optimise the second-harmonic generation for an input intensity of $10^3\,\mathrm{W/cm^2}$. The figure shows that a conversion efficiency close to 100% is achieved over roughly three orders of magnitude from $10^3\,\mathrm{W/cm^2}$ to $10^5\,\mathrm{W/cm^2}$. Below $10^2\,\mathrm{W/cm^2}$ the efficiency starts decreasing reaching 25% efficiency at $10\,\mathrm{W/cm^2}$.

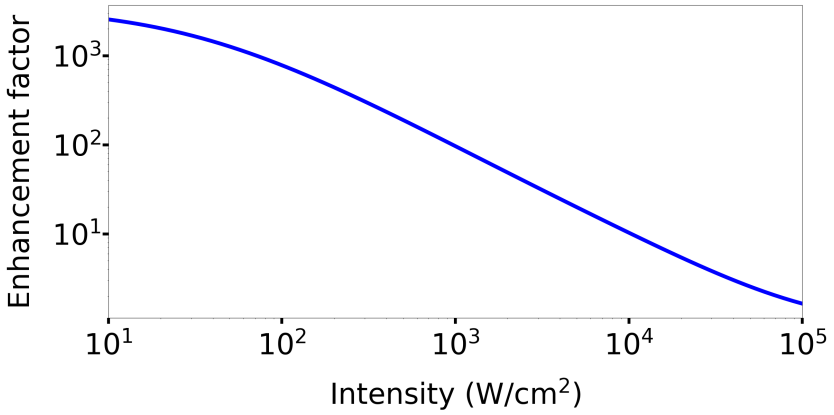

FIGURE 6.15: SHG enhancement over a standard QPM device versus input intensity with $\Lambda_S = 5.78\,\mathrm{mm}$, $\phi_1 = \pi/4$ and other parameters as in Fig. 6.5.

Figure 6.15 shows the corresponding enhancement factor compared to a standard QPM device. Analogous to varying the device length, lower intensities have greater enhancement factors and higher intensities have greater conversion efficiency. For an input intensity of $10\,\mathrm{W/cm^2}$ the second-harmonic generation is enhanced by a factor of 2555 compared to a factor of 1.6 for an input intensity of $10^5\,\mathrm{W/cm^2}$.

6.3.5 Varying the grating strength

The slow light field enhancement is dependent not only on the moiré period, but also on the grating strength δn. Larger values of δn decrease the group velocity producing larger field enhancement; consequently setting $\delta n = 0$ recovers a standard QPM device. Figure 6.16 shows how the second-harmonic generation varies with the grating strength with device parameters as in figure 6.5 with optimised phases $\phi_1 = \pi/4$ and $\phi_2 = 0$, and moiré period $\Lambda_S = 5.78\,\text{mm}$. Figure 6.17 shows the corresponding enhancement factor.

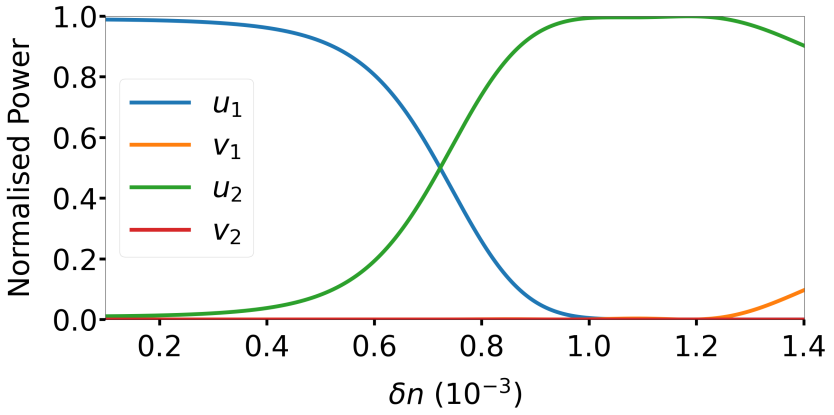

FIGURE 6.16: Output powers for fundamental and second-harmonic modes versus grating strength δn with $\Lambda_S = 5.78\,\text{mm}$, $\phi_1 = \pi/4$ and other parameters as in Fig. 6.5

Just as was seen with the moiré period, increasing the grating strength leads to an increase in the second-harmonic up to a limit, at which point the power couples into the backward fundamental mode. Decreasing the grating strength decreases the second-harmonic generation. At $\delta n = 10^{-4}$ the slow down factor is reduced to 1.01 resulting in almost zero second-harmonic generation.

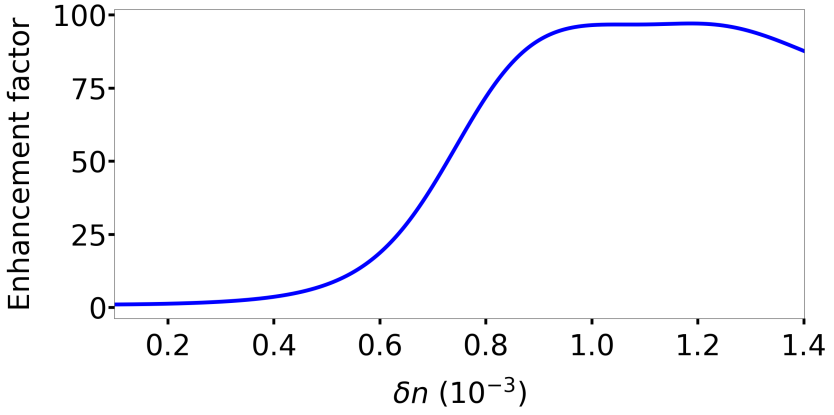

FIGURE 6.17: SHG enhancement over a standard QPM device versus grating strength δn with $\Lambda_S = 5.78\,\text{mm}$, $\phi_1 = \pi/4$ and other parameters as in Fig. 6.5

6.4 Summary

This chapter has investigated using a π-phase shifted superstructure grating with a slow light transmission band to enhance second-harmonic generation in a quasi-phase matched device. By tuning the grating so that the centre of the transmission band corresponds to the fundamental mode, the induced slow light increases the rate of second-harmonic generation. The superstructure grating couples forward and backward fundamental modes, which in turn generates forward and backward harmonic modes. Therefore, a second linear Bragg grating is introduced at the start of the device to suppress the backward second-harmonic ensuring that the second-harmonic is unidirectional.

The conversion efficiency increases with the moiré period until it reaches a maximum value after which the second-harmonic couples back into the fundamental mode; similar behaviour was observed for both the grating strength and the input intensity. The device can be further optimised by setting the relative phases of the grating to take advantage of a resonator effect formed between the linear gratings. In the parameter regime investigated it was found that the device exhibits near-unity conversion efficiency for intensities spanning three order of magnitude.

Chapter 7

Conclusions and future work

7.1 Conclusion

In this thesis I presented a new approach to storing and releasing optical pulses based on slow light dynamic moiré gratings. By dynamically varying the grating strength it is possible to compress the pulse spectrum and dramatically decrease group velocity inside the grating. The dynamic compressing of the pulse bandwidth allows the device to beat the delay-bandwidth product of a static moiré grating. Further, I showed that a slow light π-phase shifted grating is capable of producing enhanced second-harmonic generation. Combined with a back reflecting grating, the two gratings form a resonance which is capable of producing near unity conversion efficiency at low intensities.

All the devices investigated in this thesis have been modelled using coupled mode theory. Chapter 3 introduced a new method of producing couple mode equations based on the Lagrangian formalism. The usual approach to developing coupled mode equations relies on having to take multiple versions of the electromagnetic wave equation and applying different approximations on each other them in order to produce a set of coupled of equations. The benefit of using the Lagrangian formalism is that the equations can be derived from a single expression, namely the Lagrangian. With only one expression needed only a single set of approximations need to be made. The equations of motion result from varying the Lagrangian with respect to the modes, which gives a set of coupled mode equations. As the Lagrangian is closely related to the Hamiltonian, the resulting equations conserve energy.

Chapter 4 investigated dynamic moiré grating. The main difficulty with slow light devices is the delay-bandwidth product. Slow light devices tend to either have a narrow resonance and longer length, or a broader resonance and a shorter length. Therefore, it is hard for a slow light device to compete with an optical fibre. They have a wide acceptance bandwidth and even though their group velocity is significantly higher than

a slow light device, they can be made arbitrarily long which increases the delay time. However, increasing the fibre length means longer retrieval times limiting their use. Therefore, it would be of great practical benefit to make a slow device that could both store and release a pulse on demand. A way around the delay-bandwidth product constraint in slow light devices is to use an adiabatically tuned resonance. This allows a larger initial bandwidth with a subsequently lower group velocity through adiabatic tuning. The problem with such a device is localisation. A pulse must be fully localised within the device before the tuning takes place. Therefore, the device must be long enough to accommodate the pulse. A dynamic moiré grating is a good candidate to create such a device as they can be written into waveguides and as such can be made to lengths sufficient to accommodate a signal pulse. By dynamically varying the size of the moiré transmission bandwidth a pulse localised in the device has its spectrum compressed and experiences a reduction in its group velocity. My simulations showed that the group velocity could be reduced by many orders of magnitude with the delay-bandwidth product increasing inversely with decreasing group velocity. In section 4.4 a possible realisation of dynamic moiré grating was proposed using an electro-optic grating.

In chapter 5 creating delay lines with fast switching times using Bragg and moiré grating was investigated. By using a strong pump pulse, XPM could be used to alter the Bragg condition of a grating shifting the rejection bandwidth. Therefore, by using XPM a grating can be used as a gate to allow a single pulse to pass. By having two such gratings, a storage device could be created using XPM to store and release pulses. The change in the refractive index using XPM is on the order of $10^{-6} - 10^{-5}$ and shifting the entire band gap would require a grating strength of the same order magnitude as the refractive index change. To create gratings with high reflectance with such a small grating strength would require gratings roughly 2 m in length which is beyond the fabrication limits of current ultra-long gratings. This situation can be improved by not requiring that the entire rejection band gap be shifted, but instead use the shifted bandwidth at the rejection band edge so that a larger grating strength can be used. While this reduces the required grating length considerable, an apodisation is necessary to suppress sidelobing. This increases the grating size but to a length within fabrication limits. The downside of using the band edge is that strong second order dispersion will mean significant pulse broadening. Another approach looked at in the chapter was to shift the transmission band of a moiré grating. This approached showed that significantly smaller gratings could be used even with an apodisation applied. Whether a Bragg of moiré grating was used, successive reflections off of the gratings introduced pulse distortions which limits the practical use of the device.

The affects of slow light on enhancing second-harmonic generation were investigated in chapter 6. I demonstrated that a closely related grating to the moiré grating, the π-phase shifted grating could be used in conjunction with a quasi-phase matching scheme

to enhance the efficiency of second-harmonic generation. It was found that there was a optimum superstructure period beyond which power was transferred from the second-harmonic into the backward fundamental mode. Similarly the π-phase shifted grating creates both forward and backward modes, so a second reflection grating was added to start of the grating to suppress the backward second-harmonic. It was found that the inclusion of this second grating created a resonance with the π-phase shifted grating which further enhanced the second-harmonic generation. For all parameter regimes invested the inclusion of the slow light grating device provided significant enhancement over a standard quasi-phase matched device. The greatest enhancement came from shorter devices with lower pump intensities, therefore the device could be useful for small chip-scale devices and quantum applications.

7.2 Future work

Typically, electromagnetism is expressed in a covariant form when using Lagrangian formalism but only the vacuum expressions are of interest. When matter is included, the covariant formalism can not be used. The reason for this is that Maxwell's equation in matter break Lorentz invariance. Therefore, expressing the equations in a covariant form would be an abuse of notation. However, there are a number of problems with this. The largest perhaps is the correct definition of the electromagnetic momentum which has been an unsettled problem for a hundred years. This problem stems from the correct definition of the stress energy tensor and in section 3.2.1 it was shown that some licence needs to be taken in order to derive it. In my own work in this area, I found that incorporating matter into the electromagnetism alters the underlying metric structure. In turn this breaks Lorentz invariance and subsequently alters the form of the stress energy tensor. However, while I did not develop these ideas sufficiently to include them in this thesis, I do believe they form a good basis for further research. Therefore further work in this area can look at developing a covariant formalisation of Maxwell equations in matter.

Further work in the area of dynamic gratings would be to try to fabricate such a device to demonstrate the theory in this thesis is valid. Current limits on the refractive index change of an electro-optic grating using lithium niobate is in the order of 10^{-4}; therefore only small bandwidth changes could be made. Nonetheless small changes in the group velocity could be observed. It may be possible to induce larger refractive index changes using an alternative medium or using a different method to realise the device. In developing delay lines, additional work in this area could focus on finding grating and apodisation profiles that minimise pulse distortions. Also while SPM was discussed, further work could also include a full simulation including material dispersion to see the affect SPM has on the profile of the pump pulse. Finally, the chapter exploring the enhancement of second-harmonic generation using slow light gratings

developed a theoretical model that showed promising results. Further work could focus on the fabrication of these devices to test the modelled behaviour. There have been groups developing the technology [94, 95] necessary for experimental verification and so it could be possible to realise a device in the near future.

Appendix A

Research Project Output

A.1 Journal Articles

T. E. Maybour, D. H. Smith, and P. Horak, "Slow and stopped light in dynamic moire gratings," Phys. Rev. A, vol. 104, p. 013503, (2021)

T. E. Maybour, D. H. Smith, and P. Horak, "Grating-induced slow-light enhancement of second harmonic generation in periodically poled crystals," Phys. Rev. A, vol. 105, p. 013517, (2022)

A.2 Conference Proceedings and Presentation

(Conference Proceedings & Poster Presentation) T.E Maybour, D. Smith and P.Horak (2021) Slow-Light Enhanced Second-Harmonic Generation Using a π-Phase Shifted Moiré Grating in a Quasi-Phased-Matched Medium. CLEO/Europe-EQEC 2021, 21 - 25 June 2021, Munich, Germany.

(Conference Proceedings & Poster Presentation) T.E Maybour and P.Horak (2019) Slow and stopped light in a time-dependent Moiré grating. CLEO/Europe-EQEC 2019, 23 - 27 June 2019, Munich, Germany.

(Conference Proceedings & Oral Presentation) T.E Maybour, D. Smith and P.Horak (2018) Slow light propagation through a Moire grating at the zero dispersion wavelength. At Photon 2018, 3 - 6 Sep 2018, Birmingham, United Kingdom. IoP.

References

[1] Nicolas Sangouard, Christoph Simon, Hugues de Riedmatten, and Nicolas Gisin. Quantum repeaters based on atomic ensembles and linear optics. *Reviews of Modern Physics*, 83:33–80, 2011. doi:10.1103/RevModPhys.83.33.

[2] Yun-Fei Pu, Sheng Zhang, Yu-Kai Wu, Nan Jiang, Wei Chang, Chang Li, and Lu-Ming Duan. Experimental demonstration of memory-enhanced scaling for entanglement connection of quantum repeater segments. *Nature Photonics*, 15:374–378, 2021. doi:10.1038/s41566-021-00764-4.

[3] Alexander I. Lvovsky, Barry C. Sanders, and Wolfgang Tittel. Optical quantum memory. *Nature Photonics*, 3:706–714, 2009. doi:10.1038/nphoton.2009.231.

[4] Rachel Won. Slow light now and then. *Nature Photonics*, 2:454–455, 2008. doi:10.1038/nphoton.2008.148.

[5] Thomas F. Krauss. Why do we need slow light? *Nature Photonics*, 2:448–450, 2008. doi:10.1038/nphoton.2008.139.

[6] Toshihiko Baba. Slow light in photonic crystals. *Nature Photonics*, 2:465–473, 2008. doi:10.1038/nphoton.2008.146.

[7] Luc Thévenaz. Slow and fast light in optical fibres. *Nature Photonics*, 2:474–481, 2008. doi:10.1038/nphoton.2008.147.

[8] Jacob B. Khurgin. Slow light in various media: a tutorial. *Advances in Optics and Photonics*, 2:287–318, 2010. doi:10.1364/AOP.2.000287.

[9] George M. Gehring, Robert W. Boyd, Alexander L. Gaeta, Daniel J. Gauthier, and Alan E. Willner. Fiber-based slow-light technologies. *Journal of Lightwave Technology*, 26:3752–3762, 2008. doi:10.1109/JLT.2008.2004883.

[10] George Skolianos, Arushi Arora, Martin Bernier, and Michel Digonnet. Slow light in fiber bragg gratings and its applications. *Journal of Physics D: Applied Physics*, 49:463001, 2016. doi:10.1088/0022-3727/49/46/463001.

[11] J.B. Khurgin and R.S. Tucker. *Slow Light: Science and Applications*. CRC Press, 2018.

[12] G. Lenz, B.J. Eggleton, C.K. Madsen, and R.E. Slusher. Optical delay lines based on optical filters. *IEEE Journal of Quantum Electronics*, 37:525–532, 2001. doi:10.1109/3.914401.

[13] R.S. Tucker, Pei-Cheng Ku, and C.J. Chang-Hasnain. Slow-light optical buffers: capabilities and fundamental limitations. *Journal of Lightwave Technology*, 23:4046–4066, 2005. doi:10.1109/JLT.2005.853125.

[14] Jacob B. Khurgin. Optical buffers based on slow light in electromagnetically induced transparent media and coupled resonator structures: comparative analysis. *Journal of the Optical Society of America B*, 22:1062–1074, 2005. doi:10.1364/JOSAB.22.001062.

[15] J. R. Pierce. Traveling-wave tubes. *The Bell System Technical Journal*, 29:1–59, 1950. doi:10.1002/j.1538-7305.1950.tb00932.x.

[16] S. L. McCall and E. L. Hahn. Self-induced transparency by pulsed coherent light. *Physical Review Letters*, 18:908–911, 1967. doi:10.1103/PhysRevLett.18.908.

[17] D. Grischkowsky. Adiabatic following and slow optical pulse propagation in rubidium vapor. *Physical Review A*, 7:2096–2102, 1973. doi:10.1103/PhysRevA.7.2096.

[18] Lene Vestergaard Hau, S. E. Harris, Zachary Dutton, and Cyrus H. Behroozi. Light speed reduction to 17 metres per second in an ultracold atomic gas. *Nature*, 397: 594–598, 1999. doi:10.1038/17561.

[19] Stephen E Harris. Electromagnetically induced transparency. *Physics Today*, 50: 36–42, 1997. doi:10.1063/1.881806.

[20] Chien Liu, Zachary Dutton, Cyrus H. Behroozi, and Lene Vestergaard Hau. Observation of coherent optical information storage in an atomic medium using halted light pulses. *Nature*, 409:490, 2001. doi:10.1038/35054017.

[21] D. F. Phillips, A. Fleischhauer, A. Mair, R. L. Walsworth, and M. D. Lukin. Storage of light in atomic vapor. *Physical Review Letters*, 86:783, 2001. doi:10.1103/PhysRevLett.86.783.

[22] S. E. Schwarz and T. Y. Tan. Wave interactions on saturable absorbers. *Applied Physics Letters*, 10:4–7, 1967. doi:10.1063/1.1754798.

[23] Lloyd W. Hillman, Robert W. Boyd, Jerzy Krasinski, and C.R. Stroud. Observation of a spectral hole due to population oscillations in a homogeneously broadened optical absorption line. *Optics Communications*, 45:416–419, 1983. doi:10.1016/0030-4018(83)90303-6.

[24] Matthew S. Bigelow, Nick N. Lepeshkin, and Robert W. Boyd. Observation of ultraslow light propagation in a ruby crystal at room temperature. *Physical Review Letters*, 90:113903, 2003. doi:10.1103/PhysRevLett.90.113903.

[25] Fengnian Xia, Lidija Sekaric, and Yurii Vlasov. Ultracompact optical buffers on a silicon chip. *Nature Photonics*, 1:65–71, 2007. doi:10.1038/nphoton.2006.42.

[26] F. Morichetti, C. Ferrari, A. Canciamilla, and A. Melloni. The first decade of coupled resonator optical waveguides: bringing slow light to applications. *Laser and Photonics Reviews*, 6:74–96, 2012. doi:10.1002/lpor.201100018.

[27] Yong Wan, Li-Jun Jiang, Sheng Xu, Meng-Xue Li, Meng-Nan Liu, Cheng-Yi Jiang, and Feng Yuan. Slow light effect with high group index and wideband by saddle-like mode in pc-crow. *Frontiers of Physics*, 13:134202, 2018. doi:10.1007/s11467-017-0719-1.

[28] Jacob B. Khurgin. Optical buffers based on slow light in electromagnetically induced transparent media and coupled resonator structures: comparative analysis. *Journal of the Optical Society of America B*, 22:1062–1074, 2005. doi:10.1364/JOSAB.22.001062.

[29] Yoshitomo Okawachi, Matthew S. Bigelow, Jay E. Sharping, Zhaoming Zhu, Aaron Schweinsberg, Daniel J. Gauthier, Robert W. Boyd, and Alexander L. Gaeta. Tunable all-optical delays via brillouin slow light in an optical fiber. *Physical Review Letters*, 94:153902, 2005. doi:10.1103/PhysRevLett.94.153902.

[30] V. I. Kovalev, N. E. Kotova, and R. G. Harrison. Slow light in stimulated brillouin scattering: on the influence of the spectral width of pump radiation on the group index. *Optics Express*, 18:8053, 2010. doi:10.1364/oe.17.017317.

[31] K. O. Hill, Y. Fujii, D. C. Johnson, and B. S. Kawasaki. Photosensitivity in optical fiber waveguides: Application to reflection filter fabrication. *Applied Physics Letters*, 32:647–649, 1978. doi:doi:10.1063/1.89881.

[32] G. M. Gehring, R. W. Boyd, A. L. Gaeta, D. J. Gauthier, and A. E. Willner. Fiber-based slow-light technologies. *Journal of Lightwave Technology*, 26:3752–3762, 2008. doi:10.1109/JLT.2008.2004883.

[33] Joe T. Mok, C. Martijn de Sterke, and Benjamin J. Eggleton. Delay-tunable gap-soliton-based slow-light system. *Optics Express*, 14:11987–11996, 2006. doi:10.1364/OE.14.011987.

[34] George Skolianos, Arushi Arora, Martin Bernier, and Michel J. F. Digonnet. Slowing down light to 300 km/s in a deuterium-loaded fibre bragg grating. *Optics Letters*, 40:1524–1527, 2015. doi:10.1364/ol.40.001524.

[35] Jacob B. Khurgin. Light slowing down in moiré fiber gratings and its implications for nonlinear optics. *Physical Review A*, 62:013821, 2000. doi:10.1103/PhysRevA.62.013821.

[36] D. Janner, G. Galzerano, G. Della Valle, P. Laporta, S. Longhi, and M. Belmonte. Slow light in periodic superstructure bragg gratings. *Physical Review E*, 72:056605, 2005. doi:10.1103/PhysRevE.72.056605.

[37] James Clerk Maxwell. Viii. a dynamical theory of the electromagnetic field. *Philosophical Transactions of the Royal Society of London*, 155:459–512, 1865. doi:https://doi.org/10.1098/rstl.1865.0008.

[38] Amnon Yariv. Coupled-mode theory for guided-wave optics. *IEEE Journal of Quantum Electronics*, 9:919–933, 1973. doi:10.1109/JQE.1973.1077767.

[39] K. Okamoto. *Fundamentals of Optical Waveguides*. Academic Press, 2nd edition edition, Dec 2004.

[40] Raman Kashyap. *Fiber Bragg Gratings*. Academic Press, 2nd edition edition, Nov 2009.

[41] K Fujii. Introduction to the rotating wave approximation (rwa): Two coherent oscillations. *Journal of Modern Physics*, 8:2042–2058, 2017. doi:10.4236/jmp.2017.812124.

[42] P. A. Franken, A. E. Hill, C. W. Peters, and G. Weinreich. Generation of optical harmonics. *Physical Review Letters*, 7:118–119, 1961. doi:10.1103/PhysRevLett.7.118.

[43] N. Bloembergen and P. S. Pershan. Light waves at the boundary of nonlinear media. *Physical Review*, 128:606–622, 1962. doi:10.1103/PhysRev.128.606.

[44] R.W. Boyd. *Nonlinear Optics*. Elsevier Science, 2019.

[45] J. A. Armstrong, N. Bloembergen, J. Ducuing, and P. S. Pershan. Interactions between light waves in a nonlinear dielectric. *Physical Review*, 127:1918–1939, 1962. doi:10.1103/PhysRev.127.1918.

[46] T.W.B. Kibble and F.H. Berkshire. *Classical Mechanics*. Imperial College Press, 2004.

[47] H Goldstein, C Poole, and J Safko. *Classical Mechanics*. Addison-Wesley, third edition edition, 2002.

[48] L.D. Landu and E.M. Lifshitz. *The Classical Theory of Fields*, volume 2. Pergamon, fourth edition edition, 1975.

[49] Joseph-Louis Lagrange. *Mécanique analytique*, volume 1. 1788.

[50] Joseph-Louis Lagrange. *Mécanique analytique*, volume 2. 1788.

[51] W.N. Cottingham and D.A. Greenwood. *An Introduction to the Standard Model of Particle Physics*. Cambridge University Press, 2007.

[52] P. Y. Chen, R. C. McPhedran, C. M. de Sterke, C. G. Poulton, A. A. Asatryan, L. C. Botten, and M. J. Steel. Group velocity in lossy periodic structured media. *Physical Review A*, 82:053825, 2010. doi:10.1103/PhysRevA.82.053825.

[53] Hans G. Schantz. Energy velocity and reactive fields. *Philosophical Transactions of the Royal Society A*, 376(2134):20170453, 2018. doi:10.1098/rsta.2017.0453.

[54] Thomas E. Maybour, Devin H. Smith, and Peter Horak. Slow and stopped light in dynamic moiré gratings. *Physical Review A*, 104:013503, 2021. doi:10.1103/PhysRevA.104.013503.

[55] Kwang Yong Song, Weiwen Zou, Zuyuan He, and Kazuo Hotate. All-optical dynamic grating generation based on brillouin scattering in polarization-maintaining fiber. *Optics Letters*, 33:926–928, 2008. doi:10.1364/OL.33.000926.

[56] Mehmet Fatih Yanik and Shanhui Fan. Dynamic photonic structures stopping, storage, and time reversal of light. *Studies in Applied Mathematics*, 115:233–253, 2005. doi:10.1111/j.1467-9590.2005.00327.x.

[57] Mehmet Fatih Yanik and Shanhui Fan. Stopping light all optically. *Physical Review Letters*, 92:083901, 2004. doi:10.1103/PhysRevLett.92.083901.

[58] Mehmet Fatih Yanik and Shanhui Fan. Stopping and storing light coherently. *Physical Review A*, 71:013803, 2005. doi:10.1103/PhysRevA.71.013803.

[59] Mehmet Fatih Yanik, Wonjoo Suh, Zheng Wang, and Shanhui Fan. Stopping light in a waveguide with an all-optical analog of electromagnetically induced transparency. *Physical Review Letters*, 93:233903, 2004. doi:10.1103/PhysRevLett.93.233903.

[60] Jacob Khurgin. Adiabatically tunable optical delay lines and their performance limitations. *Optics Letters*, 30:2778–2780, 2005. doi:10.1364/ol.30.002778.

[61] Brian A. Daniel, Drew N. Maywar, and Govind P. Agrawal. Dynamic mode theory of optical resonators undergoing refractive index changes. *Journal of the Optical Society of America B*, 28:2207–2215, 2011. doi:10.1364/josab.28.002207.

[62] Jacob B. Khurgin. Slowing and stopping photons using backward frequency conversion in quasi-phase-matched waveguides. *Physical Review A*, 72:023810, 2005. doi:10.1103/PhysRevA.72.023810.

[63] Takasumi Tanabe, Eiichi Kuramochi, Hideaki Taniyama, and Masaya Notomi. Electro-optic adiabatic wavelength shifting and q switching demonstrated using a p-i-n integrated photonic crystal nanocavity. *Optics Letters*, 35:3895–3897, 2010. doi:10.1364/ol.35.003895.

[64] Mahmoud A. Gaafar, Jannik Holtorf, Manfred Eich, and Alexander Yu. Petrov. Pulse time reversal and stopping by a refractive index front. *APL Photonics*, 5: 080801, 2020. doi:10.1063/5.0007986.

[65] Tal A. Weiss and Yonatan Sivan. Stopping light using a transient bragg grating. *Physical Review A*, 101:033828, 2020. doi:10.1103/PhysRevA.101.033828.

[66] T. Erdogan. Fiber grating spectra. *Journal of Lightwave Technology*, 15:1277–1294, 1997. doi:10.1109/50.618322.

[67] K. Yee. Numerical solution of initial boundary value problems involving maxwell's equations in isotropic media. *IEEE Transactions on Antennas and Propagation*, 14:302–307, 1966. doi:10.1109/TAP.1966.1138693.

[68] G. P. Agrawal and N. A. Olsson. Self-phase modulation and spectral broadening of optical pulses in semiconductor laser amplifiers. *IEEE Journal of Quantum Electronics*, 25:2297–2306, 1989. doi:10.1109/3.42059.

[69] S. J. Frisken. Transient bragg reflection gratings in erbium-doped fiber amplifiers. *Optics Letters*, 17:1776–1778, 1992. doi:10.1364/ol.17.001776.

[70] Y. Sivan, G. Ctistis, E. Yüce, and A. P. Mosk. Femtosecond-scale switching based on excited free-carriers. *Optics Express*, 23:16416–16428, 2015. doi:10.1364/oe.23.016416.

[71] H. Gnewuch, C. N. Pannell, G. W. Ross, P. G. R. Smith, and H. Geiger. Nanosecond response of bragg deflectors in periodically poled linbo3. *IEEE Photonics Technology Letters*, 10:1730–1732, 1998. doi:10.1109/68.730484.

[72] Keren Fradkin-Kashi and Ady Arie. Multiple-wavelength quasi-phase-matched nonlinear interactions. *IEEE Journal of Quantum Electronics*, 35:1649–1656, 1999. doi:10.1109/3.798088.

[73] M. H. Chou, K. R. Parameswaran, M. M. Fejer, and I. Brener. Multiple-channel wavelength conversion by use of engineered quasi-phase-matching structures in linbo3 waveguides. *Optics Letters*, 24:1157–1159, 1999. doi:10.1364/ol.24.001157.

[74] P. Mackwitz, M. Rüsing, G. Berth, A. Widhalm, K. Müller, and A. Zrenner. Periodic domain inversion in x-cut single-crystal lithium niobate thin film. *Applied Physics Letters*, 108:152902, 2016. doi:10.1063/1.4946010.

[75] Venkatraman Gopalan and Mool C. Gupta. Origin and characteristics of internal fields in LiNbO3 crystals. *Ferroelectrics*, 198:49–59, 1997. doi:10.1080/00150199708228337.

[76] Jonathan Tyler Nagy and Ronald M. Reano. Submicrometer periodic poling of lithium niobate thin films with bipolar preconditioning pulses. *Optical Materials Express*, 10:1911–1920, 2020. doi:10.1364/ome.394724.

[77] Takashi Suzuki and Toshiaki Suhara. Fabrication of one micron period poled structures in MgO:LiNbO3 by bipolar pulse application. *Jpn J Appl Phys*, 52:100204, 2013. doi:10.7567/JJAP.52.100204.

[78] Govind P Agrawal. *Fiber-optic communication systems*. John Wiley & Sons, 2012.

[79] Yoshiaki Tamura, Hirotaka Sakuma, Keisei Morita, Masato Suzuki, Yoshinori Yamamoto, Kensaku Shimada, Yuya Honma, Kazuyuki Sohma, Takashi Fujii, and Takemi Hasegawa. The first 0.14-db/km loss optical fiber and its impact on submarine transmission. *Journal of Lightwave Technology*, 36:44–49, 2018. doi:10.1109/JLT.2018.2796647.

[80] J. E. Swain, W. H. Lowdermilk, and D. Milam. Raising damage thresholds of gradient-index antireflecting surfaces by pulsed laser irradiation. *Applied Physics Letters*, 41:782–783, 1982. doi:10.1063/1.93701.

[81] David Milam. Review and assessment of measured values of the nonlinear refractive-index coefficient of fused silica. *Applied Optics*, 37:546–550, 1998. doi:10.1364/AO.37.000546.

[82] Mathieu Gagné, Sébastien Loranger, Jerome Lapointe, and Raman Kashyap. Fabrication of high quality, ultra-long fiber bragg gratings: up to 2 million periods in phase. *Optics Express*, 22:387–398, 2014. doi:10.1364/oe.22.000387.

[83] Thomas E. Maybour, Devin H. Smith, and Peter Horak. Grating-induced slow-light enhancement of second-harmonic generation in periodically poled crystals. *Phys. Rev. A*, 105:013517, 2022. doi:10.1103/PhysRevA.105.013517.

[84] C Monat, M de Sterke, and B J Eggleton. Slow light enhanced nonlinear optics in periodic structures. *Journal of Optics*, 12:104003, 2010. doi:10.1088/2040-8978/12/10/104003.

[85] A. Ashkin, G. Boyd, and J. Dziedzic. Resonant optical second harmonic generation and mixing. *IEEE Journal of Quantum Electronics*, 2:109–124, 1966. doi:10.1109/JQE.1966.1074007.

[86] W. J. Kozlovsky, C. D. Nabors, and R. L. Byer. Second-harmonic generation of a continuous-wave diode-pumped nd:yag laser using an externally resonant cavity. *Optics Letters*, 12:1014–1016, 1987. doi:10.1364/ol.12.001014.

[87] Yujie J. Ding and Jacob B. Khurgin. Second-harmonic generation based on quasi-phase matching: a novel configuration. *Optics Letters*, 21:1445–1447, 1996. doi:10.1364/ol.21.001445.

[88] Gary D. Landry and Theresa A. Maldonado. Second-harmonic generation and cascaded second-order processes in a counterpropagating quasi-phase-matched device. *Applied Optics*, 37:7809–7820, 1998. doi:10.1364/ao.37.007809.

[89] Claudio Conti, Stefano Trillo, and Gaetano Assanto. Doubly resonant bragg simultons via second-harmonic generation. *Physical Review Letters*, 78:2341–2344, 1997. doi:10.1103/PhysRevLett.78.2341.

[90] Matteo Picciau, Giuseppe Leo, and Gaetano Assanto. Versatile bistable gate based on quadratic cascading in a bragg periodic structure. *Journal of the Optical Society of America B*, 13:661–670, 1996. doi:10.1364/josab.13.000661.

[91] J Hukriede, D Runde, and D Kip. Fabrication and application of holographic bragg gratings in lithium niobate channel waveguides. *Journal of Physics D: Applied Physics*, 36:R1–R16, 2003. doi:10.1088/0022-3727/36/3/201.

[92] Sebastian Kroesen, Wolfgang Horn, Jörg Imbrock, and Cornelia Denz. Electro–optical tunable waveguide embedded multiscan bragg gratings in lithium niobate by direct femtosecond laser writing. *Optics Express*, 22:23339–23348, 2014. doi:10.1364/oe.22.023339.

[93] Mohammad Amin Baghban, Jean Schollhammer, Carlos Errando-Herranz, Kristinn B. Gylfason, and Katia Gallo. Bragg gratings in thin-film LiNbO3 waveguides. *Optics Express*, 25:32323–32332, 2017. doi:10.1364/oe.25.032323.

[94] Mohammad Amin Baghban and Katia Gallo. Phase-shifted bragg grating resonators in thin-film lithium niobate waveguides. In *2019 Conference on Lasers and Electro-Optics (CLEO)*, page SF2J.7. IEEE, 2019. doi:10.1364/CLEO_SI.2019.SF2J.7.

[95] David Pohl, Fabian Kaufmann, Marc Reig Escalé, Jannis Holzer, and Rachel Grange. Tunable bragg grating filters and resonators in lithium niobate-on-insulator waveguides. In *2020 Conference on Lasers and Electro-Optics (CLEO)*, page STu4J.5. IEEE, 2020. doi:10.1364/CLEO_SI.2020.STu4J.5.

[96] D. A. Bryan, Robert Gerson, and H. E. Tomaschke. Increased optical damage resistance in lithium niobate. *Applied Physics Letters*, 44:847–849, 1984. doi:10.1063/1.94946.

[97] Charles R. Harris, K. Jarrod Millman, Stéfan J. van der Walt, Ralf Gommers, Pauli Virtanen, David Cournapeau, Eric Wieser, Julian Taylor, Sebastian Berg, Nathaniel J. Smith, Robert Kern, Matti Picus, Stephan Hoyer, Marten H. van Kerkwijk, Matthew Brett, Allan Haldane, Jaime Fernández del Río, Mark Wiebe, Pearu Peterson, Pierre Gérard-Marchant, Kevin Sheppard, Tyler Reddy, Warren Weckesser, Hameer Abbasi, Christoph Gohlke, and Travis E. Oliphant. Array programming with NumPy. *Nature*, 585:357–362, 2020. doi:10.1038/s41586-020-2649-2.

[98] Y. H. Ja. Using the shooting method to solve boundary-value problems involving nonlinear coupled-wave equations. *Optical and Quantum Electronics*, 15:529–538, 1983. doi:10.1007/BF00620022.

[99] J. A. Nelder and R. Mead. A simplex method for function minimization. *The Computer Journal*, 7:308–313, 1965. doi:10.1093/comjnl/7.4.308.